A Galaxy Cluster Survey Using the Sunyaev Zel'dovich Effect

Thesis by

Samantha F. Edgington

In Partial Fulfillment of the Requirements

for the Degree of

Doctor of Philosophy

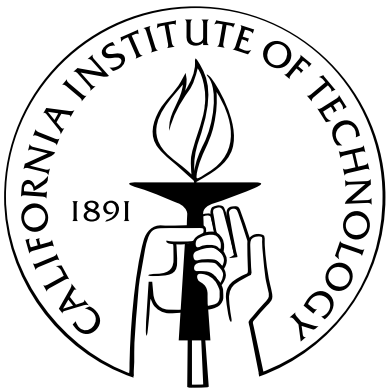

California Institute of Technology

Pasadena, California

2003

(Submitted September 27, 2003)

Abstract

This thesis describes the design and observations with the Bolocam instrument. Bolocam is a 144-element bolometer array designed to detect the Sunyaev Zel'dovich effect, used at the Caltech Submillimeter Observatory. Bolocam can be configured to observe at 1.1, 1.4, and 2.1 mm. We conducted a galaxy cluster survey at 2.1 mm, where clusters are detected as decrements against the Cosmic Microwave Background. The survey consisted of two blank fields, for a total of one square degree of coverage. We took advantage of the array configuration of the Bolocam focal plane to remove the atmospheric noise from the time stream before mapping the data. The sky noise removal left residual 1/f noise from the atmosphere in the data, and the resulting map sensitivity is limited by this noise. After filtering the maps to detect clusters with a FWHM of 2 arcminutes the RMS of the first map is 148.5 μK_{CMB} and the second is 77.8 μK_{CMB}. The difference is due to a difference in integration time on the two maps. Bolocam detected 2 4σ decrements in the two filtered $1/2 \times 1$ degree maps. Bolocam also places an upper limit on the CMB angular power spectrum at $\ell_{eff} \approx 6000$ of $\Delta T \leq 49$ μK_{CMB}.

Acknowledgements

Many people have helped to make this thesis possible. At Caltech, I would like to thank my advisor Andrew Lange for accepting me into the Bolocam program and allowing me the opportunity to work on this project. Byron Philhour and Marcus Runyan introduced me to instrumentation through the SuZIE project. Cindy Hunt was always ready and willing to explain how bolometers are made, and gave me a place to live when I needed one. Jason Glenn taught me much about the art of lab work. Phil Mauskopf showed me how to still enjoy physics after four years of graduate school. Douglas Haig kept me sane after 45 days at the summit of Mauna Kea. Sunil Golwala kept the Bolocam project on track, and helped to get the team to the telescope on time for the 2001 observing run. Several people must be thanked for actually reading the whole thesis. Luke Sollitt, who was there every Thursday for the past year asking for more plots and chapters, and Byron Philhour again came through with many useful suggestions. Outside of Caltech, many others helped me through graduate school and everything that came before. Thanks go to Sarah Grabill for being my best friend for 18 years even when I disappeared out to California and didn't call. Thanks must go to the late Professor David Wilkinson who was my mentor and taught me much more than just physics at Princeton. Also, thank you to Professor Steven Thorsett for guiding me through my first thesis, and Katie Berry, who suffered through all those late night study sessions with me, which helped to get us both into graduate school. I also want to thank my sister Lisa for her wonderful support and for helping to remind me that there is life outside of physics, and my parents, Margaret and Robert, because without their help and encouragement, and their complete faith in me, I would not have made it this far. Most of all I have to

thank Brian for everything he does everyday.

Contents

List of Figures

List of Tables

Chapter 1

Introduction

Cosmology is the attempt to answer the most basic of questions: What is the Universe made of? How has the Universe evolved from its first moments? How will the Universe evolve in the future? For the past 40 years we have had a basic framework of the answers to these questions based on the Cosmic Microwave Background (CMB) discovered by Penzias and Wilson in 1965 (Penzias and Wilson 1965), and the expanding Universe discovered by Edwin Hubble in 1929 (Hubble 1929). The background of microwave photons, and the fact that the Universe is expanding imply a hotter denser Universe in the past, leading to the Big Bang theory of the origin of the Universe. Until recently cosmology was primarily a theoretical science, with very little observational data. Any theory that could accommodate the Cosmic Microwave Background, the expanding Universe, and the development of structure was considered. Cosmology is now making the leap to an observational science with precise measurements of cosmological parameters (Peebles 2002).

Many different observations are contributing to our expanded data set on the nature of the Universe. The recent microwave measurements of the CMB by Boomerang (de Bernardis et al. 2000) and WMAP (Bennett et al. 2003) among many others have measured the cosmological parameters to higher precision than ever before, and have shown the Universe is flat. Measurements of high redshift supernovae have shown that the Universe is not only expanding, but accelerating (Perlmutter et al. 1999). The acceleration is explained by the much maligned, but now back in favor cosmological constant. The origin and nature of this constant is still a mystery. Two of the

most important cosmological parameters are Ω_M and Ω_Λ. Ω_M is the mass density of the Universe as a fraction of the critical mass and energy density required to produce a flat Universe. Ω_Λ is the energy density from the cosmological constant as a fraction of the critical density. Optical and X-ray observations of nearby galaxy clusters have measured $\Omega_M = 0.3$. Given that CMB observations require $\Omega_M + \Omega_\Lambda = 1$, this gives further evidence that $\Omega_\Lambda = 0.7$ and the cosmological constant is driving the acceleration of the expansion of the Universe.

This work will focus on a blind survey for clusters of galaxies at all redshifts. The rest of this chapter will describe how cluster surveys can help our understanding of cosmology, and how we are using the Bolocam instrument to perform such a survey. For a comprehensive introduction to the concepts of cosmology presented in the rest of this chapter see for example Peebles (1993). Chapter 2 will introduce bolometers, the detectors used by Bolocam. Chapter 3 describes the Bolocam instrument, Chapter 4 describes the Bolocam observations. In Chapter 5 we discuss the removal of atmospheric noise from the Bolocam data, and Chapter 6 discusses results from the current Bolocam data set. Finally Chapter 7 presents future prospects for Bolocam and cluster surveys.

1.1 Cosmic Microwave Background and Cluster Formation

Current cosmological theory holds that shortly after the Universe was created elementary particles were formed in a hot ionized plasma. Photons and electrons in this plasma were tightly bound. The density of this plasma was not uniform, but included primordial quantum fluctuations. During inflation, a short period of rapid expansion of the Universe early in its history, these quantum fluctuations grew into significant density variations. Weakly interacting dark matter particles collapsed into the over dense regions. The baryons are prevented from collapsing into the growing gravity wells formed by the dark matter by photon pressure. Eventually the Universe

expands, and cools enough for the electrons to bind to the baryons, in the epoch of recombination. After recombination the photons are decoupled from the now neutral atoms, and free-stream from the so called surface of last scattering. As the Universe further expands the wavelengths of the photons stretch to form the CMB we observe today at millimeter wavelengths. The spectrum of the CMB was found by the COBE satellite to be exceedingly well fit by a black body at 2.73 K (Bennett et al. 1994). The density fluctuations present in the Universe at the epoch of recombination were imprinted on the CMB background as tiny temperature variations. If we take the temperature of the sky in the direction $\hat{\theta}$ to be $T(\theta, \phi)$ we can write the temperature on the sky in terms of the spherical harmonic expansion:

$$T(\theta, \phi) = \sum_{\ell m} a_{\ell m} B_\ell Y_{\ell m}(\theta, \phi), \tag{1.1}$$

where B_ℓ is the window function of the instrument measuring the temperature, and $Y_{\ell m}$ are the spherical harmonics. The angular power spectrum gives the power of the temperature fluctuations at a given angular scale. The angular scale is defined by ℓ, the order of the Legendre polynomials that are part of the spherical harmonics. The angular power spectrum is defined as

$$C_\ell =< a_{\ell m} a^*_{\ell m} >= \frac{1}{2\ell + 1} \sum_{m=-\ell}^{\ell} |a_{\ell m}|^2. \tag{1.2}$$

The monopole term is given by C_0 and is the average temperature of the CMB. The dipole term, C_1, is dominated by the motion of the Earth with respect to the CMB, caused by our orbit around the Sun, the Sun's motion around the galaxy, and the peculiar velocity of our galaxy. The shape of the power spectrum starting with $\ell = 2$ encodes the information about the temperature fluctuations frozen in at the epoch of recombination. The shape of the CMB angular power spectrum has given us precise measurements of cosmological parameters in recent years (de Bernardis et al. 2000; Bennett et al. 2003). In this thesis, however, we will focus on the contribution of galaxy cluster surveys to our understanding of cosmology.

Once decoupled from the photons, the baryons fall into the dark matter gravity wells to form bound structures. The largest of these structures are clusters of galaxies. Clusters form from the rarest peaks in the density fluctuations. Because they are at the tail end of the Gaussian distribution of density fluctuations they are very sensitive to cosmological parameters.

1.2 Using Cluster Surveys in Cosmology

Many have suggested that galaxy clusters would provide a useful probe of cosmological parameters (Evrard et al. 2002). The number of clusters formed is dominated by the dark matter dynamics, and therefore dependent only on gravitational physics, not the more complex gas dynamics. The abundance of clusters should be determined only by the geometry of the Universe and the initial density fluctuations present in the Universe. A rough idea of the number of clusters we expect can be estimated from the values of Ω_M and Ω_Λ. A high Ω_M Universe, given that the other cosmological parameters are kept constant, will be quite young, and not have had time to form clusters. Lowering Ω_M and increasing Ω_Λ will increase the age of the Universe, and produce more clusters at the present time.

More quantitatively the number density of clusters as a function of redshift ($n(z)$) is determined by two effects; the changing co-moving volume element ($dV/d\Omega dz$), and the growth of structure given by the cluster mass function (dn/dM),

$$\frac{dn(z)}{d\Omega dz} = \int \frac{dn(M,z)}{dM}\frac{dV}{d\Omega dz}dM \tag{1.3}$$

where Ω is the solid angle on the sky, z is redshift, M is cluster mass. The co-moving volume element can be calculated from the Friedmann equation,

$$\left(\frac{\dot{a}}{a}\right)^2 = H^2(z) = H_0^2 E^2(z) = \frac{8\pi G\rho(z)}{3} + \frac{\Lambda}{3} - K(1+z)^2 \tag{1.4}$$

where $H(z)$ is the Hubble constant as a function of redshift, $\rho(z)$ is the mass density of the Universe as a function of redshift, G is the gravitational constant, Λ is the

cosmological constant, and K is the curvature of the Universe. We can rewrite $E(z)$ as a function of the critical density parameters

$$E^2(z) = \Omega_M(1+z)^3 + \Omega_\Lambda + \Omega_K(1+z)^2 \tag{1.5}$$

In currently accepted models Ω_K, the curvature of the Universe, is generally assumed to be zero, in line with the recent CMB results. All the density parameters are evaluated at the current epoch and the redshift dependence is included explicitly (Peebles 1993). The co-moving volume element is given by

$$\frac{dV}{d\Omega dz} = \frac{c(1+z)^2 d_A^2(z)}{H_0 E(z)} \tag{1.6}$$

where c is the speed of light, and $d_A(z)$ is the angular diameter distance which is given by

$$d_A(z) = \frac{1}{1+z}\int_0^z \frac{d\prime z}{E(\prime z)} \tag{1.7}$$

for the case of a flat Universe ($\Omega_K = 0$) (Holder et al. 2000).

The cluster mass function is described by the Press-Schechter function (Press and Schechter 1974). The co-moving number density of virialized objects between masses M and $M + dM$, and at redshift z is given by

$$\frac{dn(M,z)}{dM} = -\sqrt{\frac{2}{\pi}}\frac{\rho}{M}\frac{d\sigma(M,z)}{dM}\frac{\delta_c}{\sigma^2(M,z)}\exp\left(\frac{-\delta_c^2}{2\sigma^2(M,z)}\right) \tag{1.8}$$

where ρ is the background co-moving density, $\sigma(M,z)$ is the variance of the spectrum of density fluctuations on mass scale M, and δ_c is the linear over density of a density fluctuation that has collapsed. Applying this to Equation 1.3, we can calculate the number density of clusters we expect.

1.3 The Sunyaev Zel'dovich Effect and Clusters

The Sunyaev Zel'dovich Effect (SZE) is the Thompson scattering of CMB photons by the hot gas contained within galaxy clusters (Zel'dovich and Sunyaev 1980), for a comprehensive overview see Birkinshaw (1999). The probability of a photon scattering depends on the density of electrons in the hot gas, for most clusters it is estimated to be 1%. The CMB photons travel through the cluster gas and are boosted in energy due to the scattering, which is called the thermal SZE. This leads to a unique distortion of the CMB spectrum which consists of a deficit of photons below ≈ 218 GHz and a excess of photons above. The cluster therefore looks like a cold spot on the CMB at frequencies below 218 GHz and a hot spot above this frequency.

The spectrum of the SZE is given by

$$\frac{\Delta T_{SZ}}{T_{CMB}} = y\left(x\frac{e^x+1}{e^x-1} - 4\right) \tag{1.9}$$

where y is the Compton y parameter, proportional to the integrated electron pressure along the line of sight, and $x = h\nu/kT_{CMB}$. The Compton y parameter is given by

$$y = \int \frac{kT_e}{m_e c^2} n_e(l)\sigma_T dl \tag{1.10}$$

where the integral is along the line of sight through the cluster, k is the Boltzmann constant, T_e is the temperature of the electrons, m_e is the mass of an electron, $n_e(l)$ is the number density of electrons, c is the speed of light, and σ_T is the Thompson scattering cross section. We can rewrite the spectrum in terms of specific intensity

$$\Delta I_{SZ} = \frac{dB(T_{CMB},\nu)}{dT}\Delta T_{SZ} = I_0 g(x) y \tag{1.11}$$

where $B(T_{CMB},\nu)$ is the Planck black body spectrum, $I_0 = 2(kT_{CMB})^3/(hc)^2$, and

$$g(x) = \frac{x^4 e^x}{(e^x-1)^2}\left(x\frac{e^x+1}{e^x-1} - 4\right). \tag{1.12}$$

We can see from Equations 1.9 through 1.11 that the SZ surface brightness of a

cluster depends only on the properties of the cluster, and not on the redshift of cluster. The total flux of a cluster will depend slightly on redshift due to the angular diameter distance. The angular size of a cluster will fall off initially, but will eventually flatten to an almost constant level above a redshift of approximately 0.5. The total flux from a cluster is given by

$$S_{SZ} = I_0 g(x) \frac{\sigma_T k T_{CMB}}{m_e c^2} \frac{< T_e >_n N_e}{d_A^2(z)} \tag{1.13}$$

where $< T_e >_n$ is the mean density weighted electron temperature of the cluster, N_e is the total number of free electrons in the cluster plasma, and d_A^2 is the angular diameter distance.

The redshift independence of the SZE makes it an ideal tool for conducting a galaxy cluster survey. All clusters of a minimum Compton y parameter can be detected out to the redshift of formation, giving a sample of clusters that is limited by flux and not by redshift.

1.4 Sunyaev Zel'dovich Effect and the Angular Power Spectrum

The distortions of the CMB temperature map on the sky caused by the SZE are called secondary anisotropies, as opposed to the primary anisotropies caused by density fluctuations at recombination. The extra temperature fluctuations contribute to the CMB angular power spectrum and high values of ℓ at the angular scale of clusters which are the dominant source of the SZE. The data from a blind survey of blank sky can be used not only to detect individual clusters, but also to detect the high ℓ CMB angular power spectrum contribution from the SZE. Figure 1.1 shows the CMB power spectrum in red, the contribution from SZE predicted by Springel et al. (2001) using hydrodynamic simulations, and the predicted data points from a Bolocam survey in green.

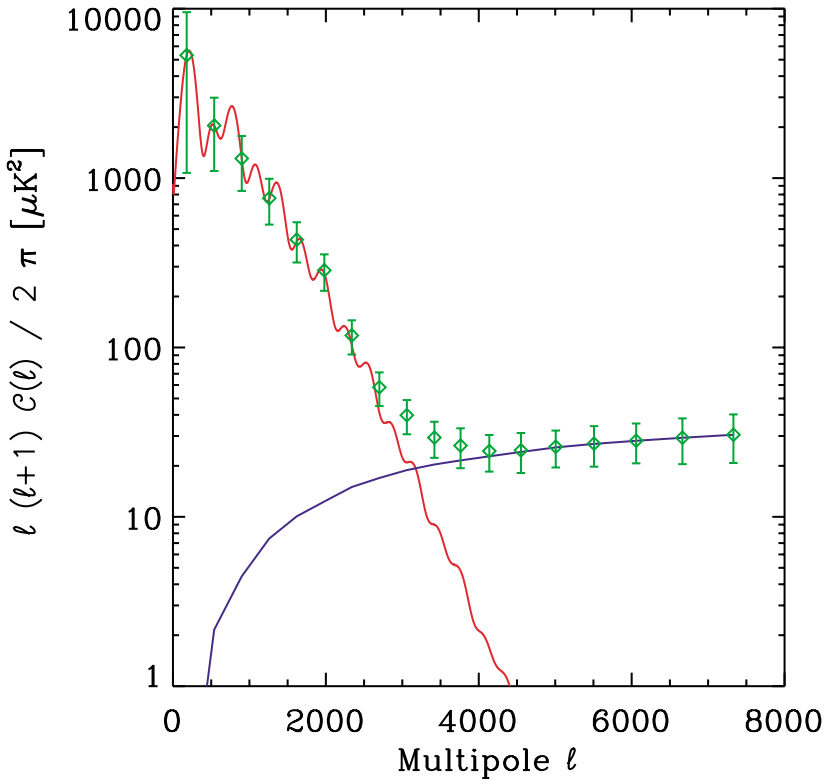

Figure 1.1: The CMB power spectrum in red, the SZE contribution at high ℓ in blue, and the predicted Bolocam data points in green. Figure courtesy of Eric Hivon.

1.5 Previous Work

Galaxy cluster surveys have been conducted for some time in optical and X-Ray wavelengths, but only recently have instruments been developed that can conduct a survey using the SZ effect. The most relevant prior surveys are those conducted by the Berkeley Illinois Maryland Association (BIMA) array (Dawson et al. 2002; Lin and Mohr 2003), the Cosmic Background Imager (CBI) (Mason et al. 2003), and the Arcminute Cosmology Bolometer Array Receiver (ACBAR) (Kuo et al. 2002).

The BIMA survey used receivers operating at 28.5 GHz to detect CMB power of $\Delta T = 14.2^{+4.8}_{-6.0} \mu K_{CMB}$ at $\ell \approx 7000$. The survey consisted of ten 6.6' circular fields, with a total area of 1/8 deg^2. Point sources were removed using a VLA survey. The power detected was attributed to unresolved SZ sources.

The CBI survey measured the CMB power spectrum out to $\ell \approx 3500$. The instrument operates at 30 GHz in the Atacama desert in Chile. The survey results report a $\Delta T = 23.9 \pm 17.5$ at $\ell \approx 2000 - 3000$, which is attributed to power from unresolved SZ sources. Point sources were removed with a survey using the 40 m telescope at the Owens Valley Radio Observatory.

The ACBAR project is a bolometric instrument operating at millimeter wavelengths on the VIPER telescope at the South Pole. Although the cluster survey did not yield any confirmed cluster candidates, a measurement of the high ℓ CMB power spectrum was made, $\Delta T = 17.5 \pm 16.6\ \mu K_{CMB}$.

Chapter 2

Millimeter-Wave Bolometers

2.1 Background

Bolometers are used by many instruments to study the CMB and the SZ effect. They are the most sensitive detectors available at the millimeter-wave bands, where the CMB signal flux is highest.

Bolometers are composed of two main parts, the thermistor and the absorber to which it is mounted. The absorber converts incident radiation to heat. This increase in temperature reduces the resistance of the thermistor. Because bolometers are sensitive to all radiation wavelengths, the frequency band is defined by optical filters placed in front of the absorber. Radiation is usually concentrated on the absorber using a feedhorn, leading to a cavity designed to allow optimal absorption of the radiation by the mounted bolometer. The temperature changes in the absorber are measured with a thermistor, a sensitive thermometer whose resistance varies with temperature. The Bolocam instrument uses a monolithic array of bolometers. 144 bolometers are fabricated on a single three inch silicon wafer to form the focal plane of the instrument. This chapter discusses a mathematical model for bolometers, and the noise properties. A detailed discussion of what follows can be found in Richards (1994).

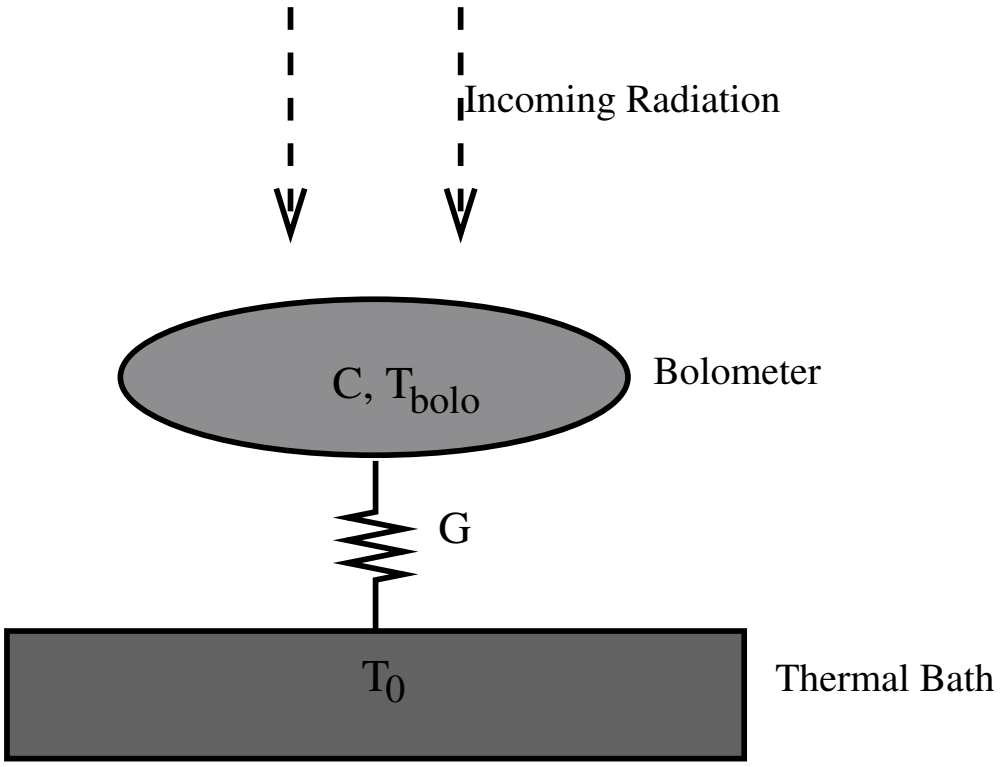

Figure 2.1: Bolometer thermodynamic model.

2.2 Bolometer Model

Bolometers can be described by a simple thermodynamic model diagrammed in Figure 2.1. The absorber, with heat capacity C, is connected to a thermal bath at temperature T_0 via a weak thermal link described by a thermal conductance G. The incoming radiation heats the absorber which then dissipates the energy to the thermal bath. Typically the thermal bath is cooled to approximately 300 mK with a ^{3}He sorption fridge, described in section 3.2. The change in resistance of the thermistor is converted to a voltage signal through a current biased circuit shown in Figure 2.2. Large load resistors in the circuit ensure that the current is constant despite resistance changes of the thermistor.

The main sources of power input into the bolometer are optical and electrical. The power output from the bolometer is through the thermal link to the bath temperature. The power balance equation that describes the temperature of the bolometer is as

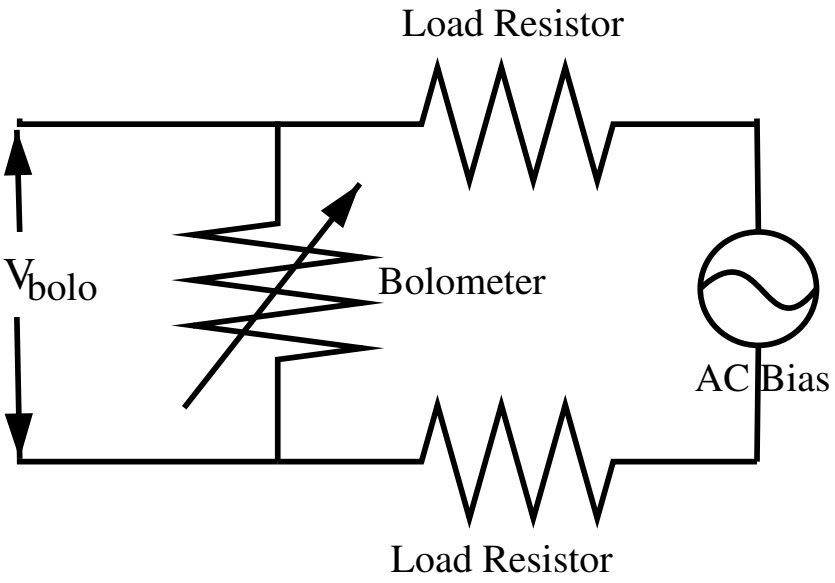

Figure 2.2: Bolometer readout circuit.

follows

$$C\frac{dT_{bolo}}{dt} = Q + P_{elec} - G(T_{bolo} - T_0) \tag{2.1}$$

where T_{bolo} is the temperature of the bolometer, Q is the incident optical power, $P_{elec} = I_{bias}^2 R_{bolo}$ is the electrical power, T_0 is the temperature of the thermal bath, usually the base plate upon which the bolometers are mounted. In many cases we are interested in a varying optical signal:

$$Q(t) = Q_{avg} + \Delta Q e^{i\omega t} \tag{2.2}$$

where Q_{avg} is the average optical power and ΔQ is the amplitude of the varing power, then the bolometer's temperature is given by

$$T_{bolo}(t) = T_{avg} + \Delta T e^{i\omega t} \tag{2.3}$$

where T_{avg} is the average temperature, and ΔT is the amplitude of the variations. Using equation 2.1 and solving for the change in temperature due to the oscillating

optical signal we obtain

$$\Delta T = \frac{\Delta P}{G\sqrt{1+\omega^2(\frac{C}{G})^2}}. \tag{2.4}$$

We can see from this equation that the bolometer acts as a single pole low pass filter on power fluctuations with a time constant of $\tau = C/G$.

The bolometer circuit translates changes in temperature into changes in signal voltage via the resistance changes of the thermistor as follows:

$$\frac{dV}{dT} = I_{bolo}\frac{dR_{bolo}}{dT} \tag{2.5}$$

The thermistors used by Bolocam are neutron transmutation doped (NTD) germanium, and have a resistance vs. temperature relation

$$R(T) = R_0 e^{(\sqrt{\frac{\Delta}{T}})} \tag{2.6}$$

where R_0 and Δ are properties of the specific germanium thermistor which can be measured using load curves.

Bolocam's bolometers are current biased by placing them in series with two load resistors of an impedance much larger than the operating impedance of the bolometer. A bias voltage is applied across the stack, and the voltage across the bolometer is read out to measure the resistance. The current in the circuit is essentially constant with the small variations in the bolometer resistance. Bolometers heat up in response to increases in optical power, which lowers the resistance of the thermistor, and causes a drop in the output voltage. The drop in resistance of the thermistor causes a drop in the applied electrical power, which in turn causes a slight cooling. This negative feedback loop is called electro-thermal feedback, and results in a shorter detector response time. The effect of electro-thermal feedback can be represented in the bolometer equations as an increase in the effective thermal conductivity, G_e, which means a shorter effective time constant, $\tau_e = C/G_e$. The effective thermal conductivity, G_e, is given by $G_e = G - I^2(dR/dT)$, which is usually rewritten as $G_e = G - \alpha I^2 R$, where $\alpha = R^{-1}(dR/dT)$. For Bolocam's NTD thermistors $\alpha \approx -16K^{-1}$.

A bolometer's responsivity is Volts read out with the bolometer circuit per Watt of incoming optical power. The bolometer's time constant imposes a single pole filter on the detector responsivity to optical power at frequency ω.

$$S(\omega) = \frac{S_0}{1 + i\omega\tau_e} \tag{2.7}$$

where S_0 is the DC responsivity that can be calculated either from the bolometer parameters or via the calibration of the instrument.

2.3 Load Curves

When using a bolometer it is necessary to determine the various parameters of the bolometer model. To do this we analyze bolometer load curves. A load curve consists of a measurement of V_{bolo} for many values of V_{bias} across the whole range of bias values. V_{bias} is easily converted to the current in the bolometer circuit, I_{bias}. A sample load curve from Bolocam can be seen in Figure 2.3. The non-ohmic shape at large bias voltages is due to the electro-thermal feedback. By analyzing the bolometer circuit we can solve for the resistance of the bolometer at any bias voltage.

$$R_{bolo} = \frac{V_{bolo}}{I_{bias}} = 2R_L \frac{V_{bolo}}{V_{bias} - V_{bolo}} \tag{2.8}$$

where R_L is the value of one of the load resistors (10 MΩ for Bolocam). In order to determine R_0 and Δ, we must measure the resistance of the bolometers at various temperatures and fit to equation 2.6. We blank off the bolometers to prevent heating by incident optical power, and measure the bolometer temperature by placing a thermometer on the base plate that provides the thermal bath. We determine the resistance of the bolometer by measuring the slope of the low current part of the load curve. We heat the base plate to determine R_{bolo} at various bath temperatures to determine R_0 and Δ.

The parameter Δ is an intrinsic property of the thermistor. We can use the value determined by the manufacturer of the thermistors in order to get a more accurate

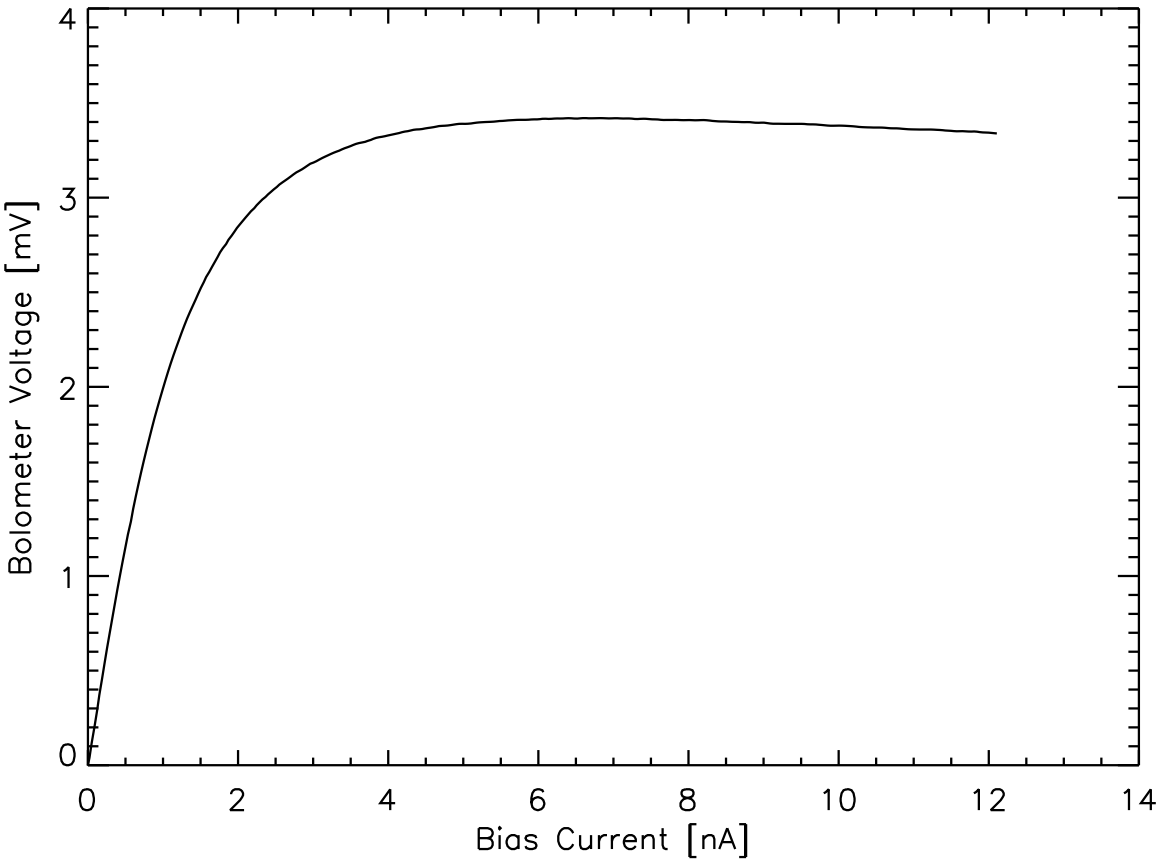

Figure 2.3: The voltage across the bolometer vs. bias current applied. The non-ohmic shape is due to electro-thermal feedback.

measure of R_0 by including a temperature offset δT in the fit. The temperature of the bolometers will not be exactly the same as the temperature of the base plate (T_0) due to factors such as errors in the thermometer calibration, and finite thermal conductance. By using $T_{bolo} = T_0 + \delta T$ in the fit and using the known value of Δ we can get an accurate measure of R_0 for all the bolometers. On average, Bolocam bolometers have an $R_0 = 180\Omega$, and $\Delta = 42K$.

Once R_0 and Δ are known, a load curve measurement can determine the value of G for the bolometers. The thermal conductivity is well described by at power law

$$\frac{dP}{dT_{bolo}} = G(T_{bolo}) = G_0 \left(\frac{T_{bolo}}{T_0}\right)^{\beta} \tag{2.9}$$

where T_0 is a reference temperature such that $G(T_0) = G_0$. G_0 is measured by taking a load curve of the bolometer with no incident optical power. The power on the bolometer is calculated from I_{bias} and R_{bolo}, and the temperture of the bolometer is calculated R_{bias}, Δ, and R_0. We fit equation 2.9 to the power vs. temperature after linearizing by taking the natural log. G_0 is usually referenced to $T_0 = 300$ mK as this is the base temperature most often used for semi-conductor thermistor bolometers.

2.4 Noise Sources

The main noise sources for a bolometer include phonon noise and Johnson noise, due to intrinsic detector parameters, and photon noise due to incident optical power. Amplifier voltage noise also contributes to the total noise of the system, and must be measured separately. Bolometer noise sources are generally measured as the amount of power required to generate a one sigma signal, or the noise equivalent power, NEP.

2.4.1 Detector Noise

The phonon noise is due to the quantization of the phonons that carry energy from the absorber to the thermal bath, via the thermal conductance G. The noise is proportional to the number of phonons times the energy per phonon. If we integrate

over the phonon distribution, we see that

$$NEP_{phonon} = \sqrt{4k_B T_{bolo}^2 G} \tag{2.10}$$

where T_{bolo} is the operating temperature of the bolometer, k_B is the Boltzmann constant, and G is the thermal conductivity of the bolometer.

Johnson noise is due to the random motion of electrons in the thermistor, and has the form

$$NEP_{Johnson} = \frac{\sqrt{4k_B T_{bolo} R_{bolo}}}{S(\omega)} \tag{2.11}$$

where R_{bolo} is the resistance of the bolometer, T_{bolo} is the temperature of the bolometer as before, and $S(\omega)$ is the responsivity of the bolometer.

2.4.2 Photon Noise

As we can see from equations 2.10 and 2.11 phonon and Johnson noise are due to intrinsic bolometer parameters. Photon noise is due, however, to the random arrival time of the incident photons. The Planck distribution gives the number of photons per second per Hz of bandwidth per spatial mode,

$$n = \frac{\epsilon\eta}{e^{h\nu/kT} - 1} \tag{2.12}$$

where ϵ is the source emissivity, η is the optical efficiency of the instrument, ν is the frequency of the radiation, and T is the temperature of the source. The variance in the number of photons absorbed by the detector is $< (\Delta n)^2 >= n + n^2$. The mean square fluctuation in power on the bolometer after one second of integration is $2Nh^2\nu^2 < (\Delta n)^2 >$, where $h\nu$ is the energy of one photon, N is the number of spatial modes (1, in the case of Bolocam), and the factor of 2 accounts for the two polarizations. Using this we can see that

$$NEP_{\gamma}^2 = 2\int P_\nu h\nu d\nu + \int P_\nu^2/N d\nu \tag{2.13}$$

where $P_\nu = 2Nnh\nu$ is the power spectral density, and the integral is over the spectral bandwidth. The first term is due to the random arrival times of the photons, and the second term accounts for the fact that photons bunch together because they are bosons. This second term, or Bose term, is the subject of some controversy. If an extra factor of $2Nt\Delta\nu$, where t is the integration time, and $\Delta\nu$ is the average bandpass width, should be in the denominator of the Bose term, then that term becomes negligible for Bolocam, significantly changing the expected photon noise. We will address this further in section 3.6 where Bolocam's noise measurements are presented. If we assume that P_ν is constant over the integral, then we can simplify equation 2.13

$$NEP_\gamma^2 \approx 2Qh\nu_0 + \frac{Q^2}{\Delta\nu} \tag{2.14}$$

where Q is the optical power as before, and ν_0 is the center band frequency.

Chapter 3

The Bolocam Instrument

The past decade has seen bolometer instruments at millimeter wavelengths move toward detector arrays with an increasing number of bolometers. This evolution toward true imaging cameras is similar to the evolution of infrared cameras in the past 20 years. Bolocam is the first instrument with a monolithic array of bolometers fabricated on the same silicon wafer instead of packing larger numbers of individual bolometers onto a focal plane. The monolithic array was developed at the Micro Devices Lab at JPL as a prototype for the SPIRE instrument to be flown on the Herschel satellite, and allows a larger number of detectors to be placed in a relatively small focal plane. Bolocam has 144 detectors on a wafer 3 inches in diameter.

In order to operate with low noise the Bolocam bolometer wafer must be brought to a temperature of 300 mK or below. For this reason the wafer is mounted inside a dewar that cools the detectors and contains the necessary read out electronics and optics. The entire dewar is mounted on the Caltech Submillimeter Observatory at Mauna Kea, Hawai'i. This chapter presents the design and in-lab characterization of the Bolocam instrument.

3.1 Caltech Submillimeter Observatory

Bolocam was designed to be mounted on the Caltech Submillimeter Observatory (CSO), a 10.4-meter telescope at the summit of Mauna Kea, which can be seen in Figure 3.1. Like most submillimeter telescopes the CSO has an alt-az mount which

Figure 3.1: The Caltech Submillimeter Observatory observing in the morning

means it moves in azimuth and elevation. The CSO has a telescope with a 10.4 m primary mirror made up of hexagonal segments designed based on the work of Robert Leighton (Leighton 1976). A 22-inch diameter secondary mirror is supported by three legs mounted on the primary. The entire telescope is protected by a compact dome that rotates with the dish. The control room and various labs are housed inside the dome. The telescope itself is on a separate foundation to the dome and the two are not connected at any point. This reduces vibrations on the telescope and instruments. The Bolocam dewar and associated optics are mounted behind the hole in the primary dish at the Cassegrain focus. A photo of the Bolocam dewar and optics mounted on the telescope is shown in Figure 3.2.

Bolocam observes approximately 20 hours every day, with great care being taken not to get any sun on the primary dish. Even at an oblique angle any rays from the sun can be focused by the telescope and cause damage to the instruments and mirror surfaces.

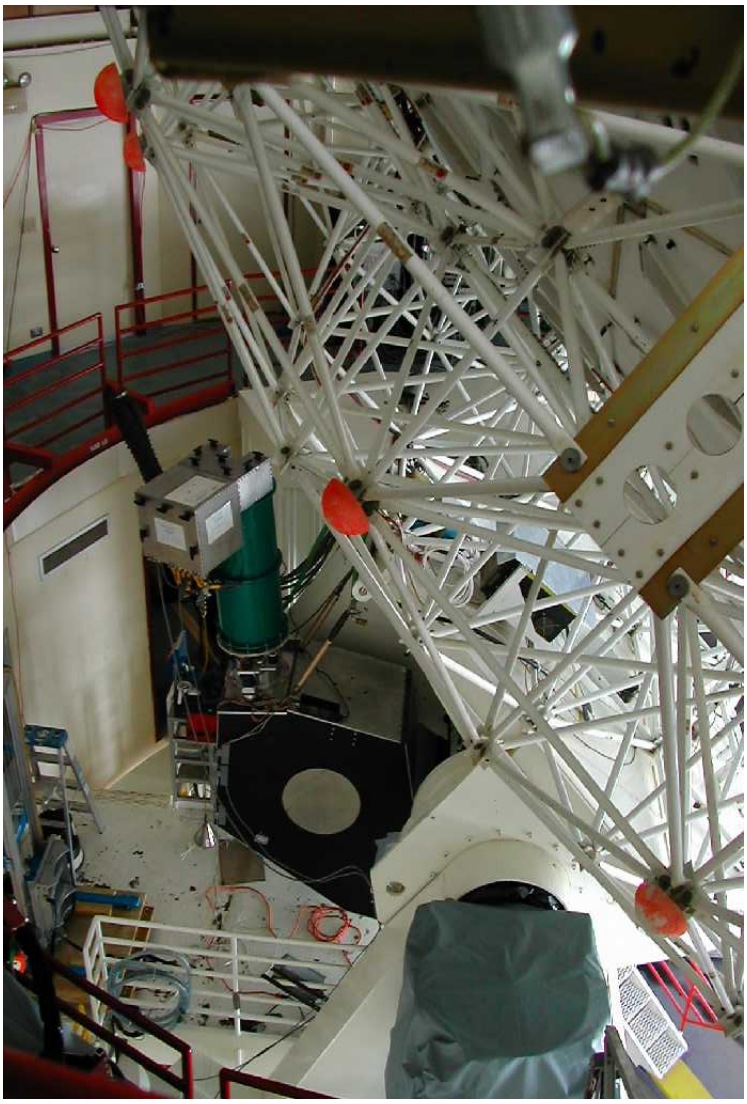

Figure 3.2: The Bolocam optics box mounted behind the CSO primary mirror at the Cassegrain focus.

3.1.1 Dewar Rotator

As the sky rotates overhead over the course of the night, the orientation of extended sources rotates also. The angle of the orientation is called the parallactic angle. The parallactic angle defines the rotation between right ascension (RA)/declination (dec) coordinate system and the local azimuth/elevation coordinate system. If we wish to scan in the RA direction with the same orientation of bolometers over the course of the night, the dewar must be rotated to compensate for the change in parallactic angle.

The dewar is mounted onto the optics box with a mount that rotates freely. A motor rotates the dewar using a gear attached to the motor and a rack that wraps around the dewar[1]. Bolocam used the SID 2.0 step motion system, which consists of a stepper motor, and the CY545 motor controller from Cybernetic Micro Systems[2]. The motor controller accepts formatted ASCII input from the serial port which selects one of several built in commands. The main commands used by Bolocam set the speed and acceleration of the motor, and the number of steps required in the motion. These commands are sent by a C program as formatted ASCII via the serial port on the instrument computer.

An absolute encoder records the dewar angle. The encoder must have a reproducible zero point to calibrate each night. The motor provides an infrared homing sensor. By running a specialized command the motor controller will rotate the motor in a clock wise direction until the homing sensor is blocked by the homing tab. This provides a reproducible position which can be used to calibrate the encoder. The homing command will rotate the dewar clockwise first, and since the dewar cannot rotate a full 360^o, the homing tab must always be to the right of the homing sensor before the homing command is run. The encoder is also controlled via the serial port on the instrument computer. A single C program controls the motor, reads the position of the encoder, and communicates with the telescope computer.

[1]The Motion Group P.O. Box 4585, Mountain View, CA 94040
[2]http://www.ControlChips.com, San Gregorio, CA 94074

3.1.2 Telescope Computer Interface

The data is collected at the telescope using three autonomous computers. The first is the Data Acquisition System, or DAS. The second computer is the antenna computer, which controls the telescope. The final computer is the instrument computer, running the Linux operating system, which controls the dewar rotator and any required communication between the instrument and the telescope.

The DAS consists of a multiplexer and an analog to digital converter board by National Instruments that samples the bolometer signals at 50Hz. The resulting signals are recorded into binary files consisting of one minute of data by a LabView program.

The telescope is controlled by the antenna computer, a Power-PC computer running the real time LynxOS operating system. In addition to controlling the motion of the telescope, the antenna computer records the pointing information of the telescope in a compact binary file written at 100Hz. The computer creates one file for every minute past midnight Universal Time. Bolocam observations are controlled via various macros that send commands to the antenna computer describing the telescope motion required to complete the observation.

The instrument computer controls the dewar rotator, and handles any required communication with the antenna computer. This computer also writes one file each minute containing auxiliary data that is not stored in the other two data files, such as the rotation angle of the dewar and the name and position of the source being observed. This auxiliary data is not rapidly changing, and is therefore recorded at a rate of one hertz. Information such as the source name is obtained from the antenna computer via a Remote Protocol Command over the summit network. The rotator angle is provided by an encoder that is accessed via the serial port.

The instrument communicates with the telescope in order to control the rotation of the dewar. The instrument must know when it is safe to rotate the dewar, and the telescope must know when the instrument has completed the rotation. This communication is achieved using Transistor-Transistor Logic (TTL) signals. The TTL

signals are simple low/high voltage levels carried by coaxial cables. The TTL signals are monitored by the instrument computer using a digital I/O board manufactured by SeaLevel Systems[3]. Two TTL signals, one controlled by the instrument computer and one controlled by the antenna computer, control the timing of the dewar rotation. The antenna computer also controls an observation TTL signal, which is set high for one second at the beginning of each new observation macro. The instrument computer monitors this TTL signal and increases the observation number being recorded by one each time it is set high. In this manner each Bolocam observation for a given night has a unique observation number which can be used for easy identification within the data analysis software.

3.2 Cryogenics

In order to reduce phonon noise in the detectors, the array must be cooled to below 300 mK. To accomplish this the array is placed in a dewar and cooled by a sub-kelvin sorption cooler.

3.2.1 The Dewar

The Bolocam dewar, shown in Figure 3.3, is a downward looking liquid helium/liquid nitrogen cryostat constructed by Precision Cryogenics[4]. The helium and nitrogen baths hold 16 liters each. The liquid helium lasts approximately 24 hours during normal operation, and the liquid nitrogen lasts approximately three days. The liquid helium cools, to 4.2 K, an aluminum plate called the cold plate. The cold plate is 16" in diameter and has a 77 K warm finger in the center. The warm finger is a 1/4" diameter copper rod that passes from the bottom of the liquid nitrogen bath through a hole in the helium bath through the center of the cold plate. The finger is used to heat-sink the cold amplifiers which operate best near 130 K. Such a mechanism allows us to conserve liquid helium and extend the lifetime of the sub-kelvin cooler.

[3]SeaLevel Systems, Liberty, SC 29657
[4]http://www.precisioncryo.com, Indianapolis, IN 46214

Figure 3.3: The Bolocam dewar in the lab during testing. The electronics box is open and we can see one of the preamp boards. The dewar is downward looking and the window is not visible.

The cold amplifiers are enclosed in a box made from a single block of aluminum. The box prevents radiation from the cold amplifiers from reaching the bolometers. A one foot long snout is attached to the bottom of the dewar to contain the optics that must be cooled to below room temperature. The detector array sits at the entrance to the snout. The detector array, which operates below 300 mK, must be thermally isolated from the 4.2 K cold plate. This is accomplished using hollow cylinders of vespel. Vespel is a plastic with a very low thermal conductivity. The vespel cylinders form the legs for a two tier support structure for the detector array referred to as the wedding cake assembly (Figure 3.4). Each tier of the wedding cake assembly is thermally connected to the sub-kelvin cooler which maintains the detector temperature, and the entire assembly is mounted on top of the cold amplifier box.

Bolocam uses two types of thermometers inside the dewar, silicon diode ther-

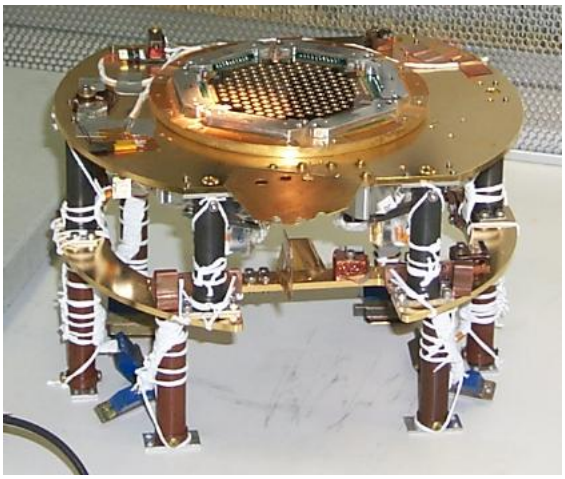

Figure 3.4: The wedding cake assembly with the detector array mounted at the top. When the dewar is observing the assembly is suspended from the JFET box, and the feedhorns are mounted above the detector array.

mometers, and germanium resistance thermometers (GRTs). Both are manufactured by Lake Shore Cryogenics Inc[5]. The silicon diode thermometers are useful between 4 K and 300 K, and are used to measure all temperatures during cool down from room temperature, the cryogenics baths, and various positions within the cold amplifier assembly. Four GRTs are used to measure the sub 4 K temperatures achieved by the sub-kelvin sorption cooler described below. The diodes present on the detector stage must be turned off when the cooler is cycled because the power dissipated increases the temperature of the detector stage, and reduces the hold time of the sub-kelvin cooler.

3.2.2 Bolocam Sub-Kelvin Cooler

In general we want the bolometers to be background limited, where detector noise is lower than the photon noise caused by the incident optical power. To accomplish this with the Bolocam detectors the base temperature must be below 300 mK. This temperature is easily achievable with a sub-kelvin cooler called a ^{3}He sorption fridge. A schematic of the Bolocam sorption fridge is shown in Figure 3.5. The Bolocam fridge was designed by Simon Chase of Chase Research in collaboration with both

[5]http://www.lakeshore.com, Westerville, OH 43082

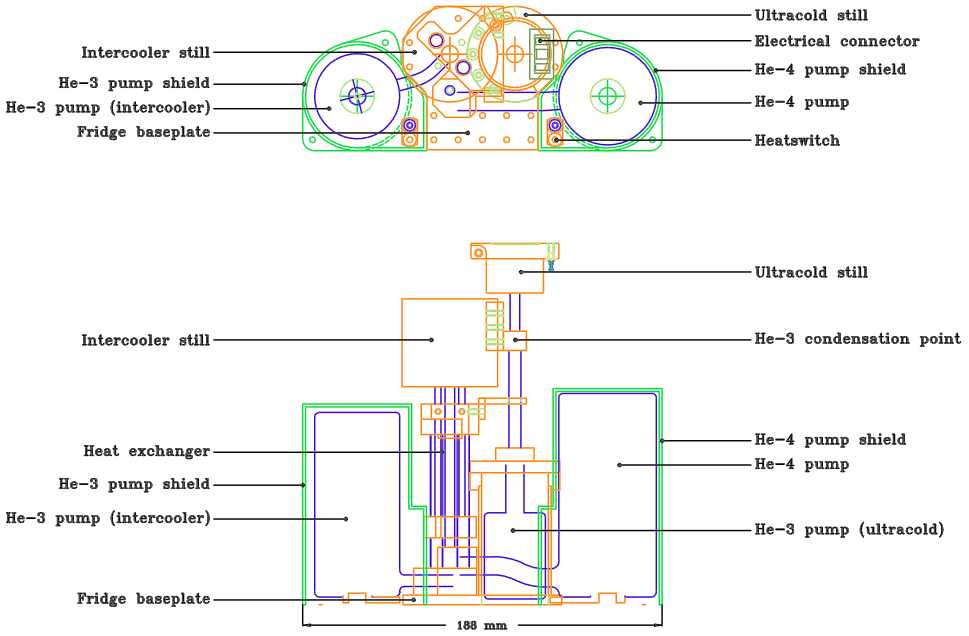

Figure 3.5: A diagram of the Bolocam fridge. Figure courtesy of S. Chase at Chase Research

the Bolocam and Polatron (Philhour 2001) projects. The Bolocam design is based on the standard ^{3}He sorption fridge. A fridge of this type employs the fact that liquid ^{3}He boils at a temperature below 300 mK in near vacuum. A standard ^{3}He sorption fridge has three main sections, the still, the pump tube, and the pump. The pump is composed of activated charcoal which absorbs the ^{3}He on its surfaces at temperatures below 20 K. When the pump is heated above 20 K the ^{3}He is released. If the still is at a temperature $\leq$ 1.2 K, the ^{3}He gas will condense to a liquid and drip into the still. As the ^{3}He boils off, the pump is allowed to cool and captures the gas, maintaining a near vacuum in which the ^{3}He boils below 300 mK. The pump tube diameter controls how fast the ^{3}He boils off, and therefore the final temperature of the still given a fixed heat load.

The standard ^{3}He sorption fridge requires the still be be brought to a temperature of 1.2 K in order to condense the ^{3}He. The standard way to achieve this is to pump on the liquid ^{4}He bath with a vacuum pump. This limits the hold time of the liquid helium bath as much of it is lost during the initial pump down to vacuum, and greatly

complicates the operation of the dewar. The Bolocam fridge is a three stage ^{3}He/^{4}He sorption fridge design that obviates the need to pump on the liquid helium bath. Bhatia et al. (2000) gives a detailed description of this new fridge design. Within the three-stage fridge each stage operates in the same manner as the standard ^{3}He sorption fridge described above. Two of the stages are ^{3}He. The first, called the ultracold stage, cools the detectors to approximately 250 mK. The other, called the intercooler, cools the middle stage of the wedding cake assembly to approximately 1 K. The third stage is ^{4}He, which operates exactly the same way, but only cools to 1.2 K. This stage is used only to condense ^{3}He for the ultracold and intercooler stages and is not active during normal operation.

A cycle of the fridge from 4 K to 250 mK takes approximately 4 hours. The pumps for all three stages are operated by applying a voltage to a resistor attached to the base of each of the pumps. The temperatures of each pump are monitored by diodes, and the temperatures of the ultracold and intercooler stages are monitored by GRTs embedded in the stills. There are also GRTs on the corresponding wedding cake assembly tiers which have been shown to have almost identical temperatures to the fridge stills. The fridge cycle is run and monitored by a custom designed LabView program. The program controls two programmable power supplies that provide voltage to the pump heaters, and monitors the diode and GRT temperature values via a custom made electronics board. The computer starts the fridge cycle at the appropriate time to ensure the instrument is ready for observations when needed. This significantly reduces the number of man hours spent preparing to take data each day.

Because the Bolocam fridge was a new design the cooling power of both the ultracold and intercooler stages were measured. The measurement took the form of load curves on each stage. Heaters were attached to both the ultracold and intercooler stills and the temperature of the still was recorded as known heat loads were applied. The fridge load curves allow us to predict the final detector temperature given the expected heat loads on the fridge. The results from both load curves are shown in Figure 3.6.

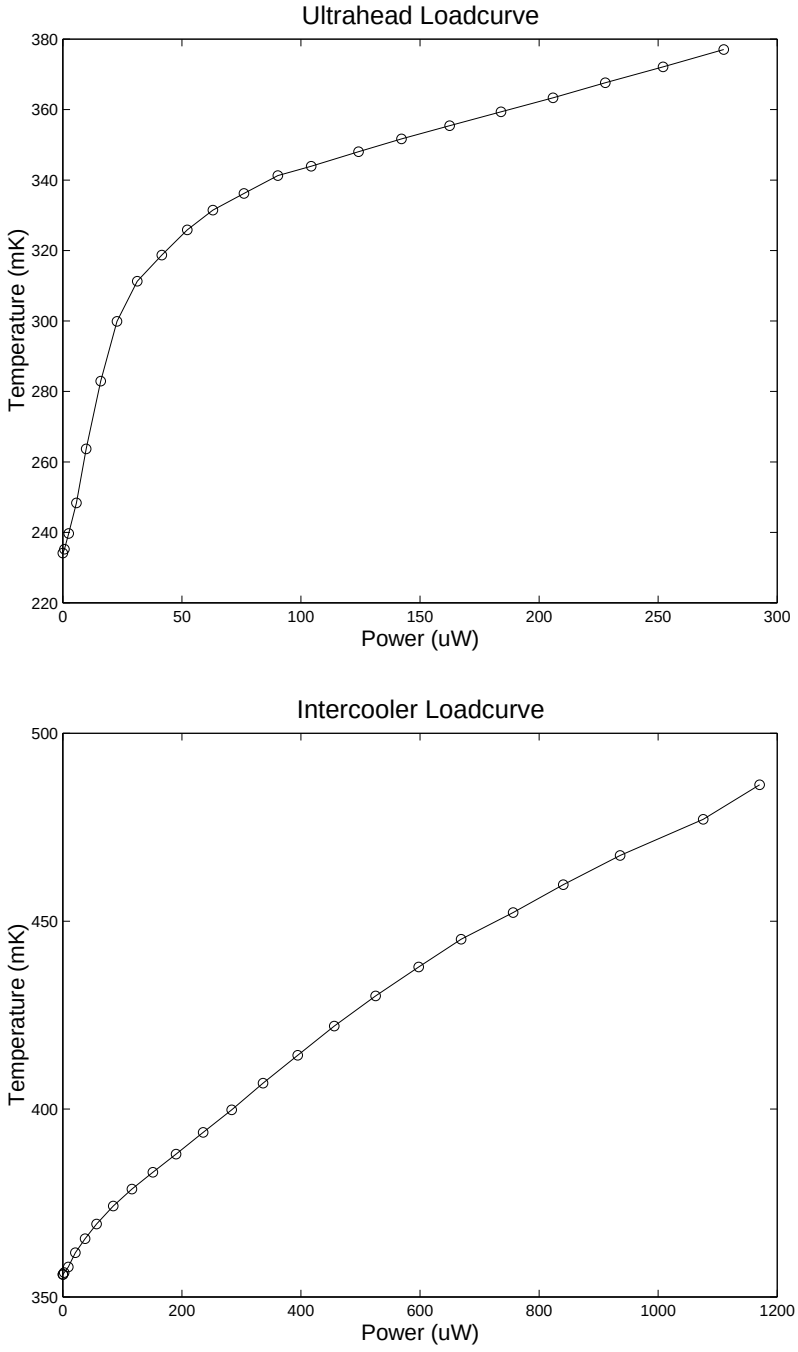

Figure 3.6: Load curves on the ultracold and intercooler stages of the fridge.

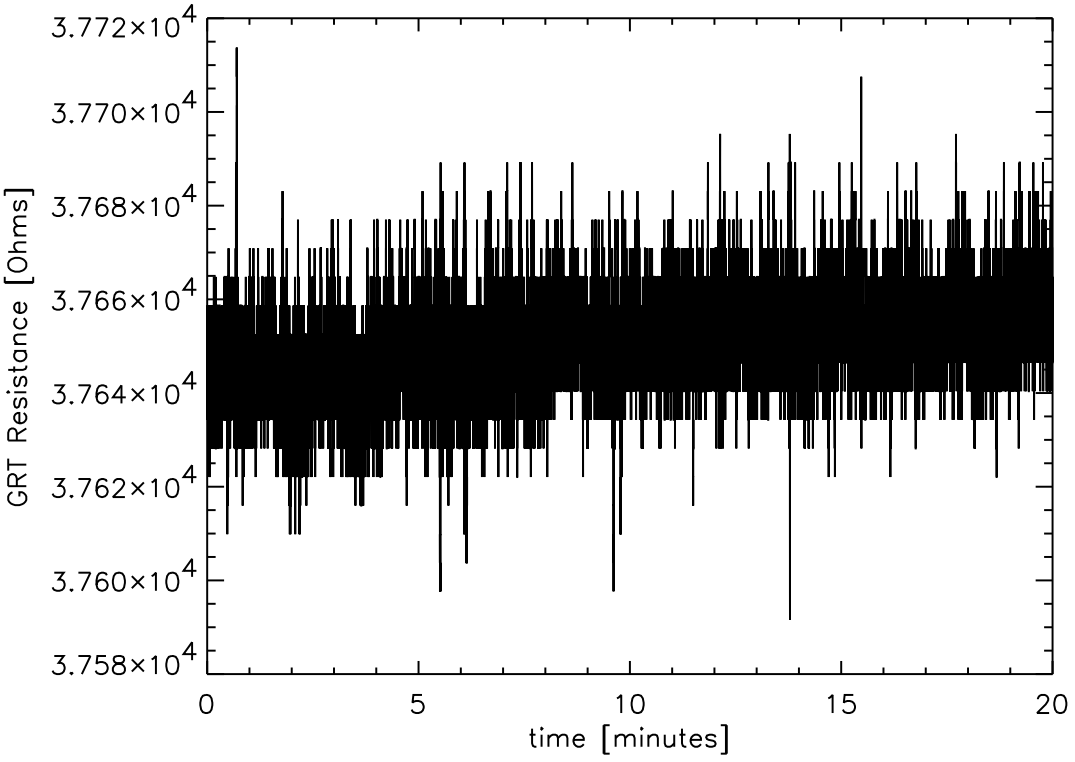

Figure 3.7: The resistance of the ultracold still GRT over the course of an observation. The noise is due to bit noise in the analog to digital converter. The temperature drift over the course of the observation is less than 0.02 mK.

The addition of an intercooler stage to buffer the ultracold still from the 4 K cold plate provides an exceptionally stable detector bath temperature without temperature control. Resistance of the ultracold still GRT over the course of an observation is shown in Figure 3.7. The noise is due to bit noise in the analog to digital converter. The resistance change of approximately 10 Ω over the course of the observation corresponds to a temperature difference of less than 0.02 mK, corresponding to a bolometer resistance change of less than 0.5%.

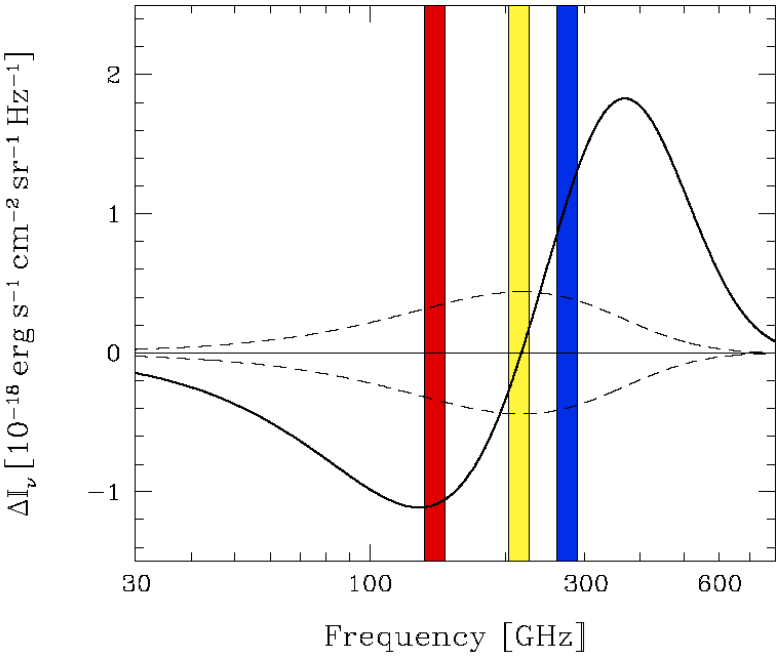

Figure 3.8: The Sunyaev-Zel'dovich Effect spectrum with the positions of the Bolocam band passes indicated. The red band pass is the 2.1 mm band pass focused on in this work.

3.3 Optics

Bolocam is designed to observe the Sunyaev-Zel'dovich effect at the decrement, null, and increment frequencies as shown in Figure 3.8. Separate optics where therefore designed for the three different wavelength bands. We observe at one wavelength band at a time. This work focuses on the 2.1 mm observations during the winter of 2001.

The Bolocam optics consist of two separate parts, the warm optics contained within the optics box that mounts behind the telescope's primary dish, and the cold optics contained within the snout at the bottom of the Bolocam dewar. The warm optics include two flat mirrors to fold the beam, and one ellipsoidal mirror that converts the f/12.36 beam provided by the telescope at the Cassegrain focus to an f/7.5 beam that enters the dewar. The optics are designed to give maximum overlap of the beams for each bolometer on the primary mirror. This optimizes the removal of atmospheric noise by averaging the bolometer signals as all the bolometers will look

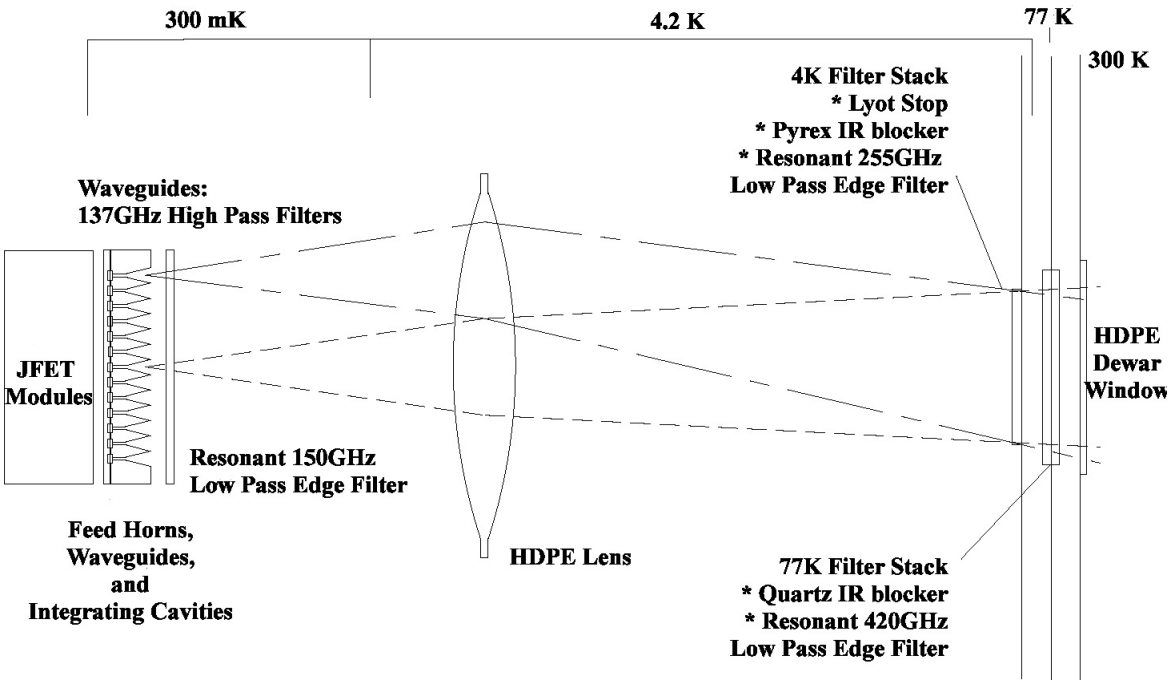

Figure 3.9: Simplified Bolocam cold optics schematic.

through almost identical columns of atmosphere. The calculated maximum deviation from the center of the primary mirror of the centroid of any beam is 0.5m. The CSO prohibits taking measurements of the beams on the primary mirror to prevent damage to the surface. The overlap of the beams on the primary must be inferred from other measurements such as the correlation of the sky signal in separate bolometers.

A simplified schematic of the cold optics is shown in Figure 3.9. A Lyot stop is a metal flange with a carefully controlled inner diameter that controls the origin of any light that reaches the detectors. Bolocam's Lyot stop is located at the 4 K shield just inside the dewar. The primary mirror is imaged at this point, and the Lyot stop allows only the rays from the center 8.15 m of the primary dish to propagate further into the dewar. The Lyot stop prevents about 50% of the light from passing beyond the 4 K shield; this reduces the overall efficiency but plays an important rold in reducing systematic offsets from light scattered off the ground and dome structure.

The lens refocuses the beams at the feedhorns, and creates a flat focal plane. The flat focal plane is necessary because the array is a single piece of silicon.

The feedhorns concentrate the incoming radiation onto the detectors. The most

important parameter for the Bolocam feedhorns is their spacing. The closer the horns are spaced the smaller the opening aperture, which reduces the efficiency with which they couple to the incoming radiation. The larger the spacing, and the fewer number of feedhorns that can be fit on the focal plane. Bolocam's feedhorns are machined into a single piece of aluminum and touch each other at the opening. Therefore the spacing between feedhorns is equal to their opening aperture. The feedhorn's opening aperture is often quoted in term of fλ, where f is the f number of the optics, and λ is the wavelength. A feedhorn with an opening aperture of 2 fλ will have maximum efficiency for point source detection, but will have different physical size depending on the optics and wavelength of detected radiation (Griffin et al. 2002). Because the spacing of detectors on the Bolocam array is fixed the opening aperture of the feedhorns is restricted so that the feed horns align with the detectors. For the 2.1 mm configuration there were two options, either using every bolometer and having 0.85 fλ horn spacing, or using every other bolometer and having 1.7 fλ horn spacing. While the 0.8 fλ horns do not couple as well to the incoming radiation, the factor of 4 increase in the number of detectors in this configuration leads to an approximately equal time to make a given map assuming 100% yield on the detectors (Griffin et al. 2002).

After being concentrated by the feedhorn, the radiation enters the waveguide which provides the low frequency cut off for the bandpass. The waveguide exits into an integrating cavity that optimizes the absorption of the bolometer. A standing wave is created inside the integrating cavity with a maximum at the bolometer. This allows the bolometer to absorb almost 100% of the incoming radiation (Glenn et al. 2002).

3.3.1 Filtering

The final part of the optical design is the set of optical filters that determine the frequency bandpass, referred to as the filter stack. Because bolometers absorb any incident light it is important to filter the incoming radiation so that only those fre-

quencies that are desired enter the feedhorns and are absorbed by the bolometers. Bolocam was optimized to observe the Sunyaev-Zel'dovich effect (SZE). Three bandpasses were designed, at the decrement, null, and increment of the thermal SZE, shown in Figure 3.8, though only one bandpass can be used per observing run. This work is concerned with the 2.1 mm bandpass which was designed to observe the decrement of the SZE, while avoiding absorption lines in the atmosphere. As mentioned above the waveguides after the feedhorns set the low frequency cut off for the bandpass at 137GHz. The high frequency cut off at 150GHz is defined by the low pass metal mesh resonant filter mounted above the feedhorns. Metal mesh resonant filters suffer from harmonic leaks at high frequencies which must be blocked with additional filters. The rest of the filter stack is designed to prevent high frequency leaks, and to reduce the loading on both the final filter and the fridge.

Referring to Figure 3.9, the filter stack starts at 300 K with the high-density polyethylene dewar window tuned in width to second order for maximum transmission within the bandpass. At the 77 K shield is a quartz dielectric filter, tuned to first order for maximum transmission at the center band frequency, and a metal mesh resonant filter with a 420GHz low pass cut off. At the 4 K shield is another metal mesh filter with a 255GHz low pass cut off, along with a Pyrex filter at the Lyot stop, also tuned to first order for maximum transmission in band. Mounted above the feedhorns at 300 mK is the band defining metal mesh filter with a 150 GHz low pass cut off. The metal mesh resonance filters were designed and manufactured by the Astronomy Instrumentation Group at the University of Wales at Cardiff (Lee et al. 1996).

The final bandpass of the instrument is measured using the Fourier Transform Spectrometer at Caltech. The resulting bandpass is shown in Figure 3.10 superimposed on the atmospheric transmission at Mauna Kea in normal observing conditions, with 1 mm of precipitable water vapor. The atmospheric transmission was calculated using the ATM software provided by the Caltech Submillimeter Observatory. In many applications it is not necessary to know the full shape of the bandpass, it is sufficient to know just the central frequency (ν_0) and the full width at half max

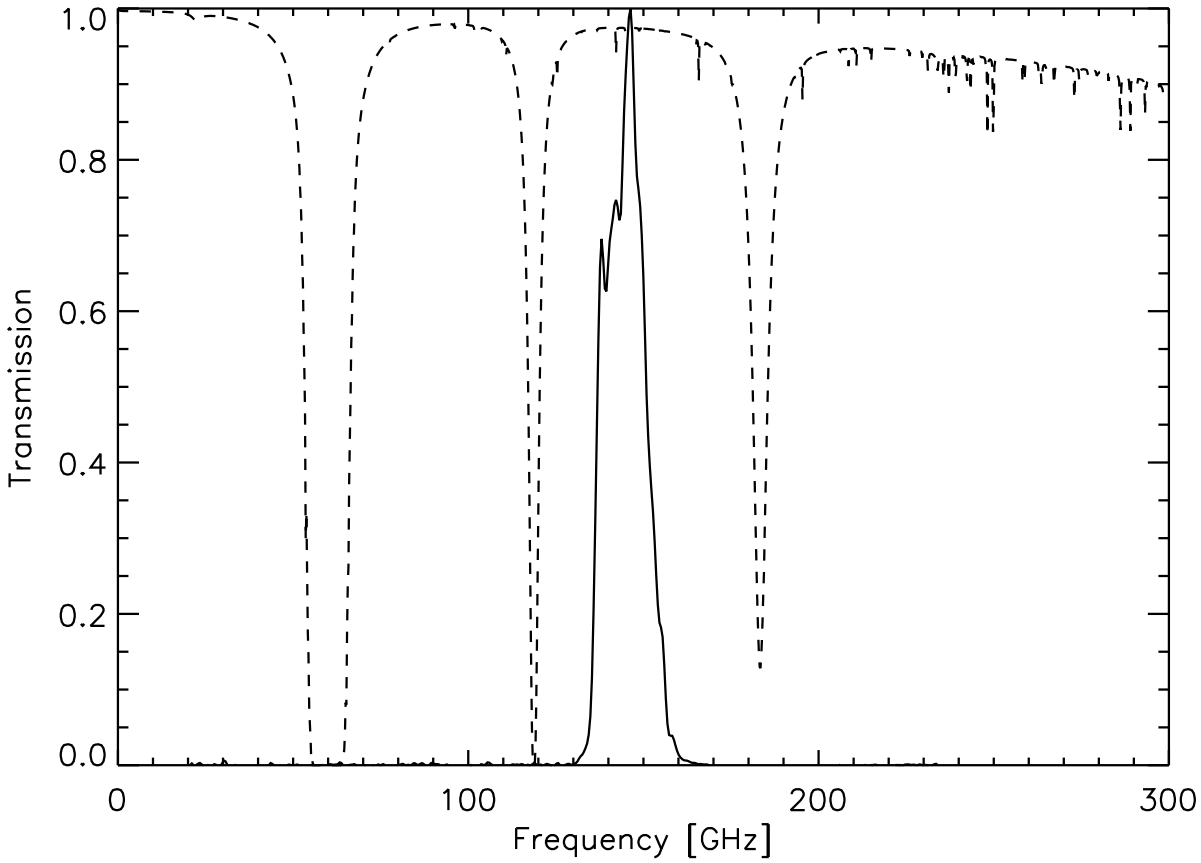

Figure 3.10: The Bolocam 2.1 mm bandpass is the solid line. The dashed line is the atmospheric transmission during average observing conditions at the CSO.

($\Delta\nu$). For the 2.1 mm bandpass, $\nu_0 = 146$ GHz and $\Delta\nu = 18.1$.

3.3.2 Beam Maps

If we think of the optics chain in a time-reversed sense, we can imagine that a beam of radiation, originating at a detector, propagates through the optics and eventually reaches the sky. To verify the new optical design for Bolocam we mapped the beams from various bolometers in the lab as they appeared at the relative position of the CSO secondary mirror. Testing shape of the beams on the sky must wait until the instrument is installed on the telescope. The position of the secondary mirror is the furthest down the optical chain that can be measured in the lab. The beams are measured using a black body source at 900^{o}C with a one inch aperture, and a chopper in front of the aperture. We move this chopped source in the beam of the instrument at a distance corresponding to the anticipated location of the secondary mirror. We demodulate the signal using a commercial lock-in amplifier.

The optical chain was originally designed at 1.4 mm using the prototype detector array. The results of the secondary beam map for the prototype system is shown in Figure 3.11. The measured beam is similar to the expected beam on the secondary, a top hat shape with a width of 18 inches. The full two-dimensional map is quite time consuming, the map shown took over 6 hours to make. For the 2.1 mm system we restricted our map to a one-dimensional slice through the center of the beam in both vertical and horizontal directions. With this time savings it was possible to map most of the 30 active bolometers in the 2.1 mm system. The predicted beam for the 2.1 mm system at the position of the secondary mirror is much the same as that for the 1.4 mm system, a top hat shape with a width of 18 inches. The results are shown in Figure 3.12.

3.4 Detectors

The Bolocam detectors consist of 151 silicon nitride mesh bolometers with NTD germanium thermistors, as described in Chapter 2, lithographed onto a single three

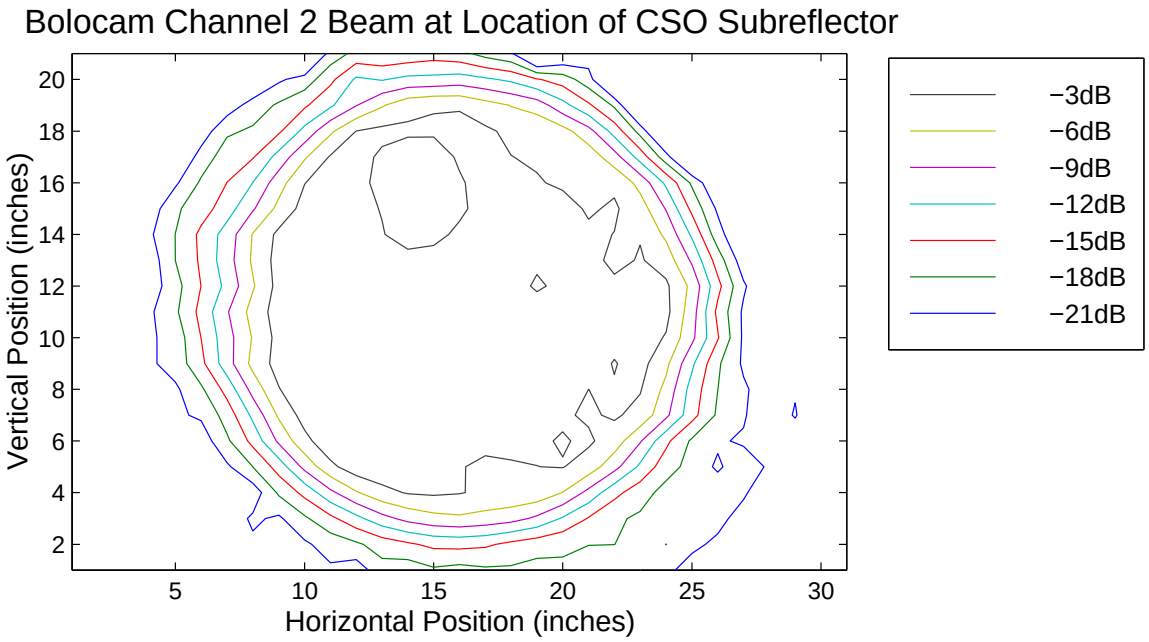

Figure 3.11: Beam map of one channel at the position of the CSO sub-reflector. The sub-reflector is 22 inches in diameter.

inch silicon wafer (Figure 3.13). The Bolocam array, called a monolithic detector array, is a prototype for the arrays developed by the Micro Devices Lab at the Jet Propulsion Lab for the SPIRE instrument on the Herschel (formally FIRST) satellite (Bock et al. 1998). Of the 151 detectors on the array, 144 of them are wired to six micro-D connectors that ring the array, conveniently splitting the array into six hextants of 24 bolometers each. The biggest challenge in making the bolometer arrays is detector yield. Traditional fabrication techniques did not aim to increase the yield of detectors fabricated on the same wafer because any functioning bolometers would be removed and operated separately. In the case of Bolocam's monolithic array all the bolometers on the array are to be used. We had two prototype arrays, as the techniques to increase yield were developed. The third array we call the 2001 science array as it was used for science observations instead of just engineering. The 2001 Science Array (2001-SA) has a yield of 53 bolometers out of 144. At 2.1 mm we had the option of either coupling every bolometer to a 0.85 fλ feedhorn, or using every other feedhorn for a total of 36 1.7 fλ feedhorns. The resulting mapping speed was

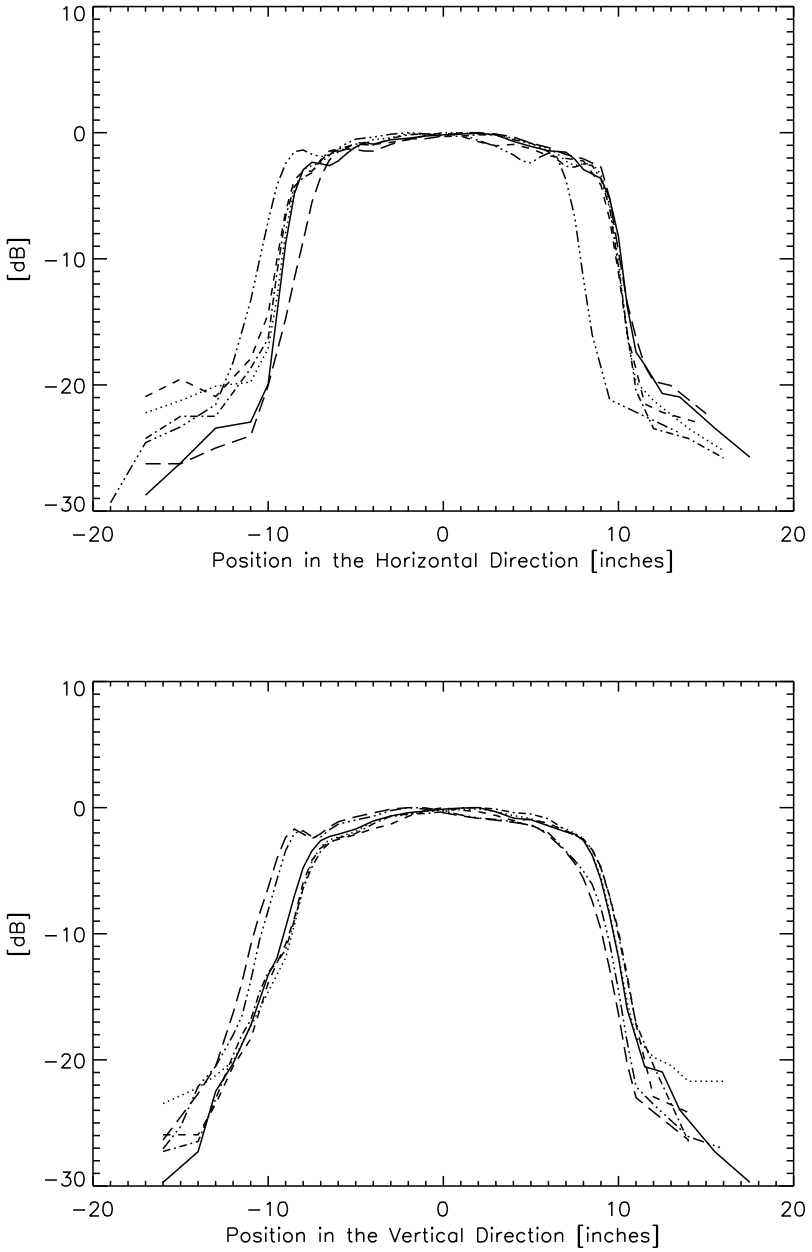

Figure 3.12: The two plots show slices through the beams at the position of the secondary mirror for the 2.1 mm optics. The slices are through the center of the beam. The beams of six bolometers are plotted, showing that the beams overlap well on the secondary, as designed.

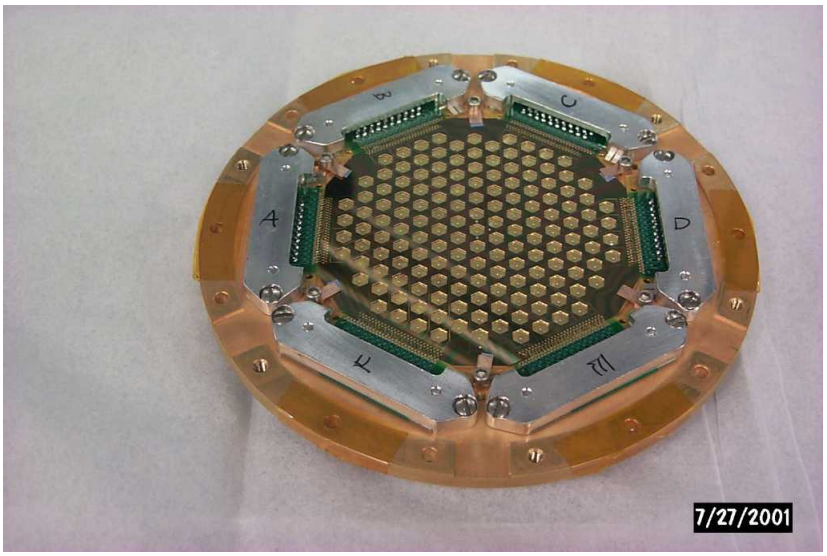

Figure 3.13: The Bolocam detector wafer after being mounted and wire bonded to the connectors for each hextant.

similar assuming a 100% detector yield. Because of the low achieved yield it was not advantageous to use all the bolometers with 0.85 fλ feedhorns, but the regular every other bolometer pattern did not take advantage of many bolometers that were working. We decided on a compromise, in which a pattern of 1.45 fλ horns was created that allowed 30 working bolometers to be coupled to the incoming radiation. This was the arrangement with optimal mapping speed. A schematic of the array with the active bolometers highlighted with blue circles is shown in Figure 3.14.

Once the feedhorn design was finalized, the parameters of the bolometers could be measured. In the previous chapter the various parameters that describe the operation of a bolometer were discussed. A quick review is presented before the parameters for Bolocam are given. The resistance of a bolometer depends on the temperature as follows:

$$R_{bolo} = R_0 e^{\sqrt{\frac{\Delta}{T_{bolo}}}} \tag{3.1}$$

where R_{bolo} is the resistance of the bolometer, T_{bolo} is the temperature of the bolometer, and R_0 and Δ are the bolometer parameters that depend on the properties of the thermistor. R_0 and Δ are measured by measuring the resistance of the bolometer at various temperatures and fitting to the equation. G_{300mK} is the thermal conductivity

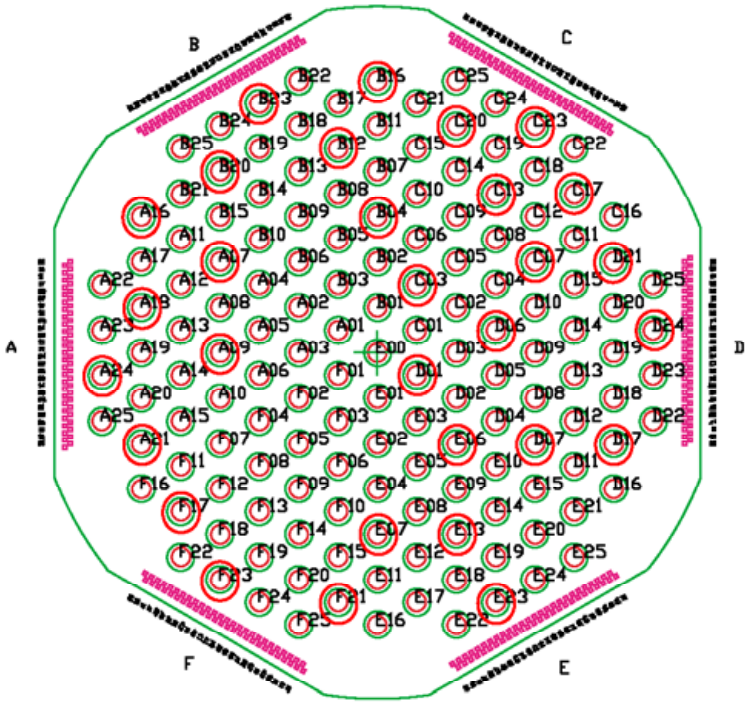

Figure 3.14: A schematic of the array including all the bolometer names. The active bolometers are highlighted with a red circle.

Parameter	median	RMS scatter
G_{300mK} [pW/K]	78.5	6.0
R_0 [Ohms]	119	28
Δ [K]	39.9	1.5

Table 3.1: Bolometer parameters for the 2.1 mm science array

of the bolometer to the thermal bath referenced to 300 mK, and is described by the equation

$$\frac{dP}{dT_{bolo}} = G(T_{bolo}) = G_{300mK}\left(\frac{T_{bolo}}{300mK}\right)^{\beta} \tag{3.2}$$

where P is the power dissipated on the bolometer, T_{bolo} is the bolometer temperature, and β is the power law index that depends on the specific bolometer. G_{300mK} is measured by taking a load curve of the bolometer with no incident optical power and measuring power vs bolometer temperature using the known values of R_0 and Δ. This data can then be fit to equation 3.2 to determine the value of G_{300mK}.

The bolometer parameters R_0, Δ, and G_{300mK} were calculated for all of the working bolometers using these techniques. The results are shown in Table 3.1.

3.4.1 Optical Efficiency

The optical efficiency is the ratio of power entering the dewar within the bandpass to the power detected by the bolometers. In the background dominated noise limit high optical efficiency reduces the time required to detect an astronomical signal. Bolocam's optical efficiency is limited principally by the Lyot stop, which blocks 50% of the signal. This sacrifice in optical efficiency is required in order to form beams on the primary mirror that do not include the surrounding ground. Absorption and reflection by the optical filters also contribute to reduced optical efficiency.

In order to measure the optical efficiency we make a differential measurement instead of trying to calibrate the absolute power incident on the bolometers. Load curves are taken with the dewar looking into 77 K and 300 K loads. Both loads are eccosorb [6], a foam, manufactured by Emerson & Cuming, that is designed to radiate as a black body at microwave frequencies, and are large enough to fill the beams at the dewar window. The 300 K load consists of a block of eccosorb at room temperature. The 77 K load is a block of eccosorb immersed in liquid nitrogen. Dry nitrogen is blown across the dewar window during the 77 K load curves to prevent water condensing on the window and reducing the optical efficiency.

The difference in power entering the dewar between the two loads is easily calculated by integrating the black body surface brightness given by the Planck function for each temperature within the average bandpass measured with the FTS. The surface brightness, with units of $[Wm^{-2}Hz^{-1}sr^{-1}]$, must be multiplied by the throughput to give the power spectral density in $[W/Hz]$. In this case the throughput is given by the wavelength squared (λ^2) which we can write as $(c/\nu)^2$ in order to integrate over frequency. The bandpass is normalized so that the maximum transmission is one, and is then integrated to give the difference in power,

$$P_{300K} - P_{77K} = \int_0^\infty (c/\nu)^2 B_\nu(\nu, T_{300K}) f(\nu) d\nu - \int_0^\infty (c/\nu)^2 B_\nu(\nu, T_{77K}) f(\nu) d\nu \quad (3.3)$$

where $B_\nu(\nu, T)$ is the black body brightness as a function of frequency at temperature

[6] http://www.eccosorb.com

T, ν is frequency, and c is the speed of light, the bandpass, $f(\nu)$ is normalized so that the maximum transmission is unity.

The difference in power detected by the bolometer between the two loads is calculated using the load curve. The resistance of the bolometer and the electrical power applied is determined for each point on the load curve. The resistance of the bolometer depends on the total power incident, electrical as well as optical. At a point on each load curve where the resistance is equal the the total power is also equal. Any difference in applied electrical power must be equal to the difference in incident optical power at constant resistance. Since the difference between incident optical power is constant throughout the load curve any point of equal resistance can be used to measure the difference in power. Figure 3.15 shows two load curves with a 300 K and 77 K load respectively. The difference in electrical power at constant resistance is shown by the grey arrow. The optical efficiency is just the ratio of this difference in power to the difference in power calculated in equation 3.3. The median optical efficiency for the 2.1 mm optics is $\eta = 0.154$, with a standard deviation from the median of 0.010.

3.4.2 Optical Loading

To finish characterizing the Bolocam detectors and optics we measure the average optical loading on the bolometers during normal operation on the telescope as one of the first tasks after mounting Bolocam on the CSO. Optical loading is measured using the same technique as the optical efficiency. By comparing load curves taken with zero optical loading to those taken during normal observing conditions, the absolute loading can be calculated. By mounting an aluminum blank above the feedhorns at 300 mK the optical loading is reduced to negligible. The loading at 2.1 mm was found to be 6.7 pW. The optical loading is usually quoted in terms of an equivalent Rayleigh-Jeans temperature. Using the optical efficiency calculated above, the power

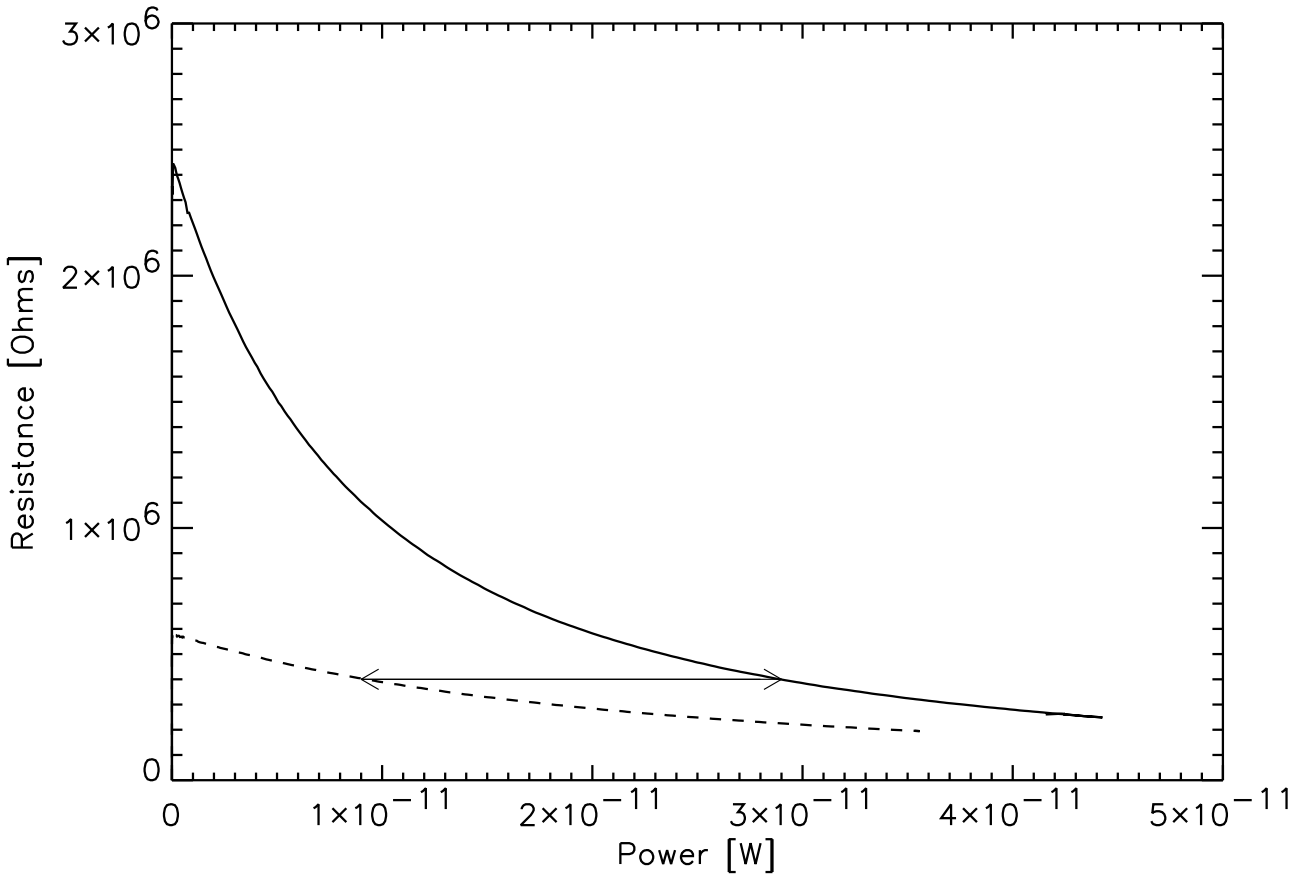

Figure 3.15: Load curves looking into at 300 K (dashed line) and 77 K (solid line) optical loads. The power difference at a given resistance is shown by the grey arrow.

incident on the bolometers can be converted to a temperature T

$$T = \frac{P}{2k_B\eta\Delta\nu} \tag{3.4}$$

where P is the incident optical power, k_B is the Boltzmann constant, η is the optical efficiency, and $\Delta\nu$ is the effective bandwidth. Applying equation 3.4 to the power difference calculated for the 2.1 mm observing run conditions gives 6.7 pW = 87 K.

We can calculate the loading we expect from the atmosphere as

$$T_{loading} = T_{atm}\left(1 - e^{-\tau_z}\right) = 16K \tag{3.5}$$

where T_{atm} is the temperature of the atmosphere which we take to be 275 K, and τ_z is the optical depth of the atmosphere at zenith, which is discussed in more detail in Chapter 5. We take $\tau_z = 0.06$ in normal observing conditions. Previous work at the CSO found the loading from the telescope to be equivalent to approximately 30 K (Holzapfel et al. 1997). We therefore anticipate the total loading on the bolometers to be 45 K. The measured value of 87 K is suspiciously high, and prompted further testing.

If the optical loading measured does not come from either the atmosphere or the telescope, it should come from inside the dewar. We tested for any excess loading contribution from inside the dewar by comparing the power difference at constant resistance between dark load curves and those taken with a 77 K optical load. This measurement parallels the optical efficiency measurement described above, but is an absolute measurement. Using the optical efficiency already measured, we can calculate the expected optical loading from a 77 K load P_{77K}.

$$P_{77K} = \eta \int_0^\infty \left(\frac{c}{\nu}\right)^2 f(\nu) B_\nu(\nu, T_{77K}) d\nu \tag{3.6}$$

where η is the optical efficiency, $(c/\nu)^2$ is the throughput, $f(\nu)$ is the measured bandpass, and $B_\nu(\nu, T_{77k})$ is the black body brightness at temperature T. The power difference between dark load curves and those with a 77 K optical load will be equal to

this expected optical loading plus any additional loading from inside the dewar. The excess loading measured for the 2.1 mm filter stack is 4.2 pW = 56 K. This loading is comparable to the total expected atmosphere and telescope loading of 45 K. The increased loading will increase the photon noise of the bolometers, and degrade the performance of the instrument.

In order to improve the instrument performance for subsequent observing runs the source of the excess load within the dewar was investigated. The obvious suspects for the origin of the excess loading are the filters. Any filter that emits in band more than designed could cause significant excess loading on the bolometers. A filter with reduced transmission in band would have a corresponding increased emissivity which would cause in band emission. All the 2.1 mm metal mesh filters were removed and sent to the Astronomy Instrumentation Group in Cardiff for testing. The transmission of all filters were tested at various positions on the filter. The filter mounted at 77 K with a 255GHz low pass cut off was found to have transmission as low as 70% in some areas. Test measurements of this filter before shipping only tested transmission a the center of the filter, and missed this problem. The temperature of the filter was measured during a test cool down of the dewar and found to be approximately 120 K. The combination of poor transmission in band and the high temperature due to poor heat sinking led to the excess load. Improved filters with more efficient heat sinking have been installed for future Bolocam observing.

3.5 Electronics

The Bolocam electronics are designed to provide DC stable bolometer signals, allowing us to readout the total power on each bolometer instead of making a differential measurement. In order to provide a stable readout Bolocam employs an AC bias circuit with lock in amplifiers to read the modulated signals. A diagram of the electronics chain for a single bolometer readout is shown in Figure 3.16. The details are described below.

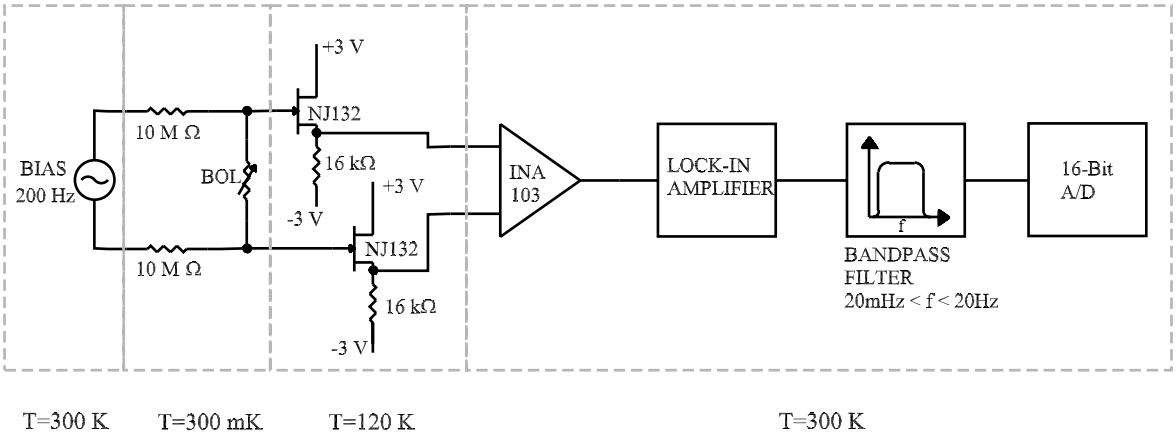

Figure 3.16: Overview of the Bolocam electronics for one bolometer channel

3.5.1 Bias Circuit

The bolometers are current biased with an AC signal. The AC bias voltage is provided from outside the dewar. The two load resistors have a much higher resistance than the bolometer during operating conditions and ensure that the current stays constant even with varying bolometer resistance. The AC bias signal is produced using a AD630 chip which outputs a square wave signal. This signal is then filtered to produce a sine wave bias signal. The bias is supplied separately to each hextant of bolometers, allowing a small level of fine tuning to suit bolometer parameters.

The load resistors are surface mounted on G10 fiberglass circuit boards. There is one board per hextant, each with 48 resistors of 10 MΩ. Each circuit board is mounted in an aluminum box that is attached under the 250 mK stage in the wedding cake assembly. Because there is no temperature difference between the load resistor modules custom made cables with copper wires are used to connect the two.

3.5.2 Cold Electronics

The wires leading from the bolometers have an impedance of a few MΩ, and voltages of a few millivolts. This current is insufficient to drive the preamplifiers. The solution to this problem is to place cold amplifiers, JFETs in the case of Bolocam, in the electronics chain as soon as possible after the bolometers. JFETs are source following

transistors that preserve the signal voltage but reduce the impedance of the lines from a few MΩ to approximately 500 Ω. The JFETs are mounted on alumina circuit boards, with one board per hextant. Each board is contained within an aluminum box that provides some thermal shielding. All six JFET modules are mounted on a G10 structure that suspends them above the 4 K cold plate. The G10 structure is heat sunk to the 77 K warm finger in the center of the cold plate. The JFETs self heat to their operating temperature of 130 K. The final temperature of the JFETs is controlled by the width of a heat strap directly between the 77 K warm finger and the JFET modules. The entire G10 and JFET module structure is enclosed within a aluminum box. This box shields the rest of the dewar from the thermal radiation from the JFETs, and provides a base for the wedding cake assembly. While the JFETs operate at 130 K the surface of the enclosure is 6 K during operation.

Because there are 144 electronics channels with 2 wires per channel running from the 130 K JFETs to the 250 mK load resistors, the thermal conductivity of the wiring is a concern. Each hextant has one cable with consists of 24 twisted pairs of 0.003 inch manganin wires which are woven into ribbon cables. Each cable extends approximately 10 cm between 250 mK and the 6 K JFET box, which produces a heat load of less then $18\mu W$ for all six cables. The cables within the JFET box that run from 130 K to the 6 K box walls are heat sunk to the G10 structure with Teflon tape at 0.5 cm increments. With this care taken with the cabling the fridge operates at 250 mK during telescope loading conditions, 50 mK lower than requirements. The same woven manganin wire cables are used to take the signals from the JFET output to the dewar vacuum shell.

3.5.3 Warm Electronics

After the signals exit the dewar they enter the preamplifier box that is attached to the dewar. The preamplifiers apply a gain of 500 and a bandpass filter centered on the bias frequency. Once the signal has been amplified, it is routed to the lock in amplifier via 25 feet of twisted pair shielded cables. The lock in amplifiers are based

on a design by Viktor Hristov. The amplifiers use a AD630 chip to demodulate the signal and produce a DC bolometer voltage. DC signal is split in two, with one signal being read out by the Data Acquisition System, and the other sent to a high pass filter with a 16mHz cut off and additional gain of 100 to produce an AC coupled signal with a total gain of 1.16×10^5. The AC signal is used for all data analysis. The DC signal gives a direct measure of the bolometer resistance, but suffers from bit noise. The high pass filter allows us to increase the gain without exceeding the ± 10 V range of the data acquisition system. The lock in amplifiers were found to be extremely sensitive to temperature changes, producing excessive 1/f noise if operated outside their enclosures.

Both the DC and AC coupled bolometer signals are recorded by the Data Acquisition System (DAS).

3.5.4 Microphonic Response

Microphonic response is increased bolometer signal due to the vibration of the high impedance signal wires. Microphonics generally occur at well defined frequencies due to the resonances in the dewar. The bias frequency should be far from any of these frequencies, therefore the microphonic pick up of the system must be measured. This measurement is done using DC bias. The output from the preamplifiers is recorded using a spectrum analyzer. We measure the spectrum of one bolometer channel at a time, which, without any vibrations of the dewar, is dominated by the 1/f noise of the JFETs and 60Hz pickup. There are two methods for vibrating the dewar at a range of frequencies, providing an impulse to the dewar, or vibrating the dewar with a chirp signal. The impulse method is simple to achieve with a rubber mallet hit to the side of the dewar, which causes vibrations at all frequencies, but the amplitude is hard to control. The chirp signal method requires a speaker mounted on the dewar fed by the chirp output provided by the spectrum analyzer, and provides repeatable vibrations at a known amplitude. Figure 3.17 shows the microphonic response of bolometer A07 with the chirp signal input. The bias frequency was chosen to be 130 Hz, in a clear

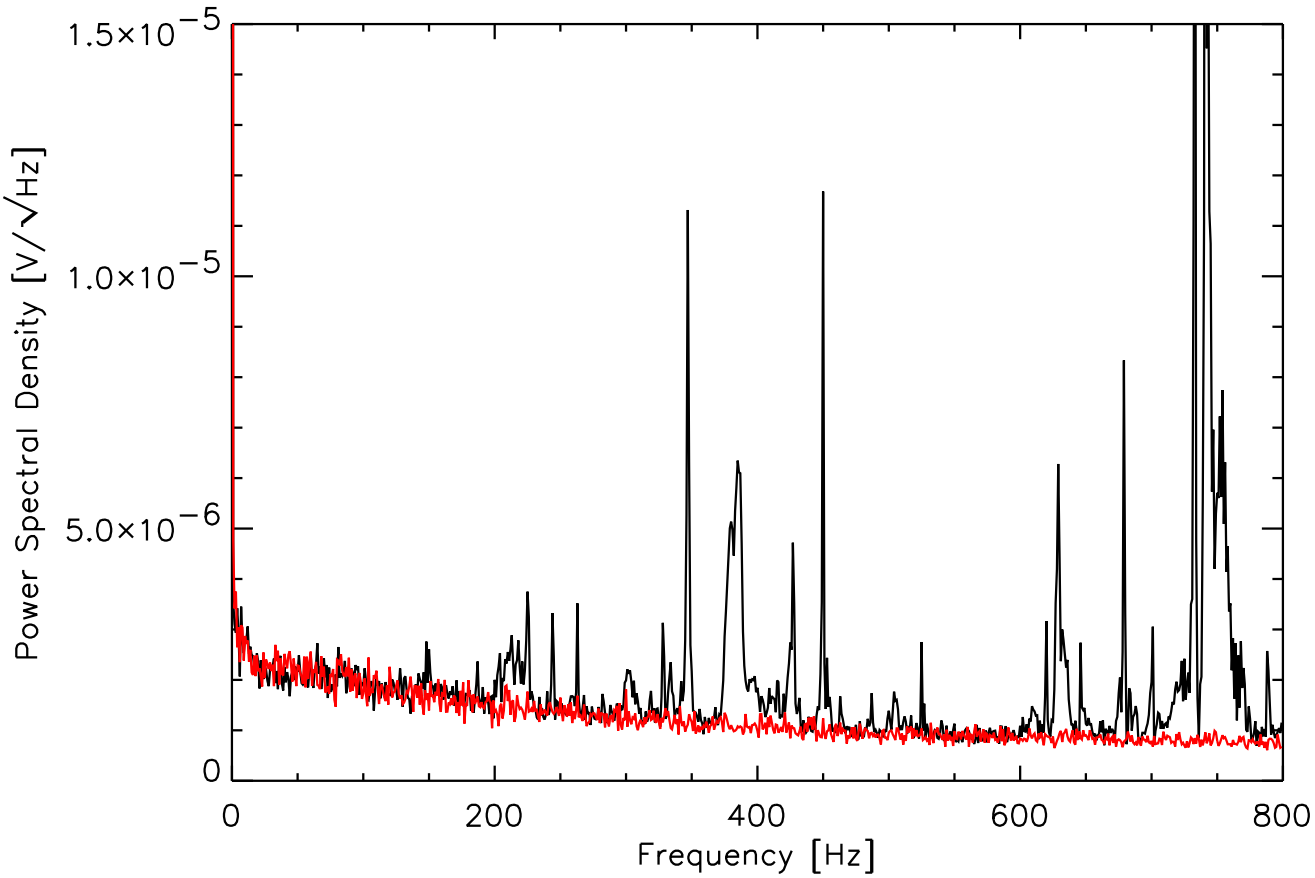

Figure 3.17: The black line is the microphonic response of bolometer A07 with a chirp signal vibration input to the dewar. The red line is the same measurement without the chirp signal. The bias frequency is chosen to be 130 Hz, which is near the center of a flat area. Any lower frequencies and the 1/f noise of the JFETs become evident.

area of the spectrum. It is also possible to reduce the microphonic response of the system by preventing the vibrations in the high impedance signal cables. We used Teflon tape to tie the signal cables to the wedding cake assembly vespel legs at 0.5 cm intervals. This not only reduced the remaining microphonic response at 130Hz, but also heat sunk the wires resulting in a lower final fridge temperature.

3.6 Noise Performance

3.6.1 Electronics Noise

The noise of the preamplifiers and lock-in amplifiers must be measured to determine their contribution to the total noise of the system. During the Winter 2001 observing run there were only 30 active bolometers and 144 electronics channels. The signal from each active bolometer was sent to two different preamplifiers and subsequent electronics. The only difference in the two signals is the noise acquired from the warm electronics chain. By taking the difference of the two signal channels warm electronics noise can be measured. The resulting power spectral density is shown in Figure 3.18. The electronics noise is flat to low frequency and much below the level expected for photon noise. The 1/f noise from the lock-in amplifiers during operation was negligible indicating extremely stable temperatures inside the enclosures. The average total amplifier noise measured during the winter 2001 observation run was $6nV/\sqrt{Hz}$.

3.6.2 Dewar Rotator Noise

Rotating the dewar introduces spikes into the bolometer signals due to step like increases or decreases in the DC bolometer levels. A sample spike is shown in Figure 3.19. Spikes can be either positive or negative and vary greatly in magnitude. Slowing the speed of the rotation reduces the magnitude of the spikes, but does not eliminate them. If the spikes were due entirely to microphonic or RF pickup from the motor, they would always be positive as the bolometers warmed. The most likely culprit of the rotator spikes is optical loading changes as the dewar rotates, which would explain both positive and negative spikes. There is little difference in optical loading from the sky with the small change in elevation due to the rotation. The optical loading changes more likely come from inside the dewar. If there is any sag in the wedding cake assembly, the amount of loading from the shielding inside the dewar would change with rotation as a different part of the array would sag downward due

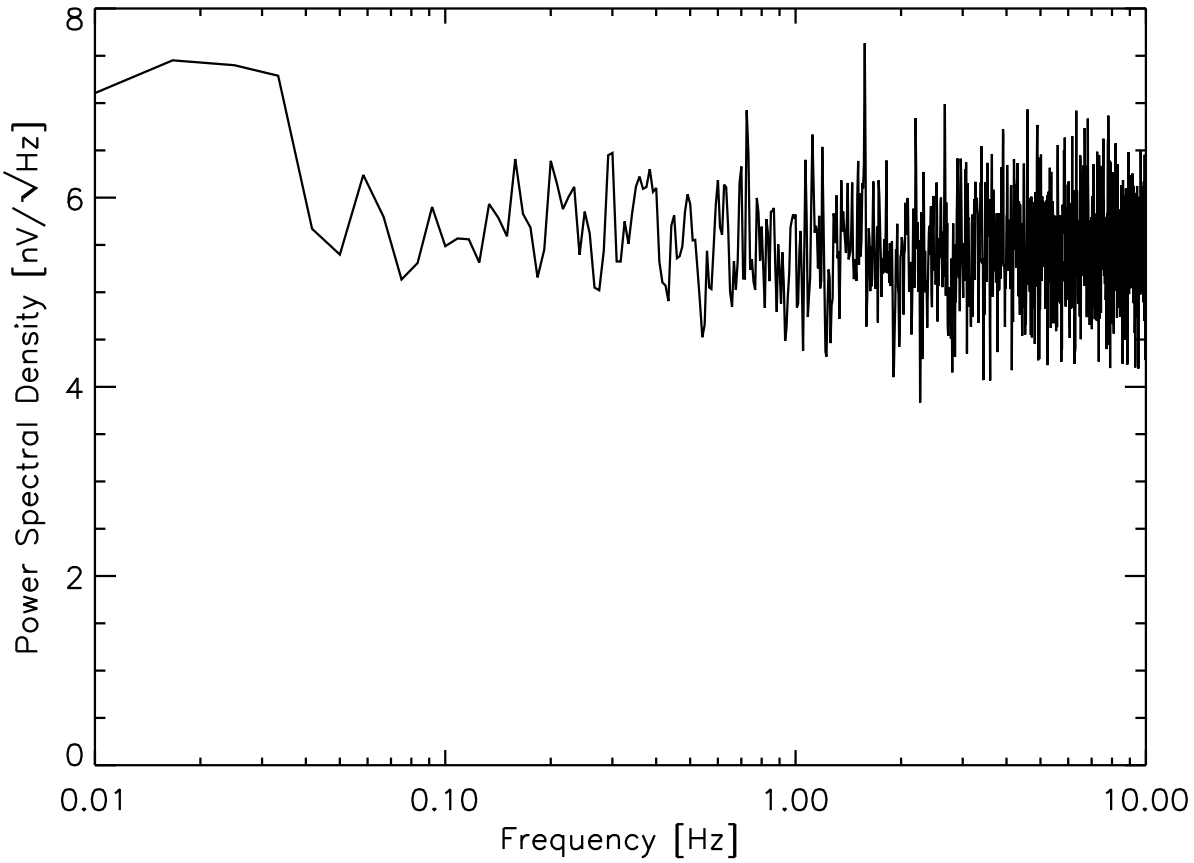

Figure 3.18: The total electronics noise measured by differencing two channels carrying the same bolometer signals on different warm electronics channels.

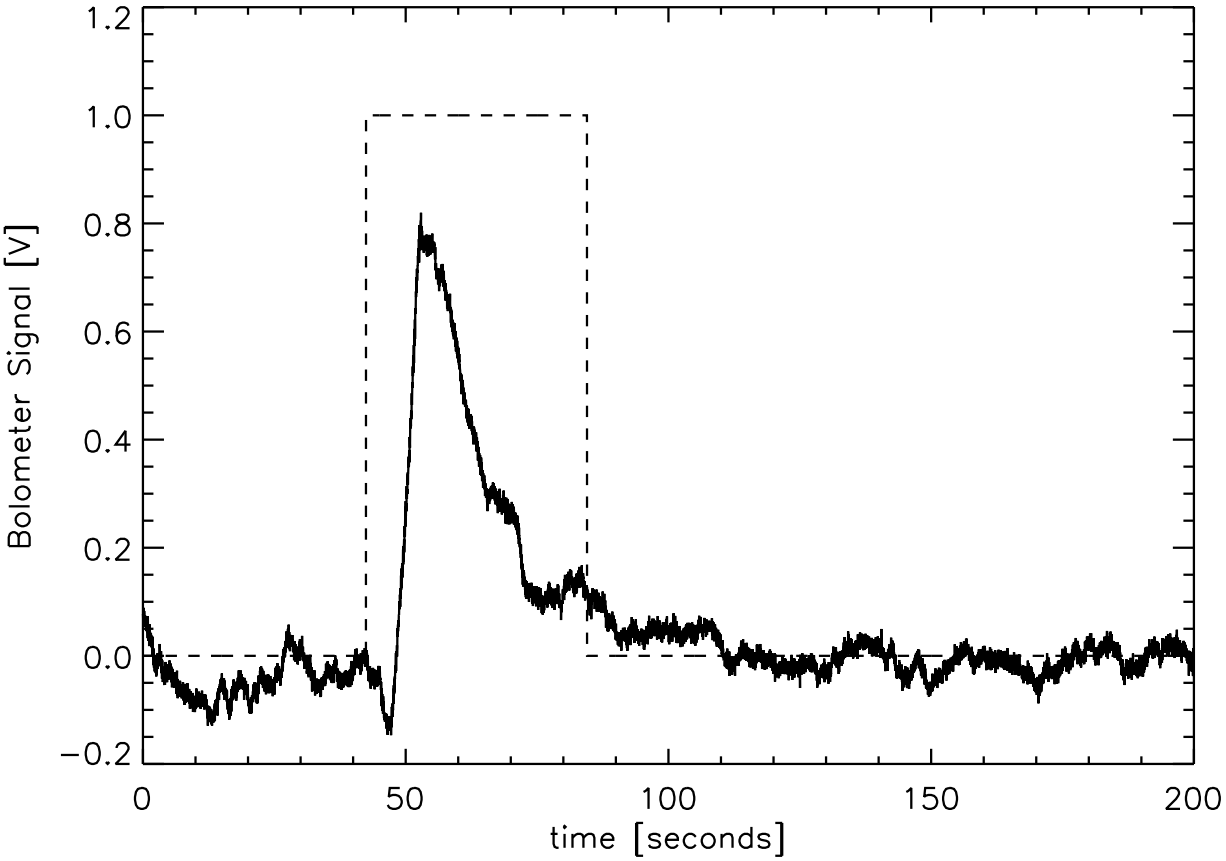

Figure 3.19: A sample rotator spike shown in the raw time ordered data of the A06 bolometer. The dotted line is 0 when we are observing, and 1 when the telescope is waiting for the dewar rotator to finish.

to gravity.

Our main concern with the 2.1 mm Winter 2001 data is to remove the spikes from the data. Our first strategy is to reduce the number of times the dewar rotates. Since the parallactic angle changes relatively slowly we reduced the number of times the dewar rotates during an observation. The second strategy is to removes the effects of the rotation when it does occur by fitting an exponential decay to the spike and subtracting that from the data. This strategy is described in more detail in Section 5.4.4.

3.6.3 Detector White Noise

Bolocam's expected high-frequency noise performance can be calculated using the noise definitions described in Chapter 2 and the operating conditions measured during the 2.1 mm observing run. The low frequency noise is dominated by sky noise, which is a very different beast that will be tackled in Chapter 5. The high frequency noise provides a lower limit to the bolometer noise which is achieved only if the sky noise is completely removed. Comparing the expected high frequency noise to that measured during the observing run we can test the validity of the bolometer parameters and operating conditions calculated in this chapter.

First, a quick review of the relevant noise equations discussed in Chapter 2. Photon noise equivalent power

$$NEP_{\gamma}^2 = 2Qh\nu_0 + \frac{Q^2}{\Delta\nu} \tag{3.7}$$

where Q is the optical power incident on the bolometer, h is the Planck constant, ν_0 is the central frequency, and $\Delta\nu$ is the average bandpass width. Phonon noise is given by the following

$$NEP_{phonon}^2 = 4k_B T_{bolo}^2 G \tag{3.8}$$

where k_B is the Boltzmann constant, T_{bolo} is the bolometer temperature, and G is the

bolometer thermal conductance. Johnson noise is given as

$$NEP^2_{Johnson} = \frac{4k_B T_{bolo} R_{bolo}}{S} \tag{3.9}$$

where R_{bolo} is the bolometer resistance, and S is the responsivity of the bolometer [V/W]. The amplifier noise is given by

$$NEP^2_{amp} = \left(\frac{e_{amp}}{S}\right)^2 \tag{3.10}$$

where e_{amp} is the noise of the amplifiers measured as described in Section 3.5. The total high frequency noise is calculated by adding all these noise sources in quadrature. The total expected noise can be compared to the measured noise levels in the data (in $V/\sqrt{Hz}$) using the responsivity of the bolometers as derived from the absolute calibration (2.0×10^8 V/W as discussed in Section 4.4.2).

In order to calculate the phonon and Johnson noise, the temperature and resistance of the bolometers must be known. The resistance is easily calculated using the DC bolometer and bias monitor signals. Once the resistance is known, the temperature can be determined using the temperature resistance relation for the bolometers

$$R = R_0 e^{\sqrt{\frac{\Delta}{T}}} \tag{3.11}$$

where R_0 and Δ are the bolometer parameters presented in Table 3.1. The average DC bolometer voltage during normal operating conditions is 2.7mV, taking the system gain of 1161 into account. The bias for these observations was 19.8mV. This gives a bolometer resistance of 2.7 MΩ, and $T_{bolo} = 396$ mK. To calculate the photon noise we use the total optical power incident on the bolometers, shown in Section 3.4.2 to be 6.7 pW. The amplifier noise is measured as described in Section 3.6, and was shown to be $6nV/\sqrt{Hz}$.

The total expected noise level is calculated as follows,

$$NEP_{total}^2 = NEP_{gamma}^2 + NEP_{phonon}^2 + NEP_{Johnson}^2 + NEP_{amp}^2 \quad (3.12)$$

$$= 3.8 \times 10^{-33} + 6.8 \times 10^{-34} + 2.9 \times 10^{-33} + 9.0 \times 10^{-34} \frac{W^2}{Hz} \quad (3.13)$$

$$NEP_{total} = 9.1 \times 10^{-17} \frac{W}{\sqrt{Hz}} \quad (3.14)$$

Figure 3.20 shows the power spectral density of data taken during normal operating conditions. The sky noise has been removed, and the white noise is above about one hertz. We can see from this plot that the white noise is approximately $7 \times 10^{-17} W/\sqrt{Hz}$. The median noise level measured over the course of the 2.1 mm Winter 2001 observations was $1.03 \times 10^{-16}\ W/\sqrt{Hz}$, with a standard deviation of $2.0 \times 10^{-17}\ W/\sqrt{Hz}$. This is in good agreement with the expected noise, giving us confidence in the measured bolometer parameters presented in this chapter.

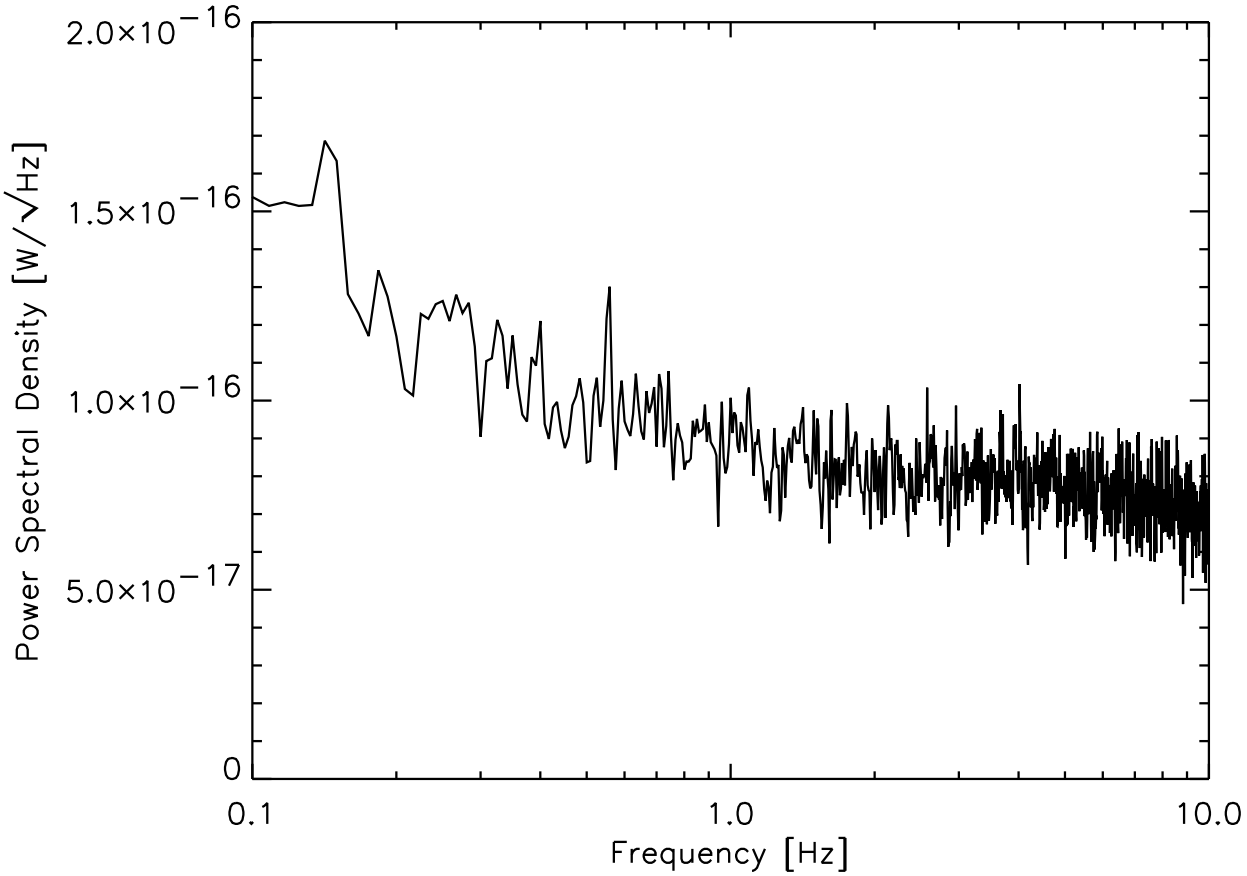

Figure 3.20: The power spectral density of data taken during average observing conditions. The white noise is above approximately 1 Hz, and corresponds well to the expected white noise level.

Chapter 4

Observations

The data discussed in this work were taken during the winter 2001 Bolocam observing run at the Caltech Submillimeter Observatory (CSO). The observations used the 2.1 mm filter configuration, and were scheduled to take place from December 14, 2001 to January 4, 2002. Unfortunately a blizzard delayed our start date to December 20 2001. Previous to this Bolocam had a one week engineering observing period at the CSO, during May of 2000 using the 1.4 mm filter configuration. The engineering run used the prototype detector array and was designed to test all aspects of the instrument and its integration into the CSO. The winter 2001 observing run was the first designed to take science data, and used the improved detector array referred to as the 2001 science array. In the previous chapter the optical configuration for the 2.1 mm observing run was described, consisting of 30 active bolometers and $1.4f\lambda$ feedhorns. Bolocam has subsequently had 3 observing runs at 1.1 mm which will not be discussed here.

4.1 Blank Sky Observations

This work focuses on the blind cluster survey work done during the 2.1 mm winter 2001 observing run. We chose two regions of blank sky, each one degree in right ascension (RA) and half a degree in declination (dec), separated by about 7 hours in right ascension, to make up our survey area. The separation of the two target areas allowed observations of both regions in a single night. We looked for areas

that would be visible during our allotted observing time, had low dust emission, and were studied at other wavelengths, especially in X-rays by the XMM-Newton satellite. Combining X-ray and SZ data for any cluster candidates from our survey tests the current cluster models. Any optical/IR data will be used to verify cluster candidates and select galaxies for spectroscopic redshift measurements. The two chosen regions were the Lynx field and the Subaru Deep Survey field 1 (SDS1).

4.1.1 Lynx

The Lynx field is centered at 08h49m12s, +44d50m24s (J2000). It has low dust emission, with 100 μm flux of 1.33 MJy/sr, and has been observed by the XMM-Newton X-ray observatory with a 150 ksec exposure in three slightly offset pointings. There is a small area of optical coverage by Kitt Peak in the area covered by Bolocam. The coverage by various wavelengths is shown in Figure 4.1.

Three galaxy clusters have already been identified in the Lynx field. CIG J0848+4453 was discovered by Stanford et al. (1997) in the Kitt Peak near-IR survey of the area. RX J0848.9+4452 and RX J0848.8+4456 were identified by Rosati et al. (1999) as cluster candidates in the ROSAT Deep Cluster Survey. Our Lynx field is centered on these three clusters.

Figure 4.2 shows the actual coverage achieved on the Lynx field during the observing run. There is a total of 50.6 hours of on source integration on this field, and 60.3 total hours of observations, over the course of 13 nights.

4.1.2 Subaru Deep Survey 1

The Subaru Deep Survey 1 (SDS1) field is centered at 02h18m00s -5d00m00s (J2000). The field is named after the optical/IR survey being undertaken by the Subaru telescope that has a field centered at these coordinates. The field has low dust emission, with 100 μm flux of 1.17 MJy/sr. SDS1 is also part of the XMM Survey Science Project which includes a 100 ksec exposure at the center of the field, and 50 ksec exposures on the surrounding pointings, along with optical and spectroscopic followup.

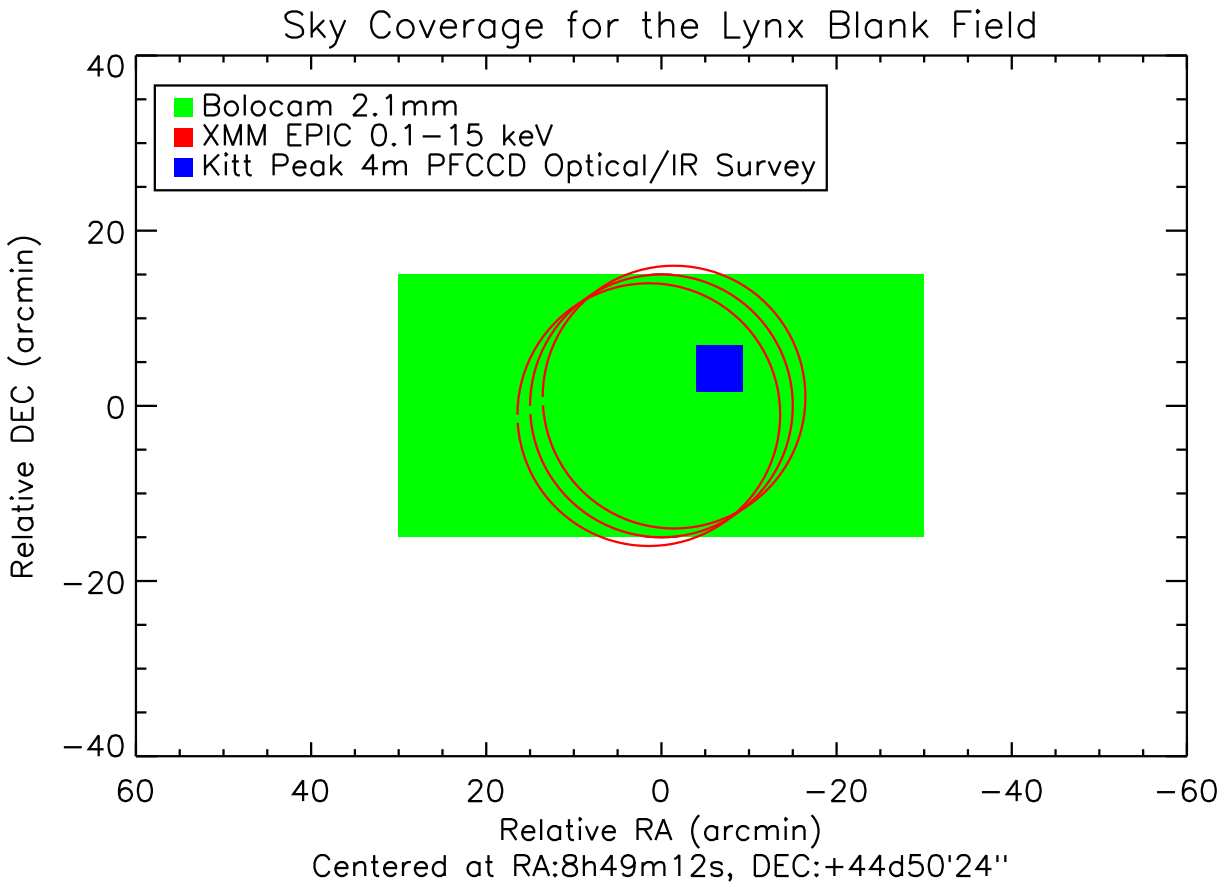

Figure 4.1: The Bolocam coverage for the Lynx field is shown in green, the red circles are XMM pointings, and the blue area is optical coverage by Kitt Peak.

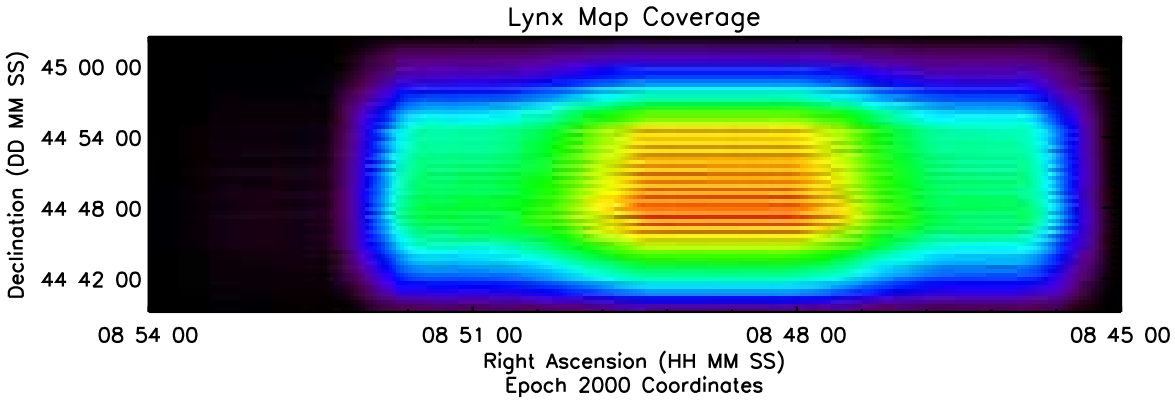

Figure 4.2: The achieved coverage of the Lynx field. We executed both long one-degree RA scans as well as short half-degree RA scans, resulting in an area of increased coverage in the center of the map.

The coverage of the SDS1 field at various wavelengths is shown in Figure 4.3.

No clusters have yet been identified in the SDS1 field. Figure 4.4 shows the achieved coverage of this field with Bolocam. It consists of a total of 35.3 hours of on source integration, and 41.7 total hours of observation time over 11 nights. The smaller integration time compared to the Lynx field is due to the fact that we could not observe SDS1 for two nights due to the proximity of the Moon.

4.2 Scan Strategy

Bolocam observes in two main modes, drift scanning and rastering. In drift scan mode the telescope is held stationary, and the sky rotates overhead moving the array across the target area at a constant declination. In this mode the scan must be at a constant declination (along right ascension) and can only move in one direction. After the sky has rotated past the target area, the telescope must reposition the array ahead of the target so it may rotate overhead again. The main advantage of the drift scan method is the fact that the telescope is stationary during observations, which means

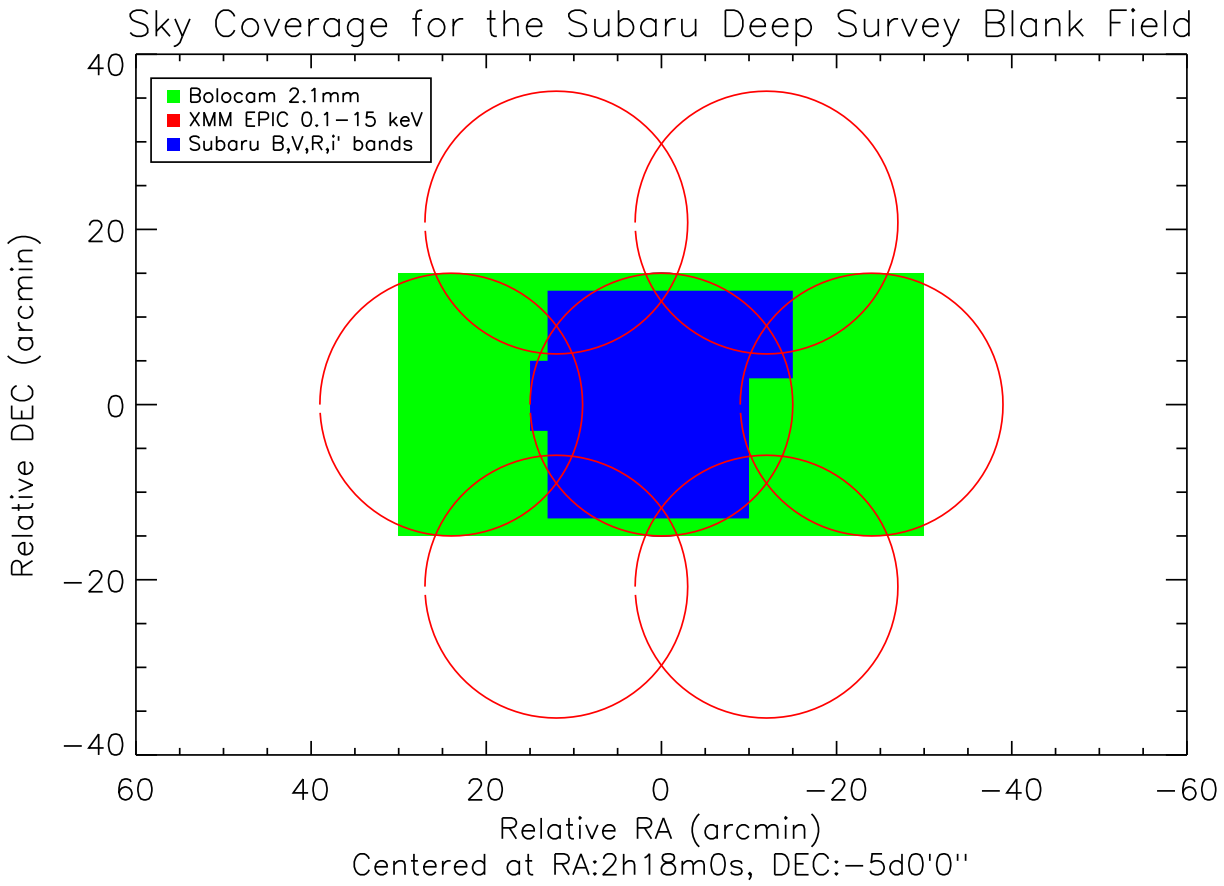

Figure 4.3: The Bolocam coverage for the SDS1 field is shown in green, the red circles are XMM pointings, and the blue area is optical/IR coverage by Subaru in their Deep Survey after which this area is named.

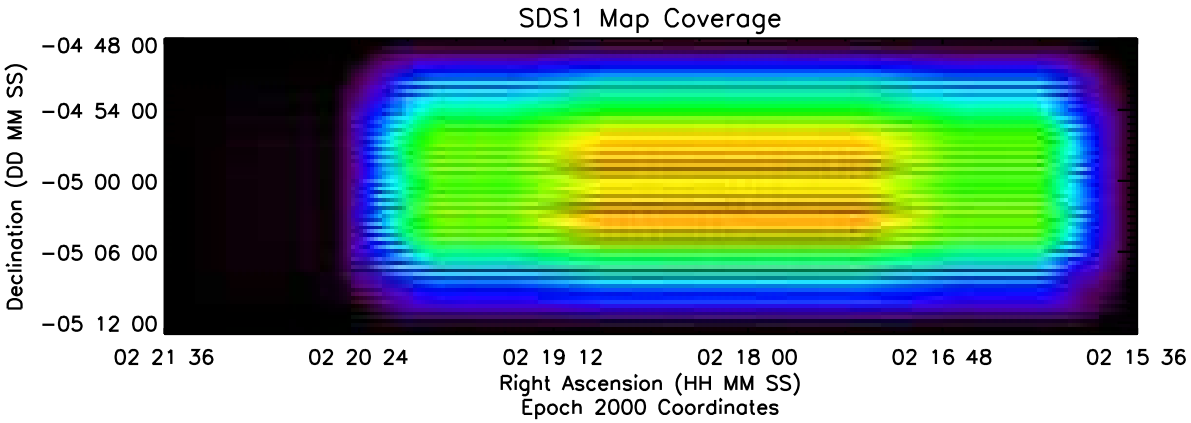

Figure 4.4: The achieved coverage of the SDS1 field. As in the Lynx field a combination of short half degree scans and long one degree scans in RA resulted in an area of increased coverage in the center of our map.

that any side lobe structure will be constant, allowing for a lower noise measurement of small signals like the CMB. There are a few problems with this scan strategy. The observing efficiency (time on source vs. total time to complete an observation) is low for drift scan mode as the telescope must move considerably between sub-scans. The other draw back is that the signal is at very low frequencies. The sky moves at $15\cos(\delta)$ arcsec/sec where δ is the declination angle.

The raster mode allows more options in scan strategy. In raster mode the telescope itself actively moves the array across the target area. In this way we can recreate the drift scan mode, but with a faster scan across the target. Observing efficiency can be improved by moving in both directions across the target area, requiring less movement of the telescope between sub-scans. By moving the telescope during an observation we are changing any side lobe pick up that may be present, and we may be introducing microphonic noise. These concerns are addressed in section 5.6. The residual low frequency noise in the data is dominated by weather conditions, so any extra noise from side lobe pick up that may be present is not detectable with the current data.

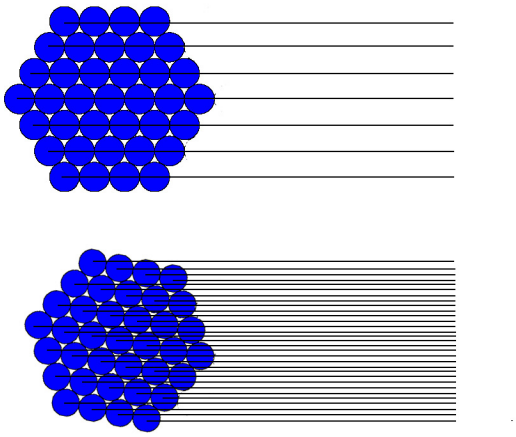

Figure 4.5: The diagram assumes that the scan direction is horizontal and shows the path of the center of each pixel. The top diagram is the worst possible coverage. The bottom diagram is at the optimal angle to the scan direction, and the coverage is obviously much improved.

In either drift scan or raster mode a single pass across the target area is called a sub-scan. During the winter 2001 observing run we used only drift scan and raster scan at constant declination, so all sub-scans were along right ascension. In order to cover the entire target area multiple sub-scans were performed with offsets of 1/3 of an array (180 arcsec) in declination between them. Full coverage of the target area in this way is called a scan. To complete a full observation two more scans are performed with small ($\pm$ 30 arcsec) deviations in declination from the original scan, for a total of 3 scans per observation. The number of sub-scans per scan depends on the size of the target area being covered, for the 1/2 x 1 degree blank sky target areas there are 9 sub-scans per scan leading to a total of 27 sub-scans per observation. Some of the Lynx and SDS1 observations were limited to 1/2 degree in right ascension to give an area of higher coverage in the center of the maps.

The coverage for each sub-scan depends on the angle of the array with respect to the scan direction (which is always right ascension). If the rows of the hexagonal array are aligned with the scan direction then the sub-scan will have coverage gaps in declination between the array rows. If the array is rotated slightly then the coverage along declination will be greatly improved. We can see this depicted in Figure 4.5. The problem is to determine the optimal angle to rotate the array with respect to

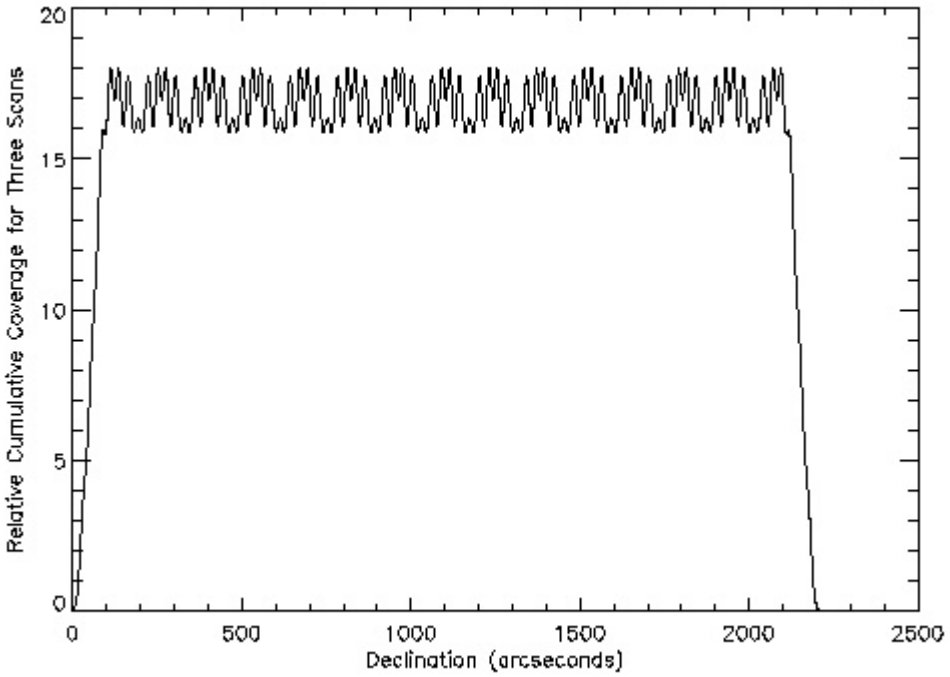

Figure 4.6: The coverage vs. declination with the dewar rotated at 10.9^o from the RA direction for each scan, using the scan strategy described in section 4.2.

the scan direction. The optimal angle is the one that produces even sampling along declination with the minimum separation of the scan lines of individual bolometers. Via geometric arguments we can write a general equation for the optimal angle based on the size of the hexagonal array:

$$\Theta = tan^{-1}(\sqrt{3}/(2N+1)) \tag{4.1}$$

where Θ is the optimal angle, and N is the number of bolometers along the edge of the hexagonal array (Glenn 2001). For the 2.1 mm configuration $N = 4$ and the optimal angle is $\Theta = 10.9^o$. If the array is rotated to be at an angle of 10.9^o with respect to the scan direction for each sub-scan we will have optimal coverage of the area. The resulting coverage vs. declination is shown in Figure 4.6. The dewar is rotated using a motor mounted to the optics box, which is discussed in section 3.1.1.

4.3 Beam Maps

The shape and size of the beams on the sky is an important part of the subsequent data analysis. Any structure detected on the sky will be convolved with the beam profile. In order to map the beams we observed Mars and several other point sources. Figure 4.7 shows the map from the Mars observation. The data from all the bolometers are mapped using only the telescope bore sight coordinates with no corrections. We should see Mars in a slightly different place for each of the bolometers. The distance of the position in the map to the actual known position of Mars gives the offset of that particular bolometer from the bore sight of the telescope. To determine the beam sizes from the Mars observations we must take the size of Mars into account. Mars is not actually a point source, and subtends 17 arcseconds on the sky during the time of the observations. The beams are found to be Gaussian as predicted with a full width half max of 59.0 arcseconds.

4.4 Calibration

During the winter 2001 2.1 mm observing run Bolocam had 30 bolometers that must all be calibrated. Calibration can be split into two main steps, relative and absolute calibration.

4.4.1 Relative Calibration

Relative calibration measures the responsivity of each bolometer relative to the average of all the bolometers, but does not compare to an absolute scale such as Kelvin. Two techniques were used to calculate the relative responsivities of each of the 30 bolometers, observations of Mars and observations of blank sky.

Mars was observed six times over the course of the observing run. Each time we took three hours of data to create a fully sampled map of Mars using the data of each of the bolometers separately. The maps for each bolometer are made, and a two dimensional Gaussian is fit to the data. The ratio of the amplitude of this fit for each

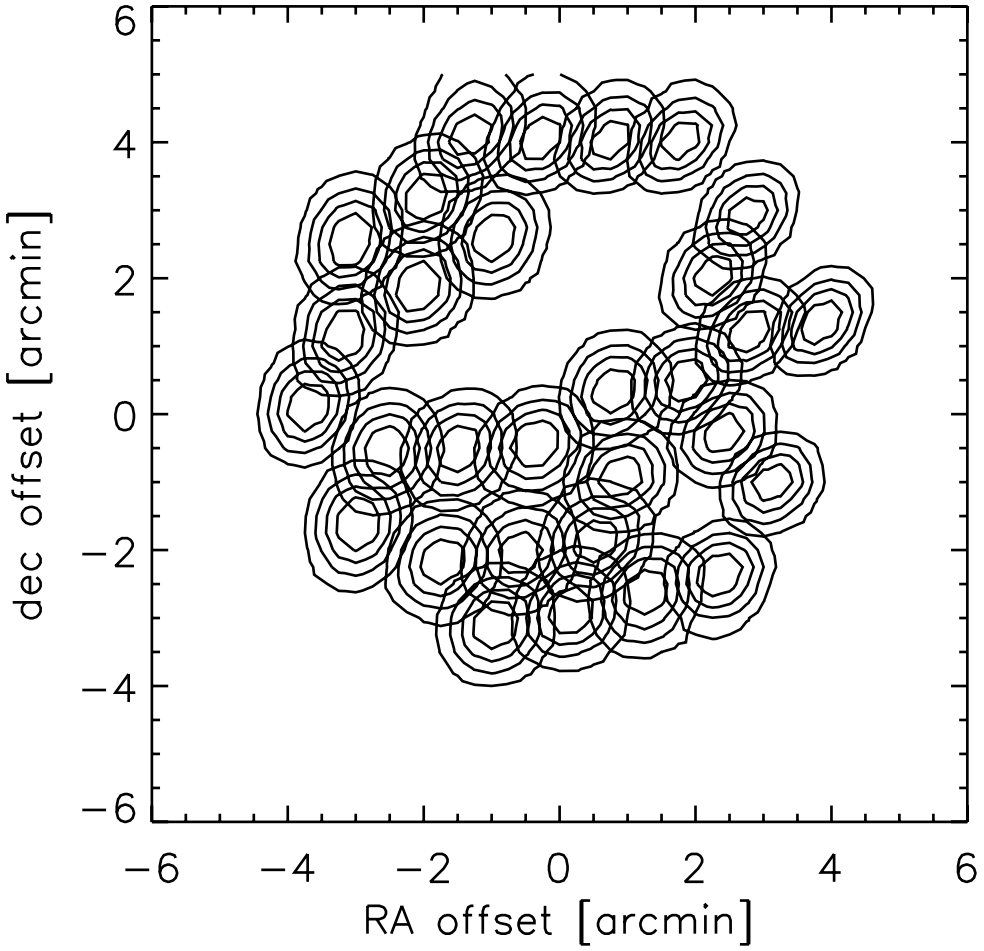

Figure 4.7: Beam map on Mars with no offset correction to show the bolometer array on the sky.

bolometer to the average is the relative responsivity. The results for each of the 30 bolometers is shown in Figure 4.8.

Relative responsivities can also be calculated using observations of blank sky. For each sub-scan in the observation a sky noise template is created by averaging the signal from each of the 30 bolometers. The astronomical signal in the blank sky data is insignificant compared to the sky noise in a single sub-scan, and therefore each bolometer should see the same signal from the sky. The sky template is scaled to fit the signal from each of the 30 bolometers using regression. The regression coefficients are the relative responsivities compared to the average. The regression coefficients are stable over the course of the observing run. The results do not change significantly between averaging the results for sub-scans for a single observation, and averaging the results for sub-scans of all the Lynx data. The regression coefficients compared to the results from the Mars analysis can be seen in Figure 4.8. We use an average of the regression coefficients over all Lynx observations as the relative responsivities to be used during making maps.

4.4.2 Absolute Calibration

The absolute calibration converts the output signal in volts to an absolute scale, in this case Kelvin CMB (K_{CMB}) or Janskys (Jy). Fortunately during the observing run in the winter of 2001 we were able to observe Mars. Mars is a primary calibration source for many submillimeter observations. The first step in the calibration is to observe Mars as described for the relative calibration. The maps of Mars were fitted to 2-D Gaussian beams. At 2.1 mm Bolocam's beams have a FWHM of approximately 60 arcsec, so we do not resolve Mars, which has a diameter of 17 arcsec. The brightness of Mars at the time of our observing run is calculated using a model based on the dielectric properties of the upper meter of the Martian surface (Rudy et al. 1987). By extrapolating this model to 2.1 mm, on December 9th, 2001 Mars had a Rayleigh-Jeans temperature of $208K_{RJ} \pm 6K_{RJ}$. Taking into account the distance to Mars on that date, our beam size, and comparing to the average bolometer responsivity the

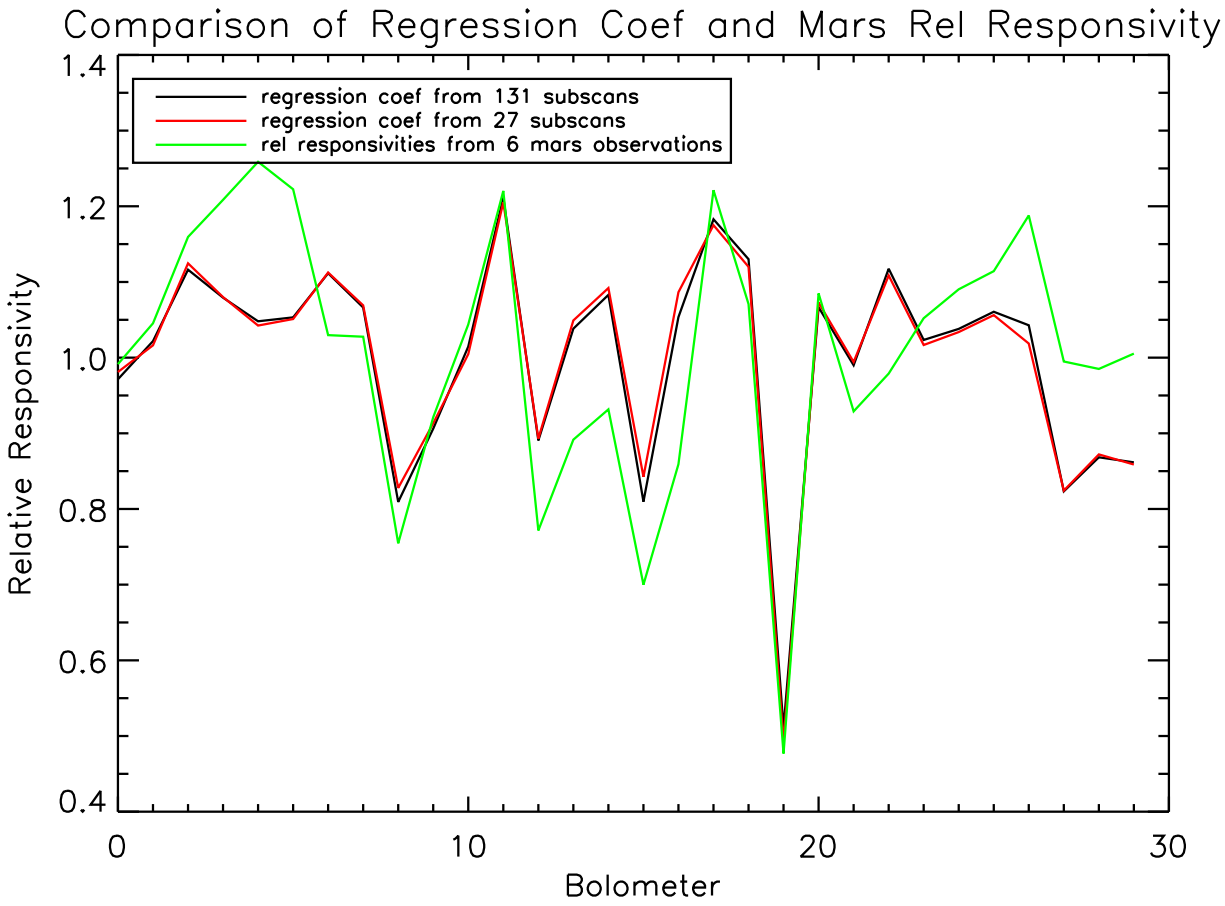

Figure 4.8: The relative responsivities of the 30 active bolometers at 2.1 mm. The green line is calculated from Mars observations. The red and black are calculated from regression coefficients during sky subtraction on blank sky. The regression coefficient values are used as the relative responsivities in all mapping.

calibration is 1.8 V/K_{RJ} (Goldin 2001). Applying the gain on the AC bolometer signal channels (1.16×10^5), and converting from K_{RJ} to Watts the bolometer responsivity is $2.0 \times 10^8 V/W$.

In order to apply this calibration to observations of the SZ effect we must convert to K_{CMB} which is the small change in temperature relative to the cosmic microwave background. The cosmic microwave background is a black body at 2.73 K, with a intensity given by

$$I(\nu, T) = \frac{2h\nu^3}{c^2(e^{\frac{h\nu}{kT_{CMB}}} - 1)} \tag{4.2}$$

where h is the Planck constant, ν is the frequency, k is the Boltzmann constant, and T is the temperature. The same intensity in given in the Rayleigh-Jeans approximation by

$$I(\nu, T) = \frac{2\nu^2 kT_{RJ}}{c^2} \tag{4.3}$$

In order to find the conversion between K_{RJ} and K_{CMB} we set the derivatives of the two intensities equal and solve for the ratio between dT_{RJ} and dT_{CMB}. The result is

$$dT_{RJ} = \left(\frac{h\nu}{kT_{CMB}}\right)^2 \frac{e^{\frac{h\nu}{kT_{CMB}}}}{e^{\frac{h\nu}{kT_{CMB}}} - 1} dT_{CMB} \tag{4.4}$$

which gives us the conversion $K_{RJ} = 0.6 K_{CMB}$. We can extend this to find the conversion from K_{CMB} to Janskys (Jy) and unit favored by radio astronomy. A Jansky is a unit of flux defined at $10^{26} W/m^2 str$. To determine the conversion between K_{CMB} and Jy we first find the intensity in Janskys and then take the derivative with respect to T_{CMB}.

$$I_{Jy}(\nu, T) = \Omega \cdot 10^{26} \frac{2h\nu^3}{c^2(e^{\frac{h\nu}{kT_{CMB}}} - 1)} \tag{4.5}$$

where Ω is the source size in steradians. Taking the derivative with respect to T_{CMB} gives us a conversion of 1 Jy = 42.8 K_{CMB}, for the Bolocam beam size.

Chapter 5

Atmospheric Noise Removal

5.1 Sky Noise Theory

Ground-based observations at millimeter wavelengths are limited by the atmosphere. The main culprit is water vapor, which absorbs, emits, and refracts at the signal wavelengths. Bolocam is located at the Caltech Submillimeter Observatory, on Mauna Kea, a high dry site, to avoid water vapor. The spectral band pass centered around 2.1 mm, is specifically designed to avoid water vapor emission lines. Even with these measures the atmospheric noise can be significant. We can consider the refraction of incoming light, attenuation of incoming light, and emission from the atmosphere seperately.

The JCMT, located next to the CSO, measures the refraction of the atmosphere using two 1.8m dishes that detect a signal from a geostationary satellite. Changes in the phase difference of this signal between the two dishes are due to turbulent water vapor refracting the signal as it passes through the atmosphere, and is interpreted as submillimeter seeing. Around midnight the seeing is typically 0.2 arcsec, and is insignificant for our 1 arcmin beam size (Archibald et al. 2002).

Attenuation by the atmosphere is accounted for by measuring the optical depth of the atmosphere in the spectral bandpass. The optical depth of the atmosphere changes on short time scales, so frequent measurements are necessary. The best way to do this is to perform sky dips, which are described below in section 5.2.

Emission by the atmosphere within our spectral band produces thermal radiation

at levels several orders of magnitude larger than the astronomical signal, and is the dominant source of noise for Bolocam. In addition to this increased optical load on the bolometers the atmospheric brightness can have significant temporal and spatial variations. Any spatial variations will be converted to temporal variations in the time ordered data due to our observing strategy described in section 4.2. The dominant variations are due to the water vapor in the atmosphere. Because the water vapor is close to condensation it is not well mixed with the rest of the atmosphere. This produces spatial variations of the emission at millimeter wavelengths that are blown through the beam by the prevailing wind conditions. The turbulence in the atmosphere produces variations in the water vapor that can be described by a Kolmogorov model (Kolmogorov 1941). This model assumes that turbulent energy is injected into the atmosphere on large scales due to convection and wind shear. This energy cascades down to smaller and smaller scales until it is dissipated on scales of 1 mm by viscous forces (Lay et al. 2000). This results in a power spectrum of the sky noise in the time ordered data that is approximately $1/f$. By measuring the power spectrum of the raw Bolocam data we can see in Figure 5.1 the $1/f$ sky noise, which is rolled off at low frequencies due to the AC filter in the electronics. At high frequencies the noise is dominated by white photon noise. Bolocam does not chop the secondary mirror to produce modulation of the bolometer signals, therefore, the signal we are attempting to measure is buried in the sky noise. A point source will cross our 60" FWHM Gaussian beams at 15"/second during a drift scan, taking 4 seconds. The frequency of such a signal in the time stream will be 80 mHz, therefore, we must remove the sky noise contaminating our signal. The methods we have used to remove sky noise from Bolocam data are presented in sections 5.5.1, 5.5.2, and 5.6.

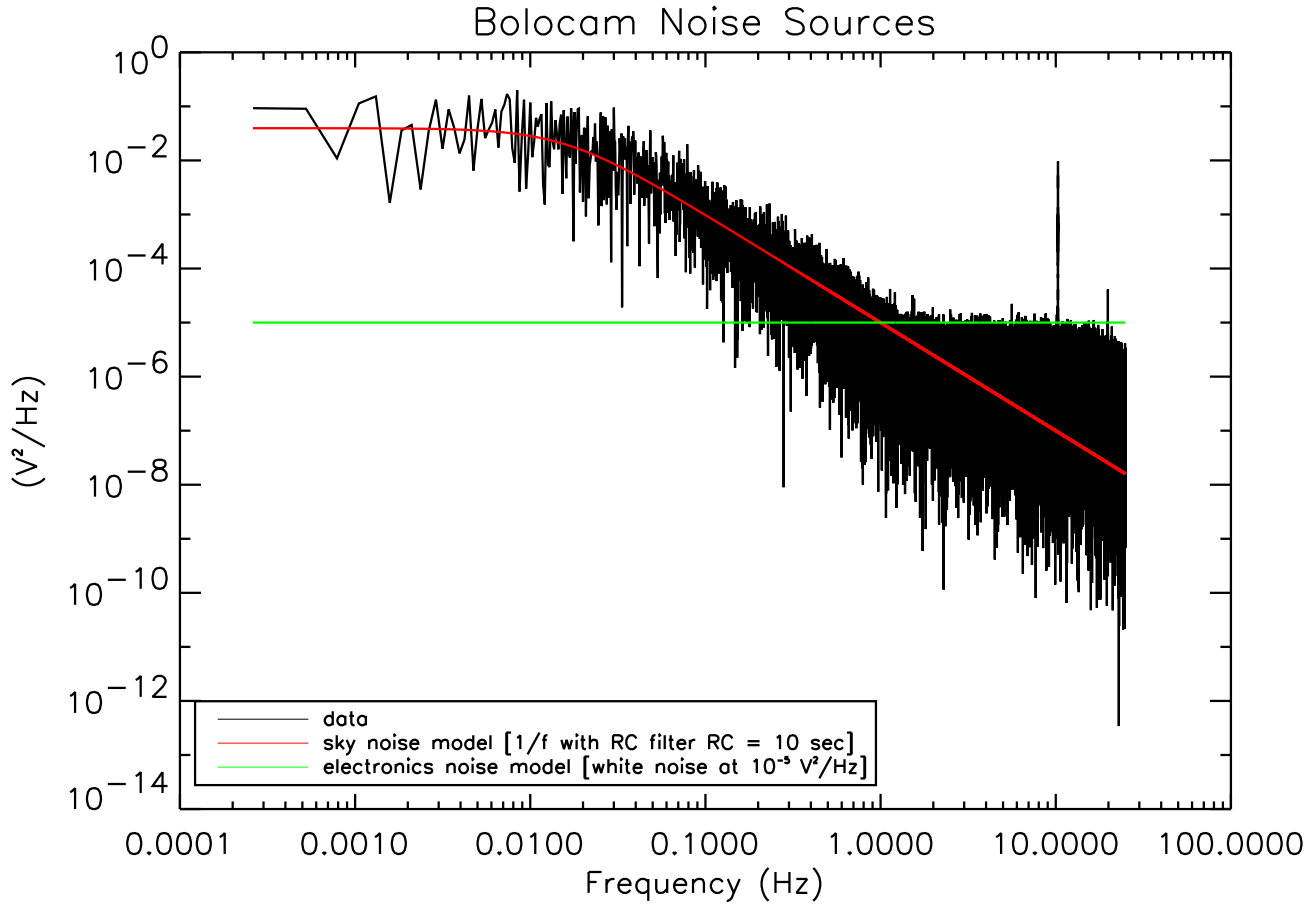

Figure 5.1: The noise sources present in the Bolocam raw data. The low frequency noise has a spectral index of -1, and rolls off at very low frequency due to the AC filter in the electronics.

5.2 Sky Dips: Measuring the Optical Depth of the Atmosphere

The optical depth of the atmosphere is a way of characterizing the attenuation of the signal. The best way to measure the optical depth is by performing a sky dip. During a sky dip the telescope is pointed to various elevations between zenith and 30 degrees. As the telescope moves to lower elevation angles Bolocam looks through larger amounts of atmosphere and the loading on the bolometers increases. The DC level of the bolometer directly measures the loading on the bolometer. Measuring the loading at various elevations allows us to calculate the optical depth of the atmosphere. There are several contributions to the loading at any given elevation. Written as a temperature the optical loading is given by

$$T_{obs}(\zeta) = T_{dewar} + \epsilon_{telescope} T_{telescope} + (1 - \epsilon_{telescope}) T_{atm} \left(1 - e^{-\tau/cos\zeta}\right) \qquad (5.1)$$

where ζ is the elevation, T_{dewar} is the loading from inside the dewar, $\epsilon_{telescope}$ is the emissivity of the telescope, $T_{telescope}$ is the temperature of the telescope, T_{atm} is the temperature of the atmosphere, and τ is the optical depth of the atmosphere. The loading from astronomical signal is negligible compared to the other terms and is ignored for these purposes. If we plot loading on the bolometers vs elevation angle we can fit this equation to the data and determine τ. In practice we plot the average DC bolometer signal vs elevation of the telescope, and convert the temperatures in equation 5.1 to volts in order to fit τ. The results of this fit for a skydip in average observing conditions is shown in Figure 5.2.

Performing a skydip with Bolocam takes approximately half an hour. Because they are so time-consuming skydips cannot be performed at the frequency necessary to track changes in the attenuation due to the atmosphere. The CSO employs a τ monitor that measures the optical depth in a small spectral band at 225GHz every five minutes. The method is a skydip, but the τ monitor is a dedicated instrument separate from the telescope and can measure τ continuously without using telescope

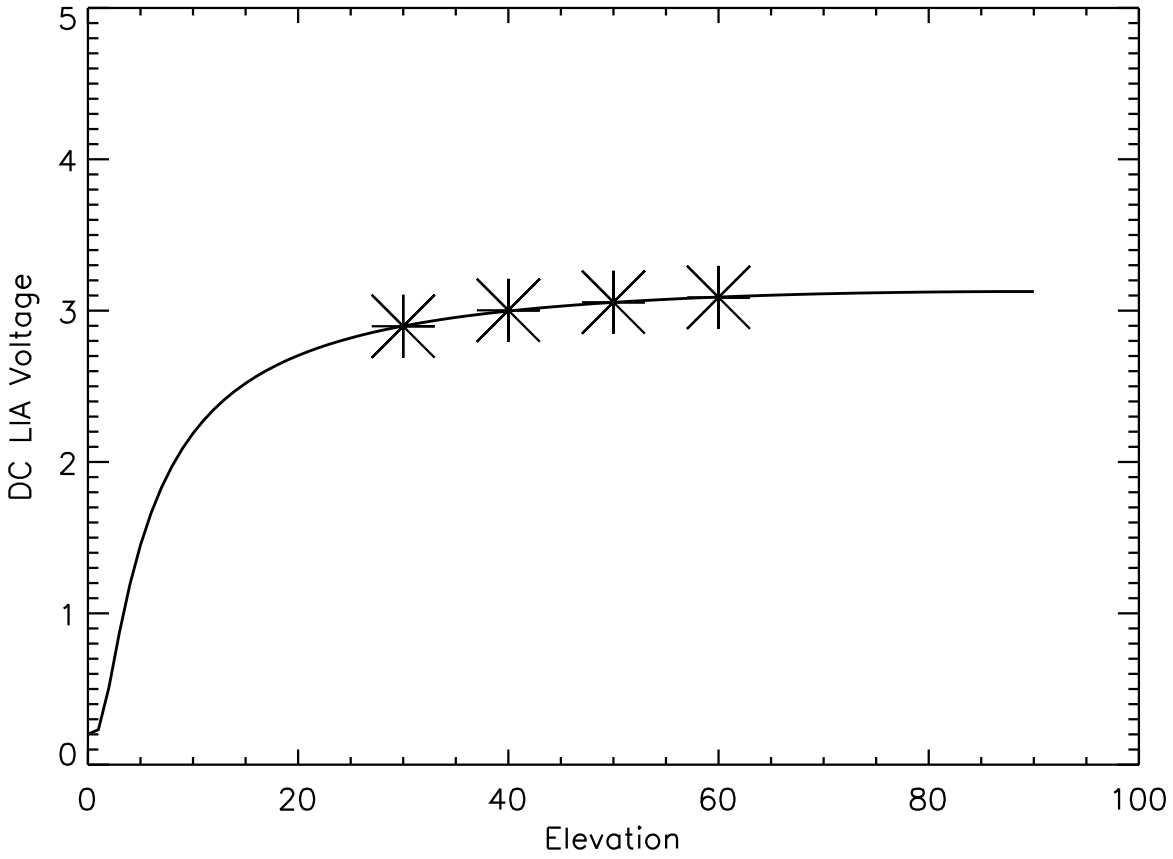

Figure 5.2: The solid line shows the model fit to the DC bolometer signals vs elevation. Only elevations between 30^o and 60^o are used because we cannot observe lower, and higher elevations lead to distortions of the telescope dish that introduces errors into the result. This fit results in τ at 2.1 mm = 0.081, with an average $\tau_{225GHz} = 0.129$

time. We perform a skydip with Bolocam approximately once a day to calibrate to the CSO τ monitor. At 2.1 mm $\tau_{band} = 0.66\tau_{225GHz}$ based on the average of all the skydips.

5.3 Observing Weather Conditions

The Bolocam 2.1 mm observing run lasted from December 22nd, 2001 to January 4th, 2002. The week before December 22nd was also assigned to Bolocam, but a blizzard prevented us from reaching the summit during that time. Figure 5.3 shows the τ monitor results for the entire observing run. For most of the run $\tau_{225GHz} \approx 0.1$, which is good observing weather for extra-galactic sources. Figure 5.4 shows the relative sensitivity of the bolometers vs τ. There is no significant increase in the noise measured for optical depths above 0.1.

5.4 Data Preparation

Before we can attempt to remove sky noise the data must have some preliminary processing. The data collection set up at the telescope is described in section 3.1.2. The raw data consist of three types of files, each one minute long, one containing the bolometer signals, one containing the telescope pointing information, and the last containing miscellaneous signals needed for analysis.

5.4.1 Merging

The first step is to combine the three autonomous data files into a more convenient file format. We chose the netCDF file format for Bolocam because of its versatility and ease of use. The netCDF file format was developed and is maintained by Unidata[1]. It is a self-describing format, which means that descriptions of the data are contained within the data file itself. The format is easily expanded and changed as Bolocam matures, new data arrays have already been added to the format in recent observing

[1]http://www.unidata.ucar.edu/packages/netcdf

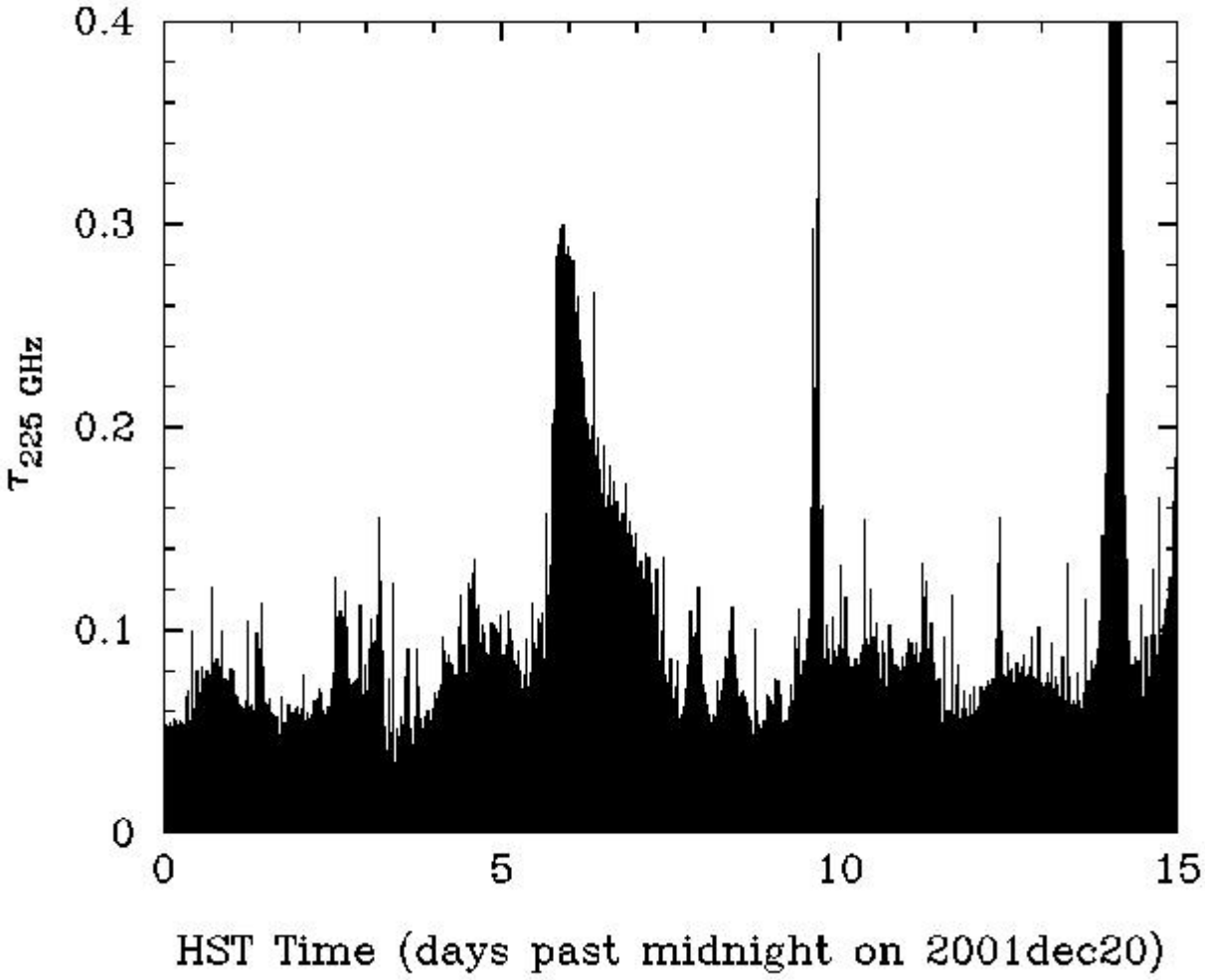

Figure 5.3: Atmospheric optical depth measured by the CSO τ monitor over the course of the Bolocam observing run. Plot courtesy of the CSO tau plotter.

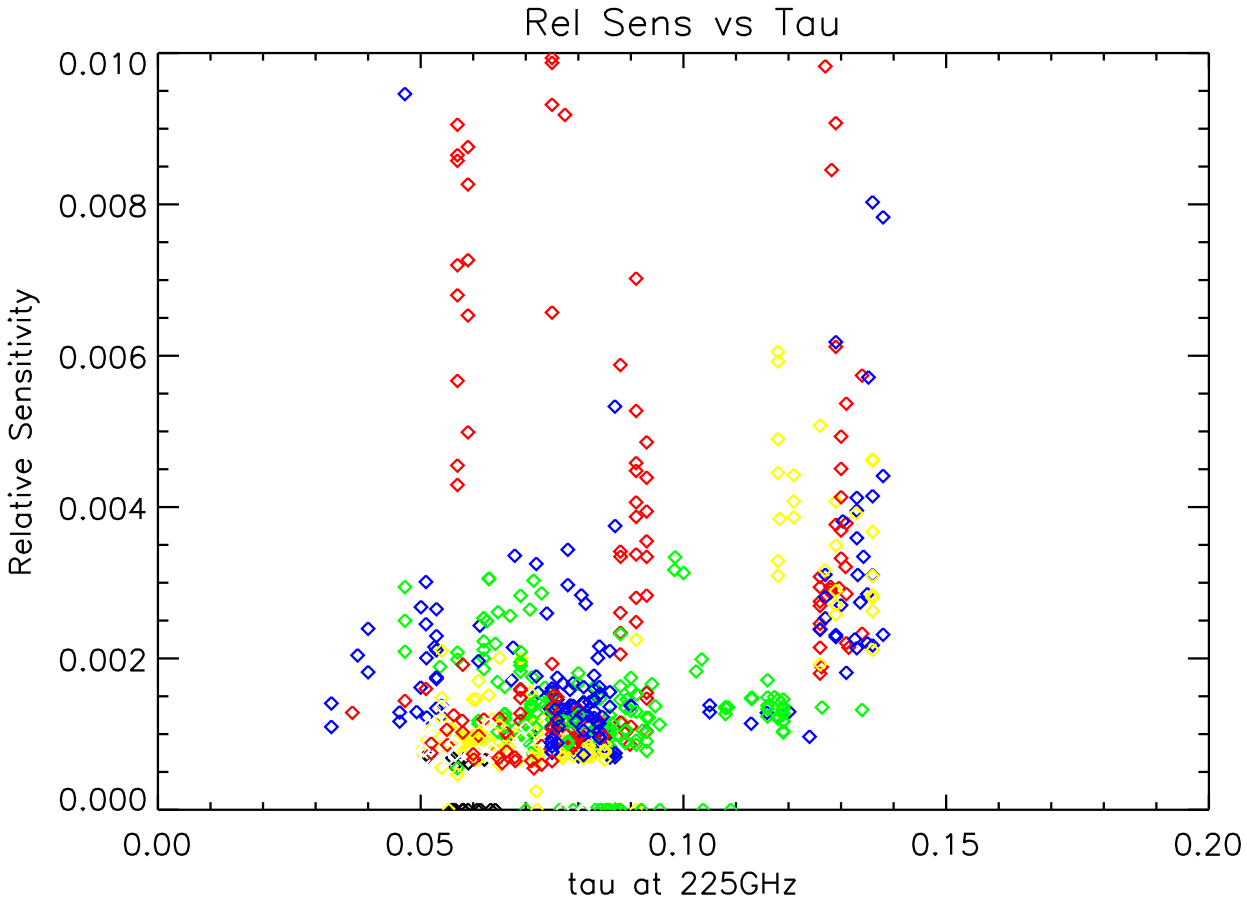

Figure 5.4: The relative sensitivity vs tau shows the relative noise in the signal band vs the optical depth of the atmosphere. No significant increase in noise is seen for $\tau \geq 0.1$. Each dimond corresponds to a sub-scan, and the different colors correspond to different observations.

runs. The format is also easily written and read from both C and IDL, making data analysis easier. The merging program combines the three raw data files into one netCDF format file that are each one hour long. These one hour long files are then sliced into individual observation files based on the observation number which is incremented every time a new observing macro is started. The individual observation files, referred to as raw data files, are now ready for cleaning.

5.4.2 Data Cleaning Organization

We use the IDL programming language to clean and analyze the Bolocam data. The language was chosen for its ease of use and simple graphing interface. All data cleaning is organized under a data cleaning wrapper program. This program reads in all the appropriate data from the raw file, creates a file to place the cleaned data into, and runs the requested data cleaning programs on the data. These programs are referred to as modules. The advantage of running the cleaning in the modular fashion is that expanding and modifying the cleaning procedure becomes trivial, and all the data reading and writing is dealt with separately from the actual cleaning. Once the data has been read and organized by the cleaning wrapper program there are several preliminary cleaning steps we need to perform before the sky removal.

5.4.3 Spike Removal

Although the bolometers are designed to have minimal cosmic ray cross section, they still occur in the time stream and must be removed. A sample cosmic ray hit is shown in Figure 5.5. The spikes in the time stream are identified by taking a point wise difference of the data, essentially the derivative. The cosmic ray rises and falls over only a small number of samples and therefore appears as a significant deviation in the differenced data. In order to automatically flag the spikes we determine the standard deviation of the differenced data, and make a cut at 5σ. Once the beginning of the spike as been identified this way, we calculate how many samples to flag using the bolometer time constant and the peak height of the spike. We assume an exponential

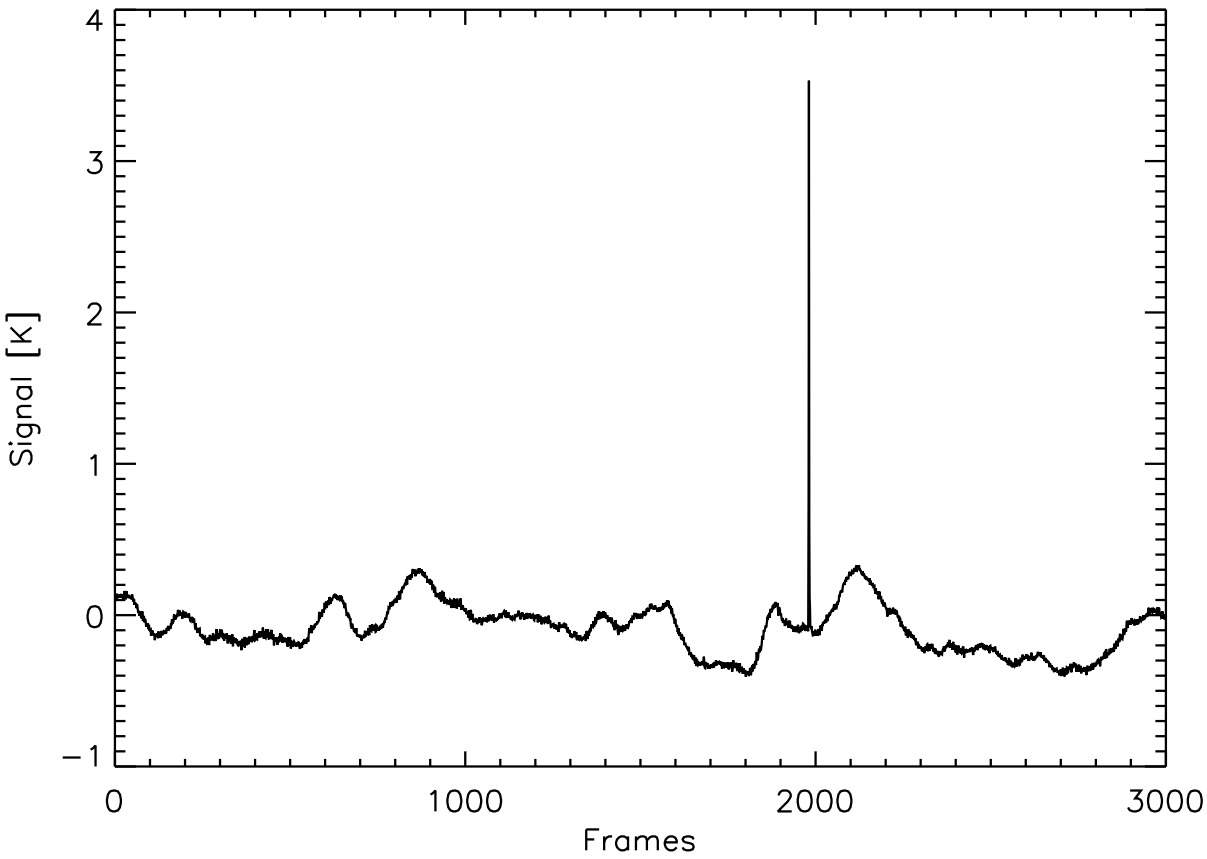

Figure 5.5: Signal trace of a single bolometer sub-scan including a cosmic ray hit.

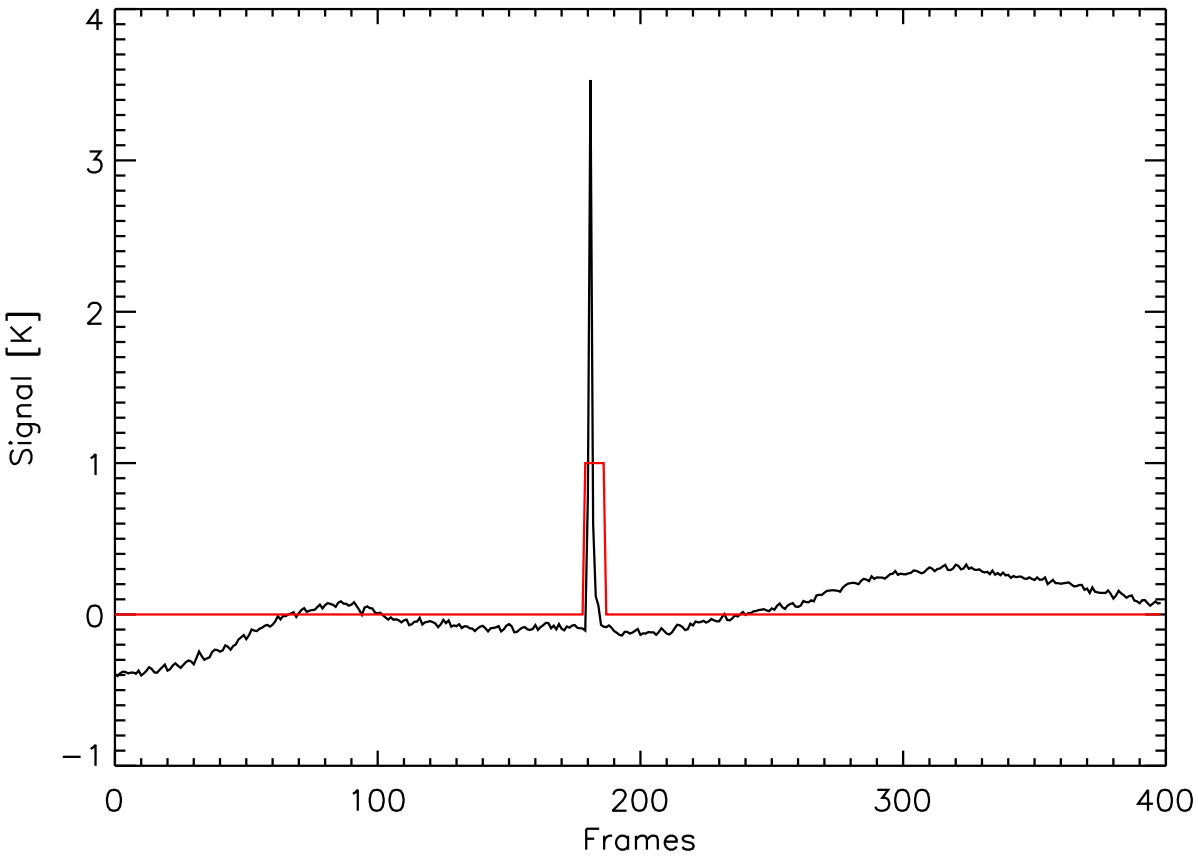

Figure 5.6: Cosmic ray hit, with data flagged by the spike removal algorithm.

decay and cut the data until the voltage returns to a nominal level. Figure 5.6 shows a close up of the cosmic ray hit in Figure 5.5 with the flagged data indicated. Spike removal flags only a very small portion of the data.

5.4.4 Exponential Decay Removal

Bolocam observes the sky by either drift scanning or rastering across a target area, (see section 4.2). The data is organized into sub-scans, which are a single pass across the area. In between sub-scans the telescope is accelerating, and we may rotate the dewar to compensate for parallactic angle. During this inter-scan time the DC level of the bolometers may change slightly due to these activities, see section 3.1.1. The

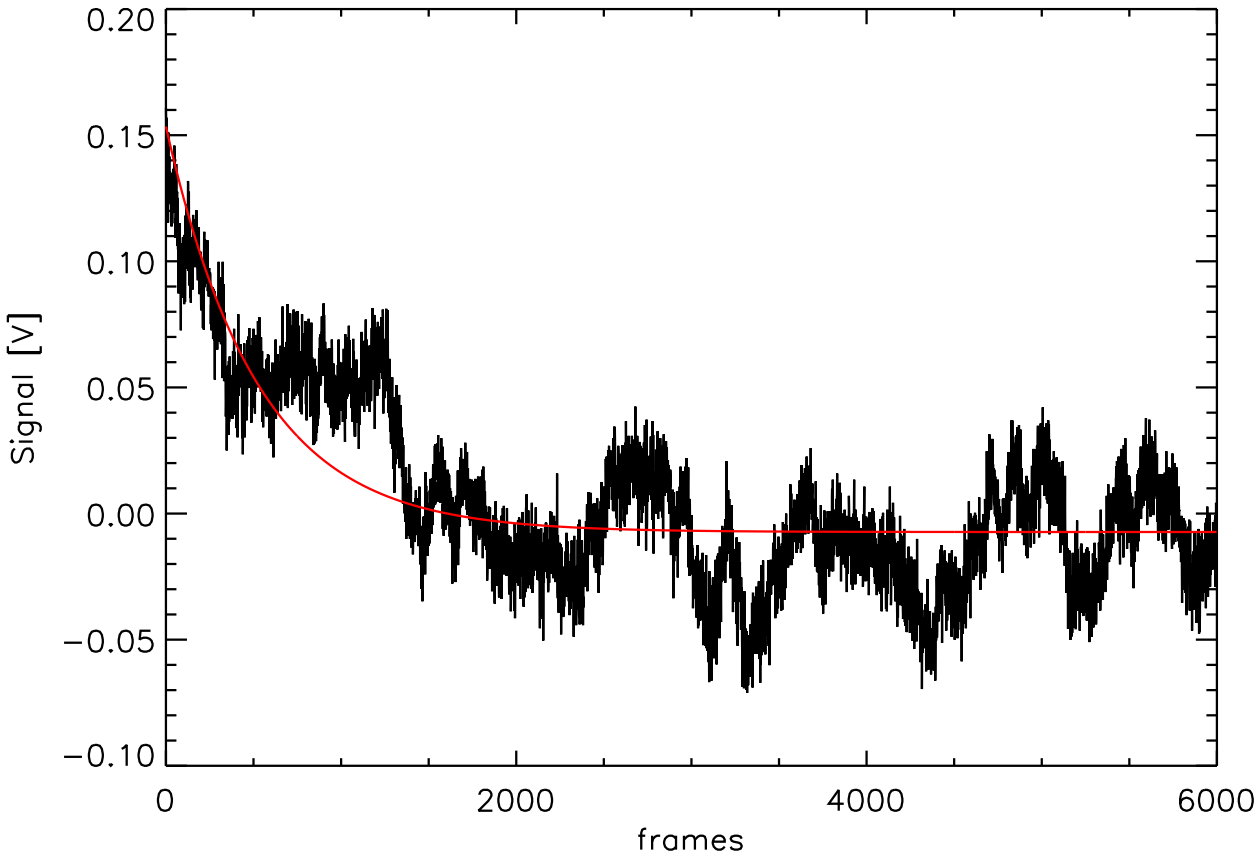

Figure 5.7: The signal trace for a sub-scan for a single bolometer in black, the exponential decay fit in grey.

bolometer signal goes through an AC filter, which translates the change in DC level into a spike with an exponential decay of the same time constant as the AC filter, 10 seconds. This exponential decay is present at the beginning of every sub-scan, and is not correlated between bolometers. It must be removed from each bolometer channel individually before sky subtraction can be attempted, so as to not contaminate the sky estimate. With a known time constant, we do a linear fit based only on the amplitude of the exponential and remove this from each sub-scan. Figure 5.7 shows data from a sub-scan that was preceded by a dewar rotation for a single bolometer, and the fitted exponential decay.

5.5 Bolometer Average Sky Subtraction

5.5.1 Full Array Average

The beams for Bolocam's bolometers overlap on the primary, and do not significantly separate until about 15km above the telescope. Most of the water vapor in the atmosphere is below this altitude, implying that each bolometer should see the same sky noise from the same column of atmosphere. If the sky noise is perfectly correlated between bolometers, and the astronomical signal is small compared to the noise in a single sub-scan, we can take the average of all the bolometer traces for a sub-scan to create a sky noise template. The template can then be subtracted from each bolometer leaving only astronomical signal and uncorrelated noise. Figure 5.8 shows a raw bolometer trace, the calculated sky template, and the cleaned bolometer trace. The cleaned trace has been shifted down by 0.15V to show the data clearly. The average subtraction removes 2 orders of magnitude of the 1/f noise. We can compare these results to the PSD of the dark bolometers. Dark bolometers do not see the sky, but are subject to all the same noise sources internal to the dewar and the electronics. Figure 5.9 shows that at low frequencies the average subtracted noise is still significantly higher than the dark bolometer noise. Obviously there is some non-perfectly correlated noise due to the sky that we have not subtracted with this method.

5.5.2 Locally Weighted Average

One possible explanation for the existence of non-perfectly correlated sky noise concerns the overlap of the beams on the primary. If the beams are not perfectly overlapped, they will separate at a lower altitude. Those bolometers on one side of the array would see a slightly different column of atmosphere than those on the other side. The bolometers closest to each other would have more highly correlated noise than those further apart. To account for this we created a slightly different sky template for each bolometer. The average for each bolometer was weighted by the

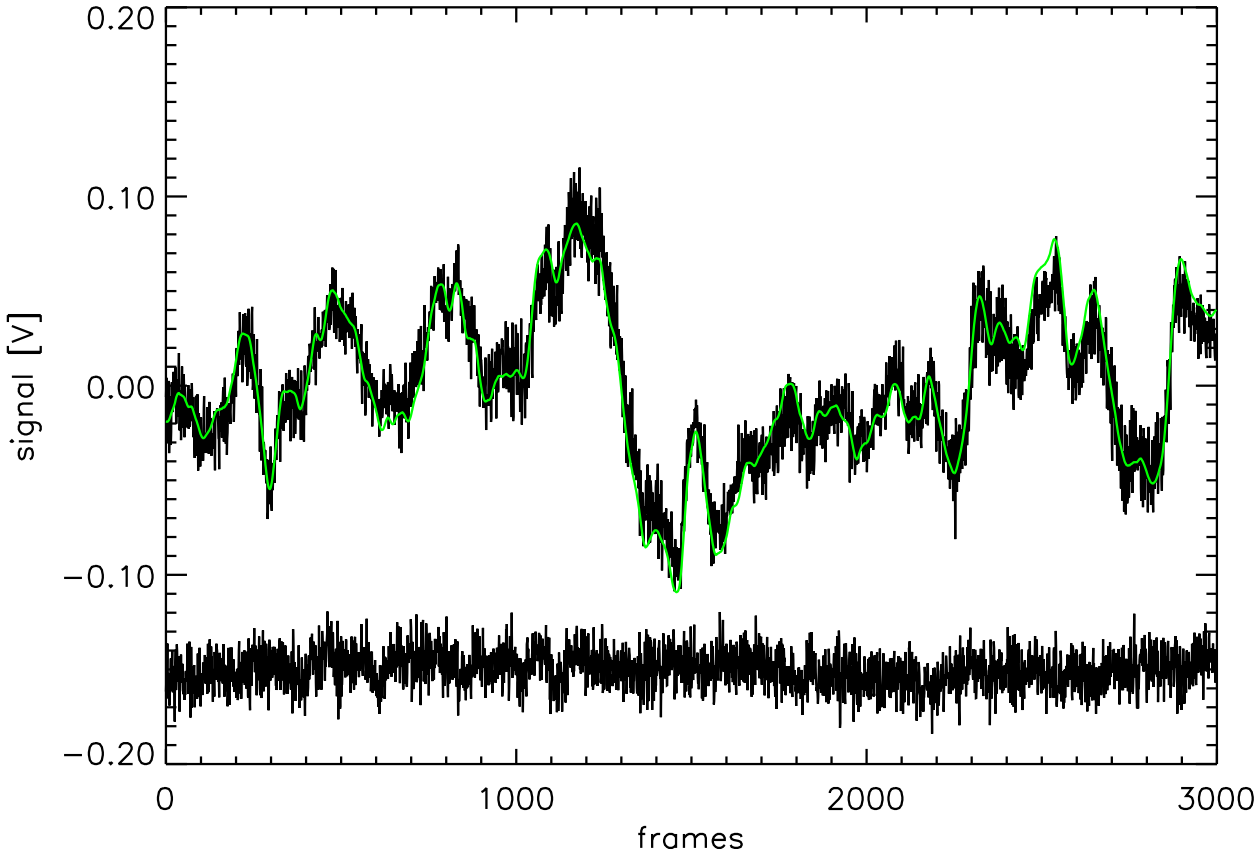

Figure 5.8: A bolometer trace for a single sub-scan in black, the sky template calculated from a full array average in grey, and the resulting cleaned trace shown below, shifted down to make it clear.

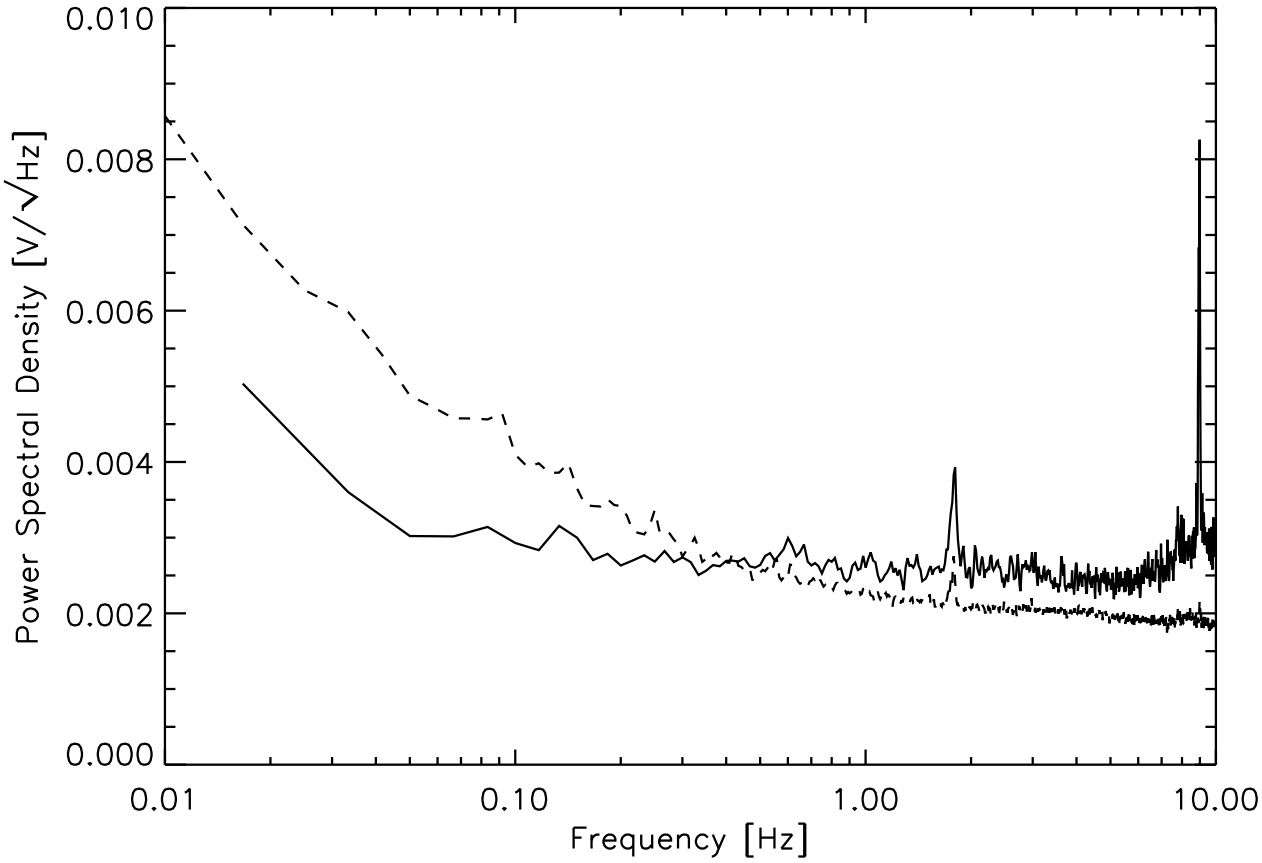

Figure 5.9: PSD of dark bolometers is the solid line, the PSD of the full array average subtracted data is the dashed line. At low frequencies residual uncorrelated sky noise contributes to noise in the average subtracted data. At high frequencies the lower temperature of the dark bolometers contributes more Johnson noise.

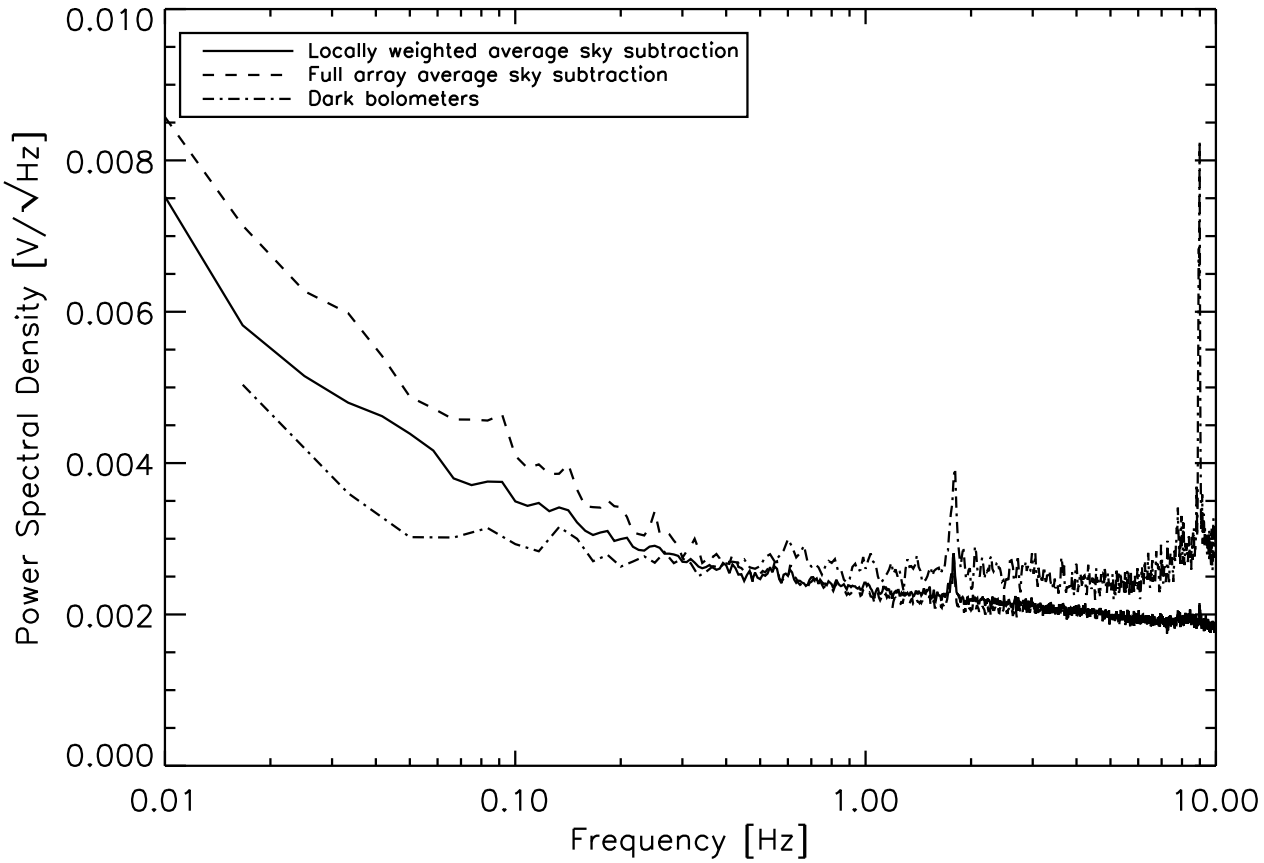

Figure 5.10: The locally weighted average subtraction improves the noise at low frequencies, but does not reach the level of the dark bolometers.

distance from the other bolometers. The weighting was a Gaussian with a standard deviation of 2 arc minutes of distance across the array. The standard deviation was determined empirically by measuring the residual 1/f noise for various values, and choosing the largest σ that still removed all the possible 1/f noise. The results of the locally weighted average subtraction are shown in Figure 5.10, compared to the full array average subtracted data, and the dark bolometer data. We have subtracted a significant amount of the 1/f noise, at the expense of subtracting some of the large scale structure in the data. The noise at low frequency is still not as low as the dark bolometers which means there is still residual sky noise that we may be able to

subtract from the data.

5.6 PCA Sky Subtraction

In order to further improve the sky subtraction we turned to a technique used in image compression, Principle Component Analysis, or more specifically the Karhunen and Loeve (KL) transform. In a KL transform a set of vectors (in our case the time ordered data for each bolometer) is transformed into an orthogonal basis determined by the eigenvectors of the auto-correlation matrix. If D_{MxN}, where M is the number of bolometers, and N is the number of data points, is the two dimensional data array, where d_i are the columns of this array and correspond to the time ordered data for each bolometer, then the KL transform is calculated as follows. First the correlation matrix is calculated,

$$C = DD^T. \tag{5.2}$$

The eigenvalues of this matrix are calculated as usual

$$|C - \lambda_i I| = 0 \tag{5.3}$$

where λ_i is an eigenvalue of the correlation matrix and I is the identity matrix. In the case of Bolocam, the number of eigenvalues should correspond to the number of bolometers. The corresponding eigenvectors are calculated and put in descending order based on the eigenvalues.

$$R = [\phi_1 \phi_2 \cdots \phi_N] \tag{5.4}$$

where ϕ_i is a eigenvector corresponding to eigenvalue λ_i. We can then transform the original matrix.

$$\Phi = R^T D \tag{5.5}$$

where the columns of Φ are now the new orthogonal basis vectors. The basis vector with the highest eigenvalue is the most highly correlated component of the data. In

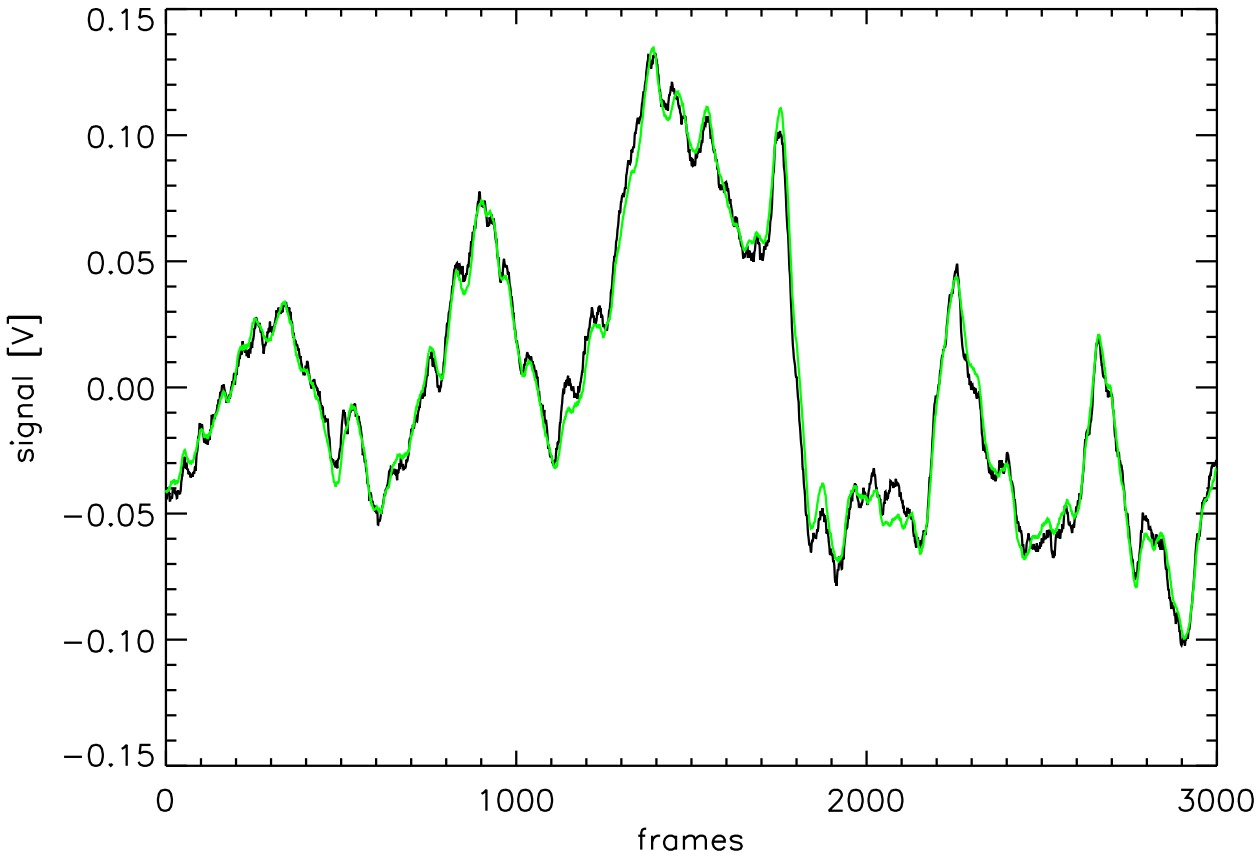

Figure 5.11: The sky template calculated using the full average array sky subtraction is shown in black, the first basis vector calculated in the PCA sky subtraction is shown in grey. The time traces are almost identical.

data compression applications the vectors with the smallest eigenvalues are removed from the data, but we wish to do the opposite. In order to remove correlated sky noise we must remove the basis vectors with the largest eigenvalues. The basis vector with the largest eigenvalue is almost identical to the sky template calculated using the full array average discussed in section 5.5, as shown in Figure 5.11. The advantage of the PCA sky subtraction technique is that we can subtract more than just this most correlated vector. The method we used to determine how many eigenvectors to remove from the data was to remove vectors until the given eigenvalue was less than the sum of all remaining eigenvalues. For the December 2001 2.1 mm data

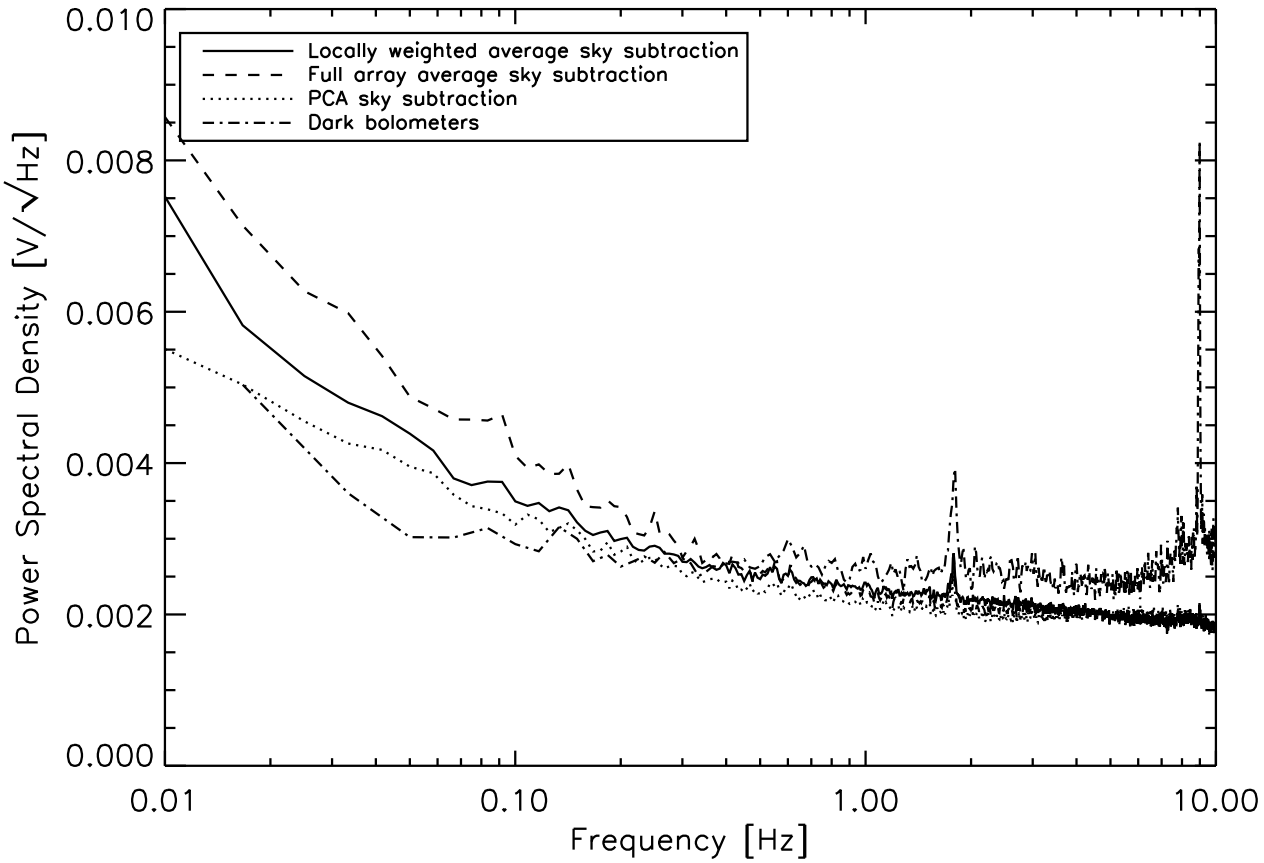

Figure 5.12: PSD for each of the sky subtraction techniques compared to the dark bolometers. The PCA technique is close to the best we can expect for sky subtraction.

this generally resulted in subtracting three eigenvectors. The results of the PCA subtraction technique compared to the full array average and locally weighted average techniques is shown in Figure 5.12. The Figure shows that the PCA technique brings us approximately to the limit of the dark bolometer data, but we can see that there is 1/f noise present in the dark bolometer data.

We can speculate on the possible causes of this low frequency noise. The bolometers do not see sky photons so the sky noise contribution must be zero. The source of noise considered most seriously was microphonics due to the telescope motion during an observation. As described in chapter 3, microphonic noise is caused by motions of

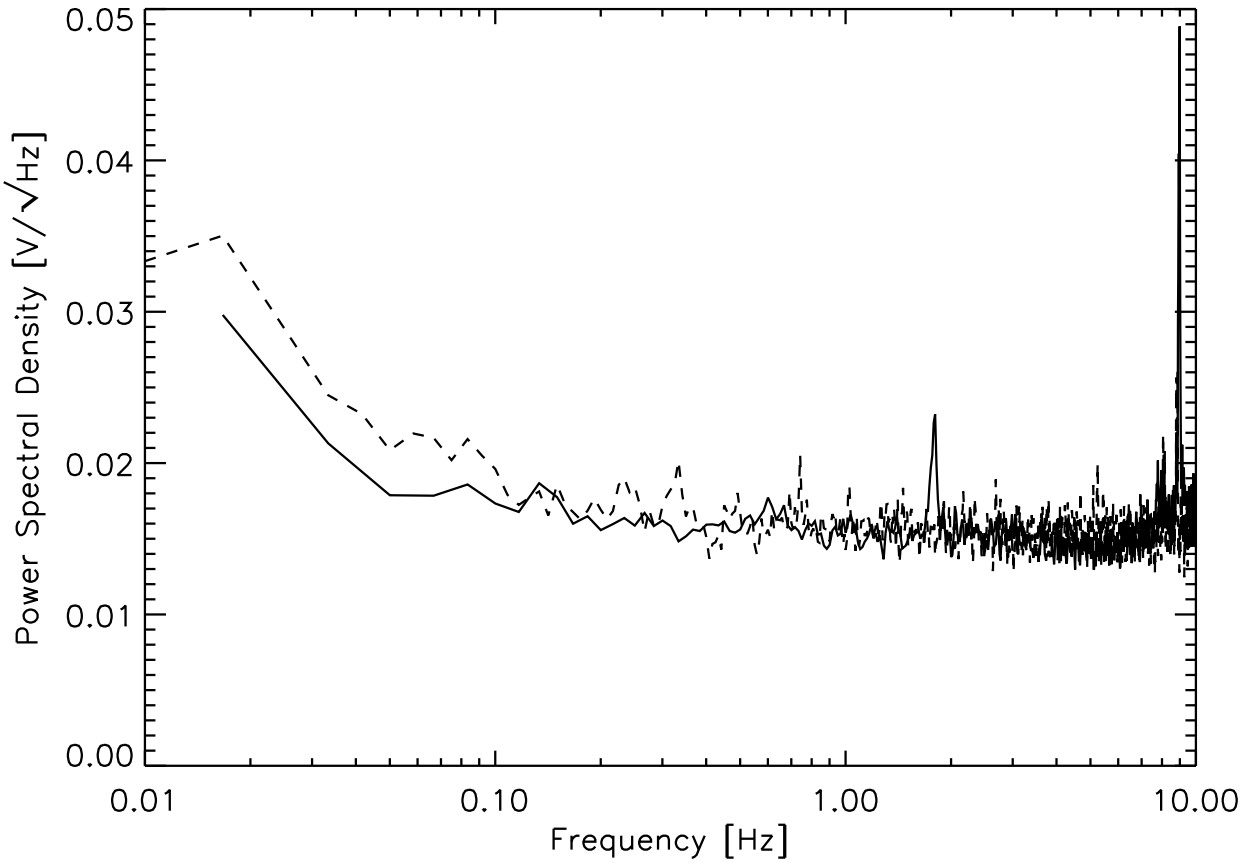

Figure 5.13: The power spectral density of dark bolometers. The solid line is during a capped raster scan observation, the dashed line is capped data with a stationary telescope.

the wires carrying signal in the dewar. If these wires are not well tied down inside the dewar motion of the telescope and dewar will contribute noise to the signal. To test this hypothesis we took data with the dewar window blanked off both with the telescope following a standard rastering observation, and with the telescope stationary. The results are shown in Figure 5.13. The noise in the dark bolometers while the telescope is stationary is compareable to the noise during the rastering observation. This eliminates telescope motion as a significant contributor to the 1/f noise of the bolometers. These results also show that we can use both rastering and drift scsan observation techniques without significant degredation in the noise.

Another possible cause for the 1/f noise in the dark bolometers is temperature drifts in the ultra-cold stage of the fridge. If the array changed temperature uniformly any signal produced in the bolometers could be removed because it would be correlated across the array and removed in the sky subtraction. If the silicon wafer is not well heat sunk and there are temperature gradiants across the array then 1/f noise may appear in the dark bolometer data. This possibility has not been pursued thus far due to the difficulty in mounting the wafer without cracking the array, and the fact that this residual noise is quite small.

5.6.1 Physical Origins of PCA Eigenvectors

The PCA technique is a mathematical transform of our data to remove correlated noise. The technique is powerful, but we would like to understand the physical causes for the particular correlations that the PCA method removes. If we can understand the physical cause, then we can attempt to remove it for future data runs. In pursuit of this goal we measured the correlation of each basis vector we subtracted with each of the bolometer traces, and looked for patterns across the array. The first vector was of course highly correlated with all the bolometer traces. The second and third vectors were more interesting. Figure 5.14 shows the correlation of the bolometer traces with the second basis vector as a function of the bolometer number, after the removal of the first basis vector, and an exponential decay from the data. The dotted line is a cosine function provided to guide your eye. Figure 5.15 shows the correlation of the second basis vector with the bolometer traces as a function of the angle of the bolometer on the array. The dotted line is again a cosine function provided to guide your eye. We can see that the correlation with angle is much better. The second and third eigenvectors remove a signal from the data which is dependent on the angle of the bolometer on the array. If the signal was due to an effect of the PCA calculations, the signal would be dependent upon the ordering of the bolometer traces in the D matrix. Any effect within the Bolocam electronics chain would depend on the bolometer number, which is the ordering of the bolometers in the electronics chain.

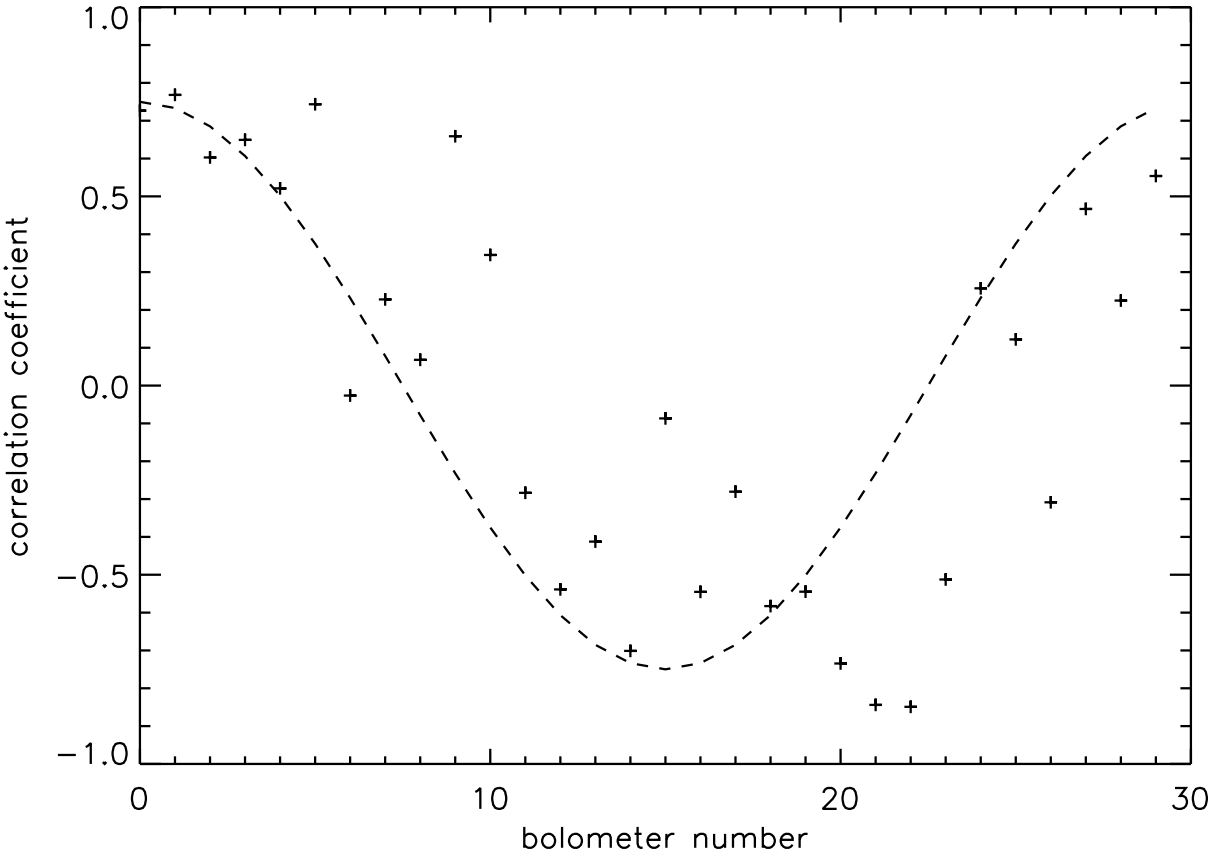

Figure 5.14: Correlation coefficients of each of the bolometer traces with the second basis vector calculated during PCA sky subtraction are shown plotted vs the bolometer number. The dotted line is a cosine function provided to guide your eye.

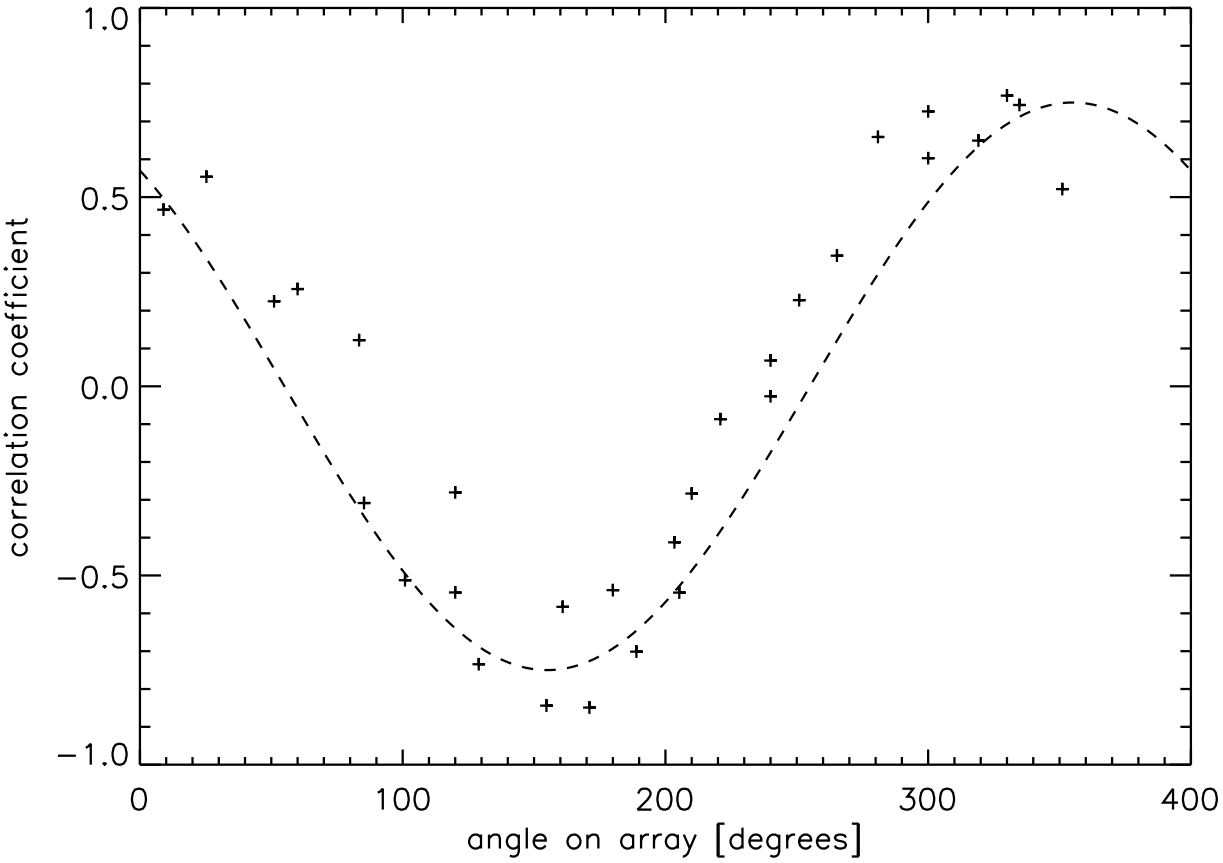

Figure 5.15: Correlation coefficients of each of the bolometer traces with the second basis vector calculated during PCA sky subtraction are shown plotted vs the angle of the bolometer on the array. The dotted line is a cosine function provided to guide your eye.

To determine if the phase of the correlation is constant with respect to either the array or the telescope, the same analysis was repeated on several different observations at varying dewar angles. The phase of the correlation remained constant with varying dewar angles implying that the source of the signal is within the dewar.

Further study into the physical origin of the PCA second and third eigenvectors is being conducted using the Bolocam data from subsequent observing runs. More careful tests with this problem in mind should solve this mystery in the near future. Unless otherwise indicated all data analysis on the 2.1 mm data presented in the next chapter used the PCA sky subtraction technique.

Chapter 6

Data Analysis

After we have removed the atmospheric noise from the data, we make maps of the SDS1 and Lynx data. This chapter will detail the process that takes the time ordered data to a map in right ascension and declination coordinates, the analysis of those maps for the presence of structure, and the filtering of the maps for cluster source extraction. The final section will present the upper limit Bolocam places on the CMB power spectrum at high ℓ.

6.1 Mapping the Data

To map the blank sky data we first create a grid of pixels in the right ascension and declination coordinates for both the Lynx and SDS1 data. Each pixel is 20 arc seconds square, which gives us 9 pixels within the beam full width half max. Each frame of the time ordered data contains the RA and dec coordinates of the bore sight of the telescope. In order to map the data for each bolometer to the correct pixel we need to know the offset of each bolometer from the telescope bore sight. These offsets are measured using the Mars observations.

6.1.1 Bolometer Bore Sight Offsets

For each observation of Mars we made separate maps for each of the bolometers with no compensation for the offset from the telescope bore sight. Each frame is mapped according to the bore sight coordinates. We fit a two-dimensional Gaussian to the

resulting map to determine the centroid of the Mars signal. This centroid will not be at the actual position of Mars. Since we know that Mars is not in a different position, we can calculate the offset required to put Mars in the proper position. This offset is calculated for each bolometer, averaged over the six Mars observations, taking the rotator angle of the dewar into account. Using the offsets we calculate the RA and dec of each bolometer for each data frame.

6.1.2 Map Calculation

Each pixel in the map encompasses a range of 20 arc seconds in RA and 20 arc seconds in declination. Using the RA and dec for each frame and each bolometer we determine which data are included in each pixel. To determine the value of the pixel we perform a weighted average of the data within each pixel, given by equation 6.1.

$$m_p = \frac{\sum_{i=0}^{N} d_i/\sigma_i^2}{\sum_{i=0}^{N} 1/\sigma_i^2} \tag{6.1}$$

where the sum is over the data samples assigned to pixel p, d_i is a time ordered data sample, and σ_i is the noise for that data sample. The noise for each sample, σ_i, is calculated from the PSD of the data. The PSD for each bolometer and each sub-scan is calculated after the sky subtraction is performed. These PSD's are multiplied by the Gaussian beam in Fourier space, and the result is integrated to give a measure of the variance for that data. Each data sample in the given sub-scan for that bolometer is assigned the same noise estimate.

6.1.3 Map Noise

The overall noise of the map is calculated in two ways. The first and easiest is the root mean square (RMS) of the pixel values. This gives an estimate of the noise of the map if we assume there is no signal. Any signal in the map would increase the RMS, a fact we take advantage of in the jack-knife tests described in the next section. The second method for measuring the noise of the map is more accurate. We fit a

Field	RMS$_{ave}$ $[mK_{CMB}]$	RMS$_{diff}$ $[mK_{CMB}]$	$\sqrt{RMS^2_{ave} - RMS^2_{diff}}$
Lynx	0.744	0.722	0.180
SDS1	2.45	2.40	0.492

Table 6.1: RMS comparison of jack-knifed data

Gaussian to the histogram of the pixel values, and take the standard deviation to be the noise of the map. This method reduces contamination from outlying pixels and any signal in the map.

6.2 Jack-Knife Tests

The first question we ask of the data is whether any of the structure is real. The easiest way to do this is to split the data into two halves, map the data, and compare the RMS of the average and difference of the two maps. The difference map must be multiplied by 0.5 so that the weighting is the same as the average. If there is real structure then the RMS of the difference should be lower than that of the average. If the maps are entirely noise, then the RMS of the two maps should be identical. We followed this procedure for the two blank fields observed by Bolocam, Lynx and SDS1. The data were divided in half by taking the data from every other observation. This is because the weather steadily worsened over the course of the observing run, and the first half of the run would have a lower RMS for this reason, unrelated to the structure in the map. The data for each half of the observation were cleaned of sky noise using PCA sky subtraction, described in chapter 5, before they were mapped. The resulting maps are shown in in figures 6.1 and 6.2. The RMS of the average and difference maps for each blank field are shown in table 6.1.

The RMS for the average and difference maps for both blank regions of the sky were similar. This implies that the data is primarily noise.

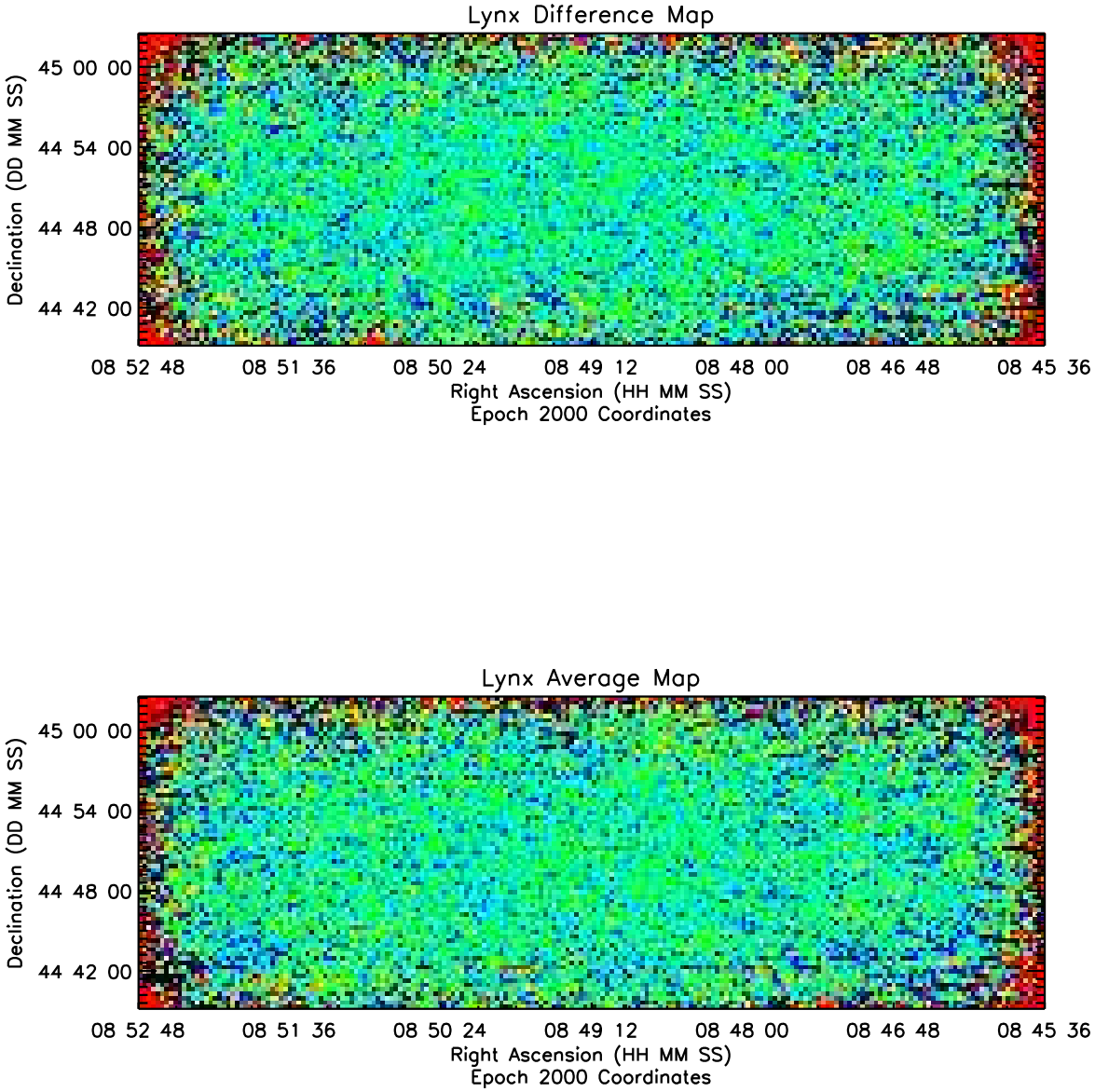

Figure 6.1: The average and difference maps of the two halves of the Lynx blank sky observations.

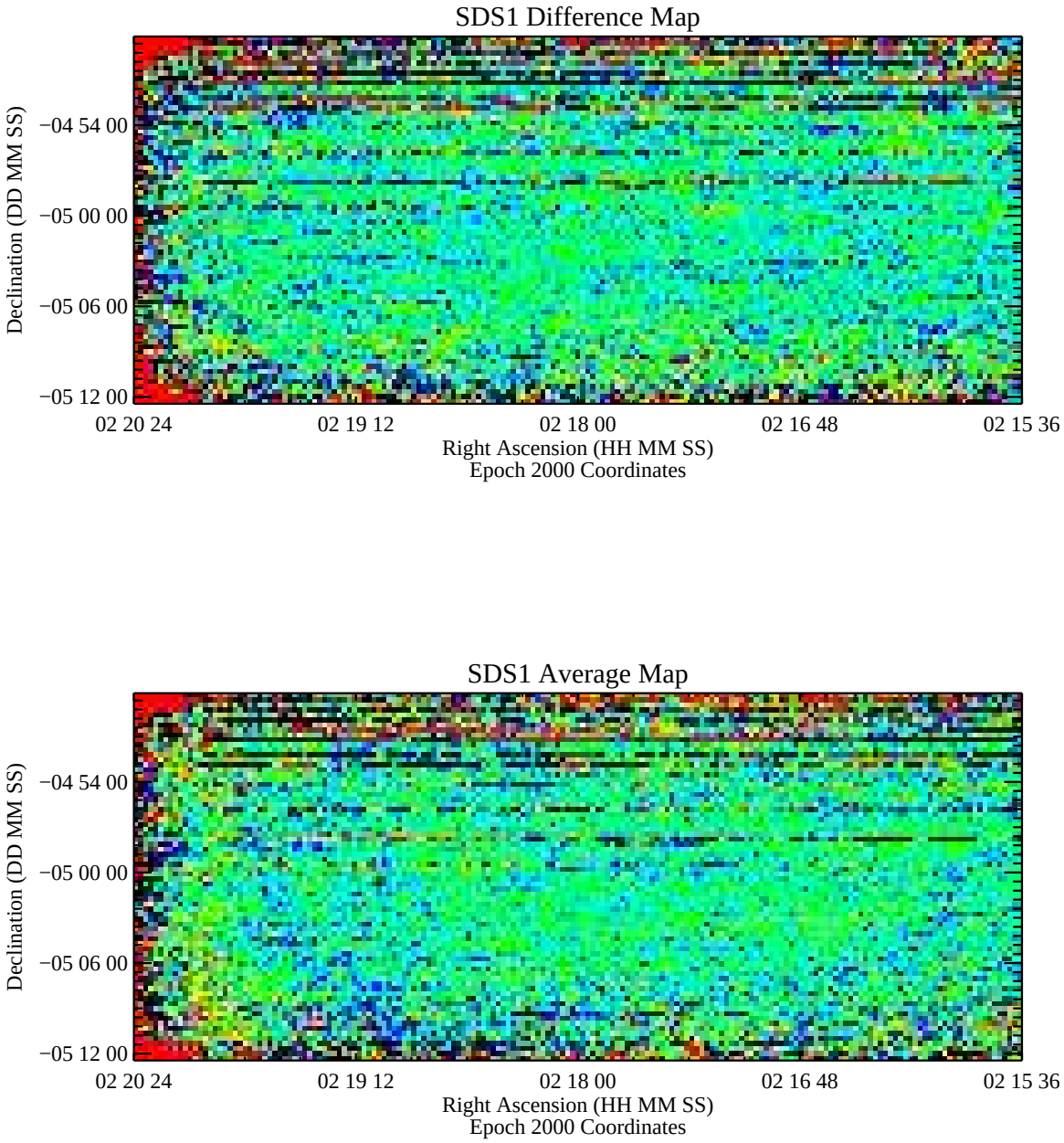

Figure 6.2: The average and difference maps of the two halves of the SDS1 blank sky observations.

6.3 Source Extraction

We can improve the signal-to-noise ratio for compact sources by taking advantage of our knowledge of the spatial structure of the expected sources. This technique is known as spatial filtering.

6.3.1 Optimal Filter

The filter employed on the Bolocam data is an optimal or matched filter. Herranz et al. (2002a) provides an overview of this filter as compared to scale-adaptive filters. If we consider a generic symmetric filter $\psi(\vec{x}; R, \vec{b})$ where R defines the scale of the filter, and $\vec{b}$ the translation from the origin:

$$\psi(\vec{x}; R, b) = \frac{1}{R^n}\psi\left(\frac{\vec{x} - \vec{b}}{R}\right) \tag{6.2}$$

we can define the filtered time stream as the convolution of the original map, $m(\vec{x})$ with the the filter

$$w(R, \vec{b}) = \int d\vec{x} m(\vec{x})\psi(\vec{x}; R, \vec{b}). \tag{6.3}$$

In order for $\psi(\vec{x}; R, \vec{b})$ to be an optimal filter for the detection of a source $s(\vec{x})$ at the origin characterized by a scale R_0, it must satisfy two conditions:

1. $< w(R_0, 0) >= s(0) \equiv A$, the amplitude of the source, or the filtered time stream is an unbiased estimator of the amplitude of the source

2. The variance of $w(R, \vec{b})$ has a minimum at the scale of the source, R_0

A filter with these conditions generates the largest gain in signal to noise ratio (SNR) when convolved with the original map. If we apply these constraints to the generic filter we defined in equation 6.2, and assume that we know the profile of the source we expect to find, we can show that the optimal filter in Fourier space is given by

$$\psi(q) = \frac{1}{a}\frac{\tau(q)}{P(q)} \tag{6.4}$$

where $\tau(q) = s(q)/A$ is the profile of the source in Fourier space, $P(q)$ is the noise spectrum, and a is the normalization required to make the filter unbiased. Equation 6.4 assumes that the source profile is spherically symmetric. For a source with amplitude of 1 at the origin we know

$$\int dq\tau(q)\psi(q) = 1, \tag{6.5}$$

which yields a value for the normalization constant a for a given source profile and noise power spectrum:

$$a = \int dq \frac{\tau^2(q)}{P(q)}. \tag{6.6}$$

6.3.2 Source Profile

The most common profile used to describe galaxy cluster is the β-model. This model provides a simple cluster profile that has been seen to fit the available SZ data well (Mohr et al. 1999).

$$\tau_{cluster}(x) = \frac{1}{[1 + (x/r_c)^2]^{3\beta/2-1/2}}. \tag{6.7}$$

where r_c is the core radius of the cluster, and β is usually taken to be 2/3. Unfortunately this model has a diverging Fourier transform. (Hobson and McLachlan 2003) describe a modified β-model that avoids this problem.

$$\tau_{cluster}(x) = \frac{r_c r_v}{r_v - r_c}\left(\frac{1}{\sqrt{r_c^2 + x^2}} - \frac{1}{\sqrt{r_v^2 + x^2}}\right), \tag{6.8}$$

where r_c is the core radius as before, and r_v is a so called virial radius. This virial radius is not the actual virial radius of the cluster, but is used to truncate the cluster model at large radii. The authors use $r_v = 3r_c$, and we follow their convention. The cluster profile must be convolved with the Bolocam beam, which is well described by

a Gaussian.

$$\begin{aligned} \tau(q) &= \tau_{cluster}(q)b(q) \\ &= \left(\frac{r_c r_v}{r_v - r_c}\frac{e^{-r_c q} - e^{-r_v q}}{q}\right)\left(\theta^2 e^{-(q\theta)^2/2}\right) \end{aligned} \tag{6.9}$$

6.3.3 Noise Power Spectrum Estimation

The noise power spectrum for Bolocam consists of white photon noise plus residual sky noise with a 1/f spectrum. As described in section 4.2, Bolocam observes the sky by scanning back and forth across the target area. The data for each single pass is called a sub-scan, several sub-scans that cover the entire target area is called a scan, and several scans make up a fully sampled observation. The subsection of the data dealt with in the cleaning and time ordered data analysis is a sub-scan. Each sub-scan is separated from the others by data during which the telescope was turning around, and the dewar may have been rotating. The noise during this time is greatly increased, and we generally ignore these data. The data in each sub-scan is completely dominated by noise, therefore, we can estimate the noise power spectrum by finding the power spectrum of the time stream directly. In order to obtain a power spectrum that is an accurate estimate of the noise for the entire map, the power spectra for each bolometer and each sub-scan in all the map observations are averaged in quadrature to generate the noise power spectrum for each map.

6.3.4 Applying the Optimal Filter

In order to apply the optimal filter to the data we must determine an appropriate core radius to use in the beta cluster profile. Benson et al. (2002) discusses the probable cluster detection rate for Bolocam, and note that most of the clusters detected will have a angular size, defined as the half width half max of the beta profile convolved with the beam, of approximately 1'. Consequently we will filter the data using three cluster profiles with half width half max centered around 1'. The core radii selected were 30", 40", and 50", which correspond to a HWHM of 36.4", 60.9", and 71.4",

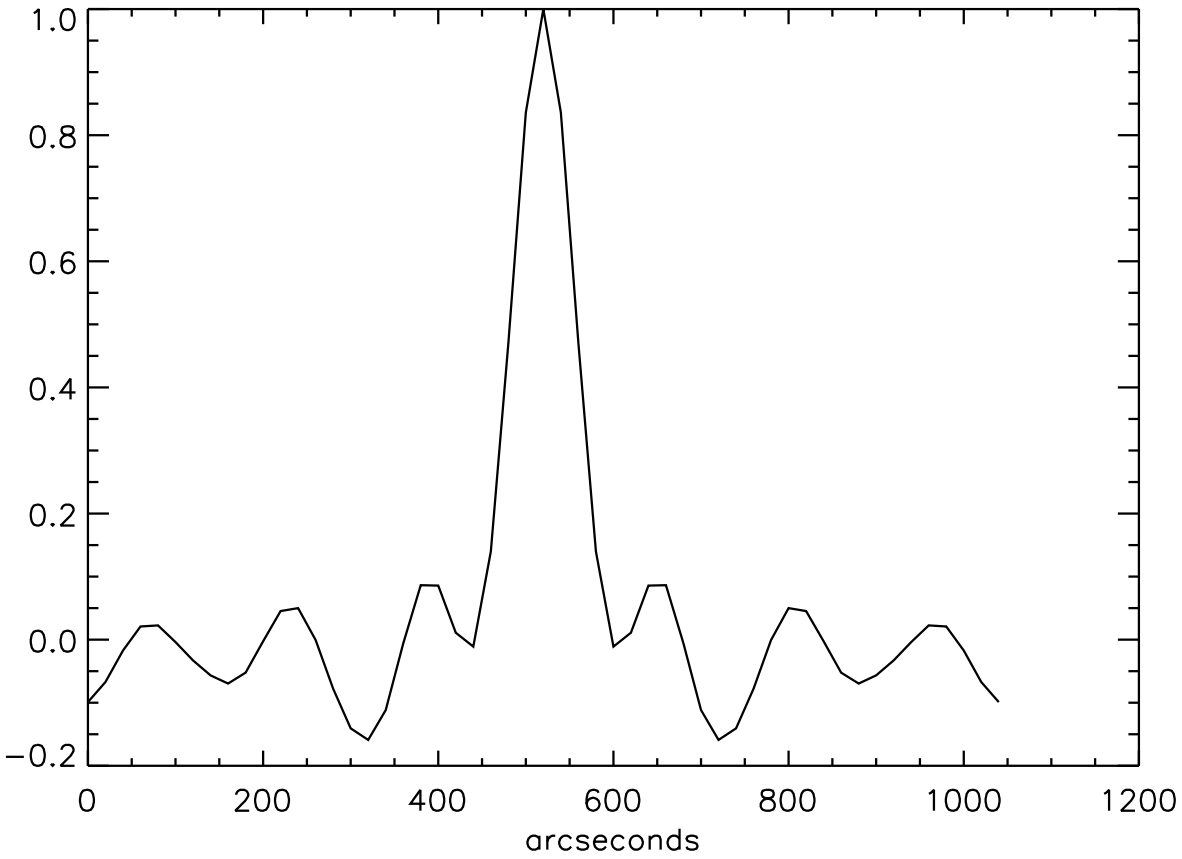

Figure 6.3: A slice through the kernel to be convolved with the Lynx map.

respectively. Figure 6.3 shows a slice through the filter kernel calculated for the Lynx map.

The filter is applied to the map by convolving the two dimensional kernel with the map. The signal to noise ratio for any potential sources is increased by reducing the RMS of the map noise while maintaining the amplitude of any structure with the same profile as the kernel. The reduction of the RMS of the map can be seen most easily by comparing the histogram of the pixel values of the pre-filtered and post-filtered maps.

r_{core}	Lynx (μK_{CMB})	SDS (μK_{CMB})
no filter	230.0	243.8
30”	84.2	165.2
40”	73.1	149.2
50”	64.2	141.1

Table 6.2: The one sigma levels for the Lynx and SDS1 maps.

6.4 Map Analysis

Maps of the two blank sky patches have been produced using data filtered for the various cluster profile widths. The results for the $r_{core} = 40''$ filter are shown in figures 6.4 and 6.5 filtered for cluster beta profiles with core radii of 40”. As a comparison the same maps are also shown without filtering.

To determine the noise of the maps we choose to limit our analysis to the high coverage areas at the center of each map. The histograms of the filtered and unfiltered maps along with the best fit Gaussians are shown in Figures 6.6 and 6.7. The results for each different filter are reported in table 6.2. The noise values for the maps depend on the size of the pixels in the case of the unfiltered maps, and the size of the filter kernel in the case of the filtered maps, which we will take into account in the following analysis.

6.4.1 Source Candidates

In order to search the entire extent of each map for sources we must take the uneven coverage into account. The source threshold must depend on the coverage in that area of the map. The most straighforward way to do this is to define the source threshold in terms of $signal \times \sqrt{time}$. We create new maps for each of the filter kernels where each pixel is multiplied by the square root of the integration time on that pixel. We determine the σ for each of these new maps and set the source threshold to 4 σ. The resulting candidates are reported in tables 6.3 and 6.4. As discussed in Chapter 1, any cluster candidates would appear as decrements in these maps.

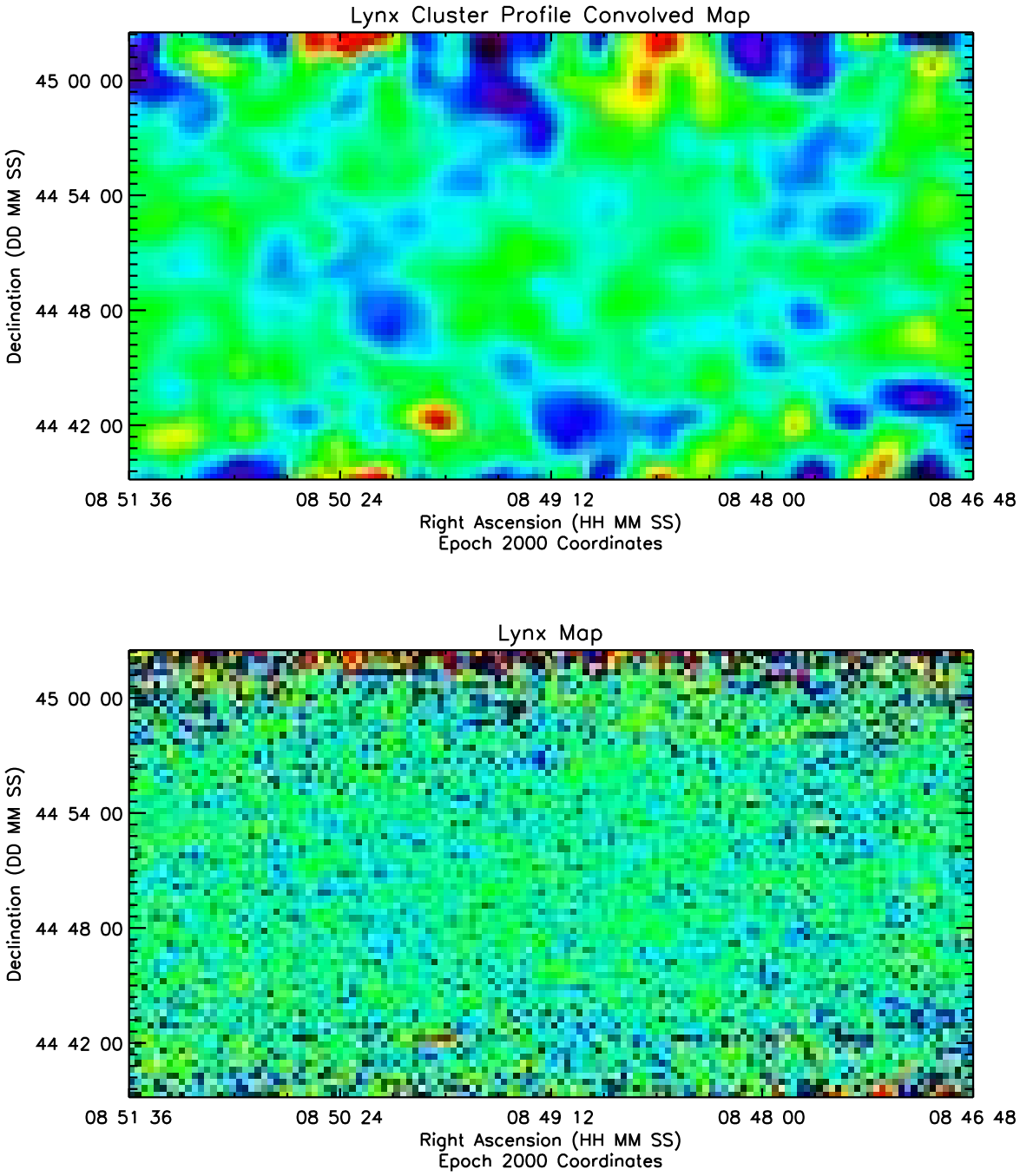

Figure 6.4: The top figure is the Lynx map filtered with the $r_{core} = 40''$ beta-profile filter. The bottom figure is the unfiltered Lynx map.

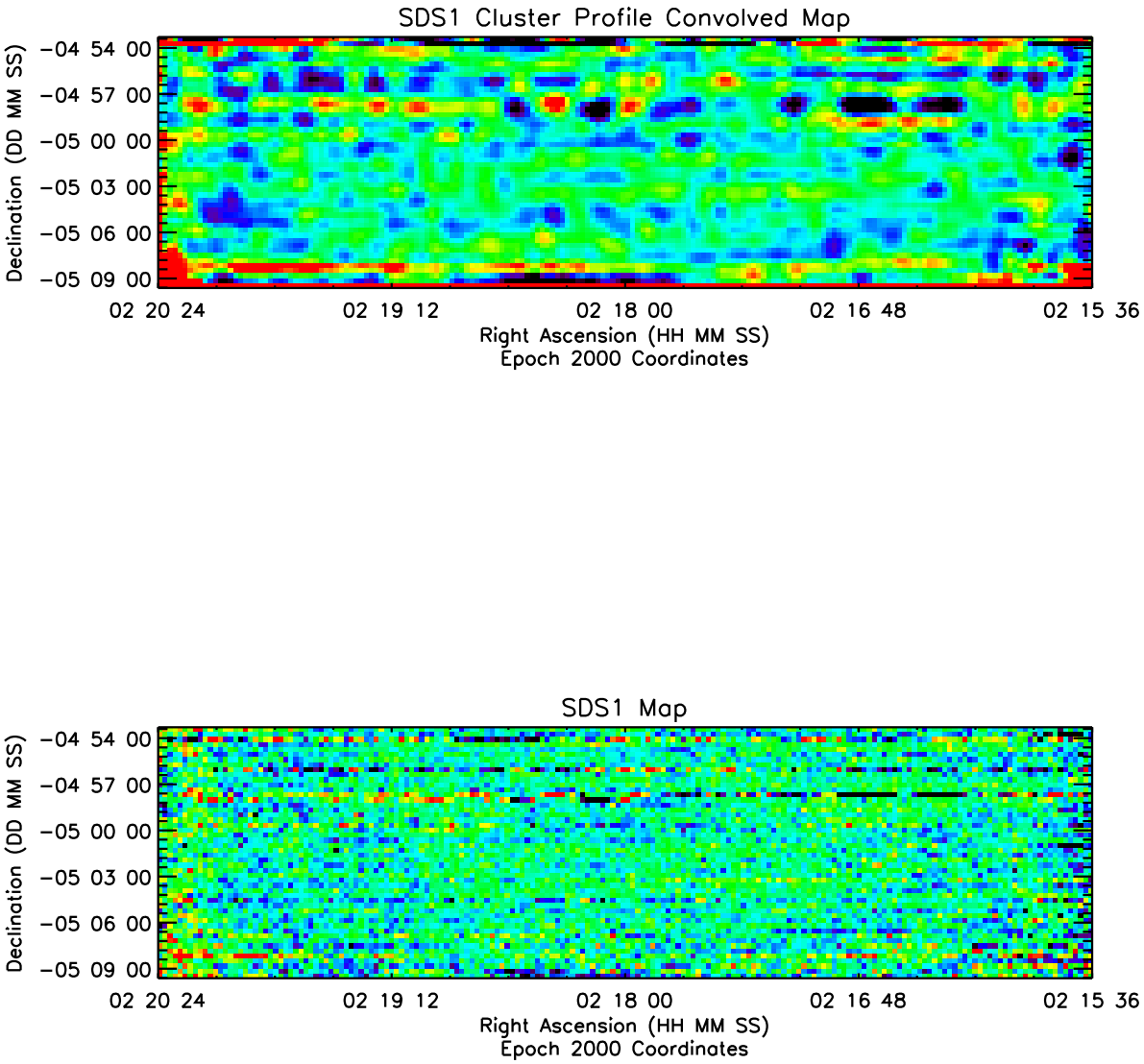

Figure 6.5: The top figure is the SDS1 map filtered with the $r_{core} = 40''$ beta-profile filter. The bottom figure is the unfiltered SDS1 map.

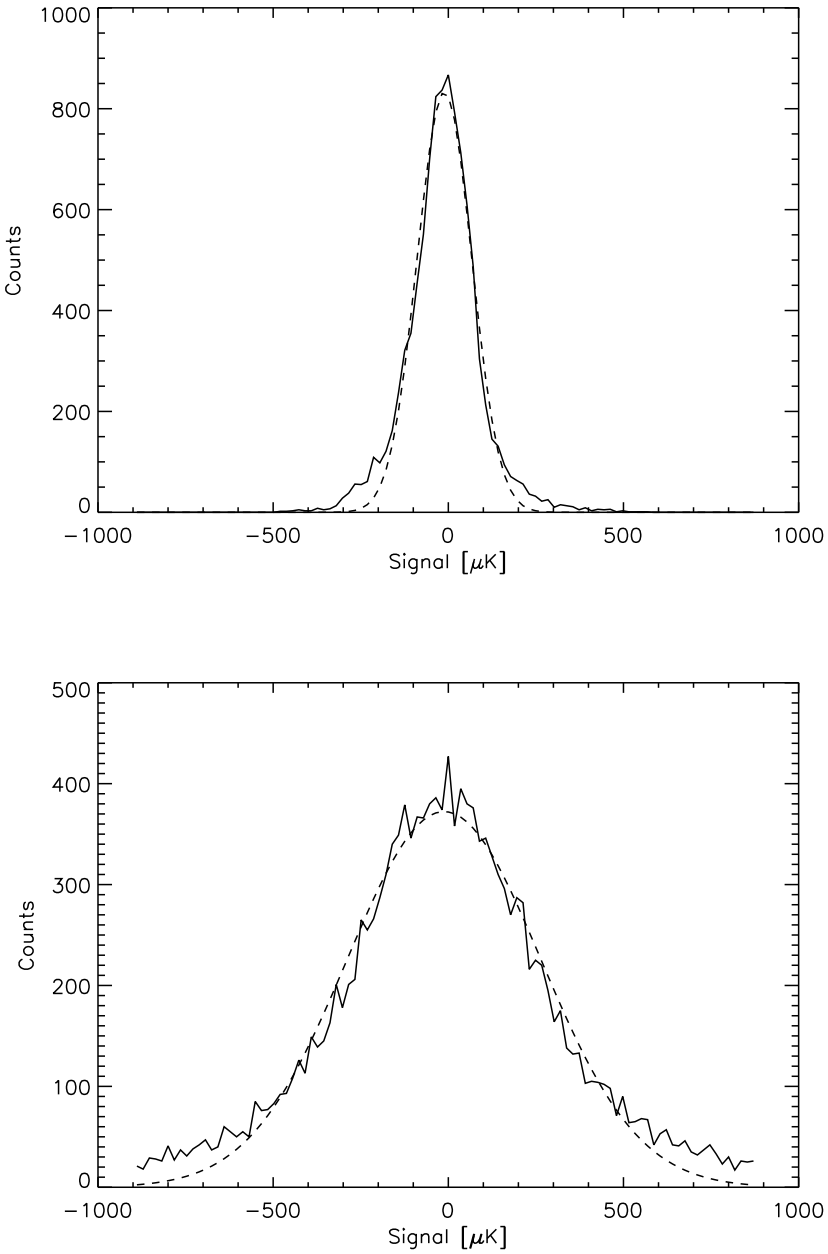

Figure 6.6: The histograms of the Lynx Map. The map convolved with the $r_{core} = 40''$ beta-profile filter is at the top, the unconvolved map is on the bottom. The dashed lines are the best fit Gaussians.

Map	RA (hh:mm:ss)	dec (dd:mm:ss)
SDS1	02:17:52.2	-04:58:17
	02:19:03.1	-04:57:37

Table 6.3: Coordinates of each - 4 σ candidate in any filtered map (J2000).

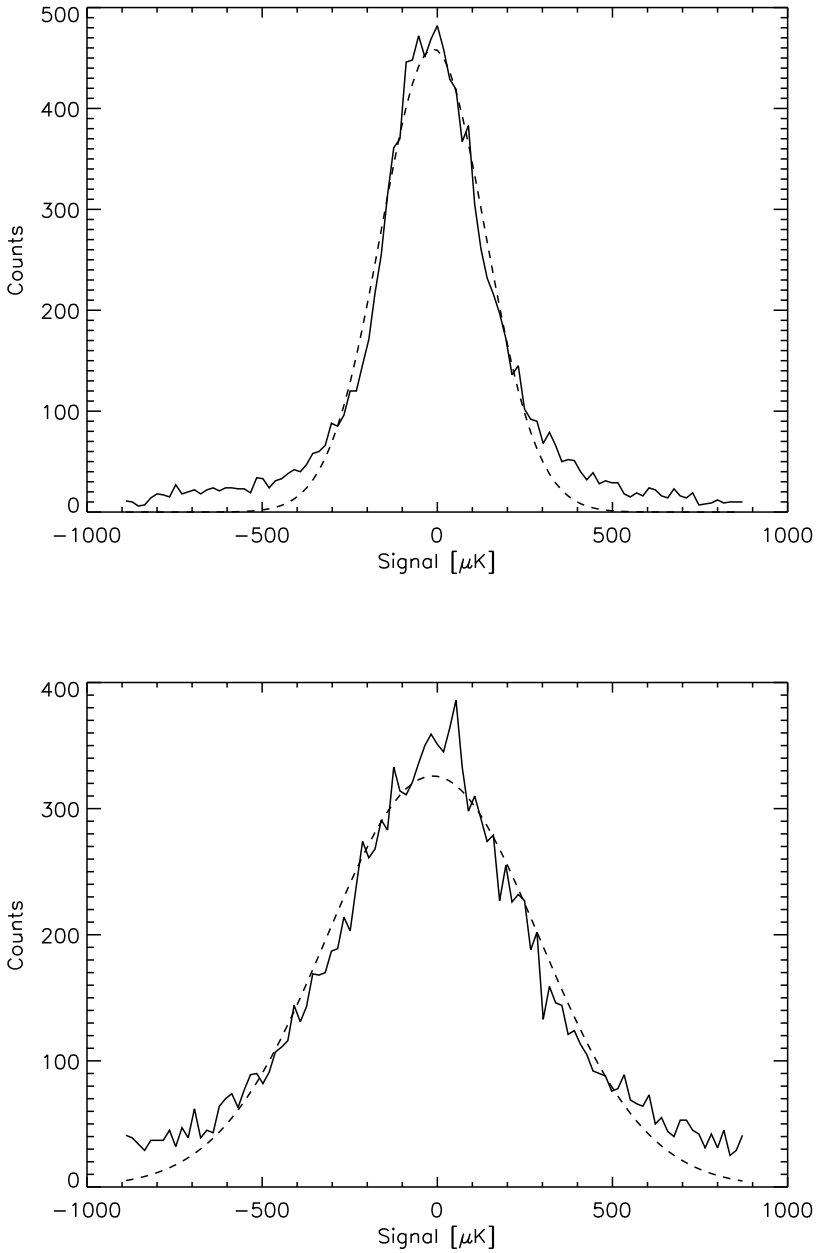

Figure 6.7: The histograms of the SDS1 Map. The map convolved with the $r_{core} = 40''$ beta-profile filter is at the top, the unconvolved map is on the bottom. The dashed lines are the best fit Gaussians.

Map	RA (hh:mm:ss)	dec (dd:mm:ss)
SDS1	02:17:40.1	-04:57:37
Lynx	08:49:44.3	+44:42:10

Table 6.4: Coordinates of each + 4 σ candidate in any filtered map (J2000).

6.4.2 Compare to Cluster Predictions

Many theoretical calculations have been made of the expected number of clusters to be found in SZ cluster surveys. We focus on Benson et al. (2002), which calculates the expected detection rate specifically for Bolocam as compared to the upcoming Planck satellite. The number of clusters are calculated using the Press-Schechter formalism described in chapter 1. The clusters are assumed to have beta-model spherically symmetric profiles, as we assumed in the map filtering. The paper predicts that Bolocam should see one cluster at 10 mJy or above in a one square degree survey. If we assume a five sigma level in order to detect a cluster then the map must have σ = 2 mJy. If we convert the one sigma levels of the Lynx and SDS1 maps to mJy we can determine if we meet this requirement. We use the filtered map with $r_{core} = 40''$. The σ for theses maps, quoted in table 6.2, are 73.1 and 149.2 μK_{CMB}/kernel size. Refering to section 4.4.2, we convert these levels to 12.5 and 25.5 mJy. With these noise levels we do not expect to see any clusters in either of the two maps.

6.5 CMB Angular Power Spectrum Upper Limit

We can also use the data from Bolocam's cluster survey to put an upper limit on the high ℓ CMB angular power spectrum. As discussed in chapter 1 the CMB angular power spectrum is thought to be flat and dominated by unresolved SZ signal at high angular resolution.

The one sigma level of the blank sky maps for Bolocam are equal to the upper limit placed on the power spectrum convolved with the window function. Since the power spectrum is thought to be flat at the high angular resolutions probed by Bolocam we can take it to be a constant. The one sigma level of the map is therefore given by:

$$\sigma = \Delta T_{CMB} \int W(ln(\ell)) d(ln(\ell)) \tag{6.10}$$

where $W(ln(\ell))$ is the window function, σ is the noise level of the map, and ΔT_{CMB} is the power spectrum upper limit. Bolocam's window function depends on the filtering

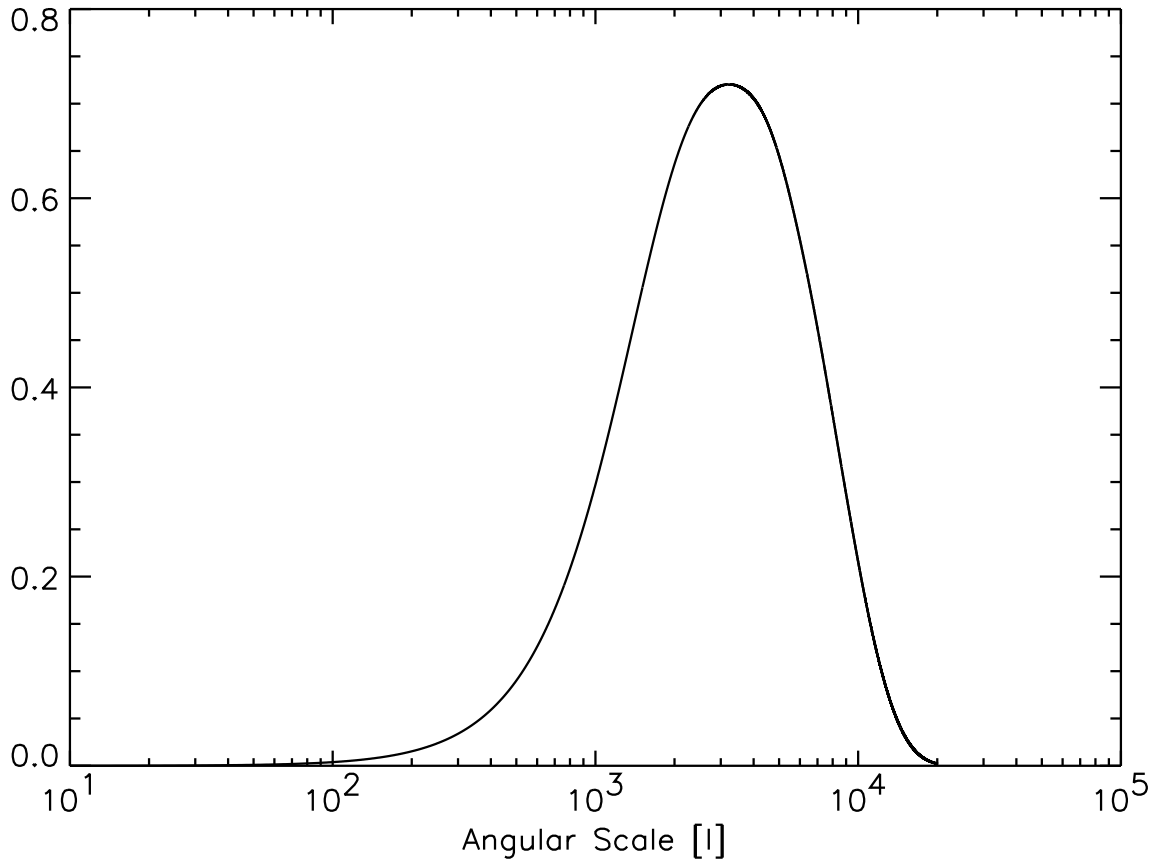

Figure 6.8: The window function for the Bolocam maps assuming a cluster profile filter with $r_{core} = 40''$ and a Gaussian beam with FWHM = 60".

we apply to the map. Figure 6.8 shows the window function for the map filtered with a $r_{core} = 40''$ beta profile filter. The lower edge of the function is due to the beta profile filter, and the upper edge is defined by the Bolocam beam size. We use the σ of our deepest integration area, the center of the Lynx map, 73.1 μK_{CMB}. We can solve for the upper limit the Bolocam blank field maps place on the CMB angular power spectrum:

$$\Delta T_{CMB} = \frac{\sigma}{\int W(ln(\ell))d(ln(\ell))} = \frac{73.1\mu K_{CMB}}{1.49} = 49\mu K_{CMB} \qquad (6.11)$$

The Bolocam upper limit plotted with the recent high ℓ data points from ACBAR,

CBI, and BIMA are shown in Figure 6.5.

6.6 Mapping Speed

The Lynx data consists of 50.6 hours of on source integration time, and 60.3 total hours of observation. The SDS1 data consists of 35.3 hours of on source integration time and 41.7 total hours of observation. This gives an average observing efficiency of 84%, implying that only 16% of the observing time is spent in between sub-scans, turning the telescope and rotating the dewar. Given the final one sigma noise levels for the filtered maps and the number of hours of integration we can determine an overall mapping speed for each blank field. We use the maps filtered with the $r_{core} = 40''$ kernel for our calculations. The $22' \times 11'$ center of the Lynx map has a one sigma noise level of 73.1 μK_{CMB} and 16 hours of integration time giving a mapping speed, neglecting observing efficiency, of $2.6 \times 10^{-3} arcmin^2/\mu K^2_{CMB} hr$. The $27' \times 10'$ center of the SDS1 map has a one sigma noise level of 149.2 μK_{CMB} and 10.7 hours of integration time giving a mapping speed of $1.1 \times 10^{-3} arcmin^2/\mu K^2_{CMB} hr$. For the following calculations we use Lynx mapping speed and account for the observing efficiency to give a mapping speed of $2.2 \times 10^{-3} arcmin^2/\mu K^2_{CMB}/hr$.

Using the predictions by Benson et al. (2002) described in the previous section we can calculate the noise level we need to achieve in the Bolocam cluster survey maps before we expect to detect clusters. If we assume the same noise performance and similar weather conditions as the first observing run at 2.1mm, we can use the mapping speed we calculated to determine the number of observing hours required to cover one square degree to 2 mJy/cluster which is equivelent to a noise level of 11.7 μK_{CMB}. Using the calculated mapping speed of $2.2 \times 10^{-3} arcmin^2/\mu K^2_{CMB} hr$, we see that this requires 1.2×10^4 hours of integration. A more practical goal is to statistically detect the high ℓ CMB power, proposed to be due to unresolved SZE flux.

In recent years several surveys have been conducted that measure the CMB angular power spectrum at small angular scales, ACBAR (Kuo et al. 2002), CBI (Mason

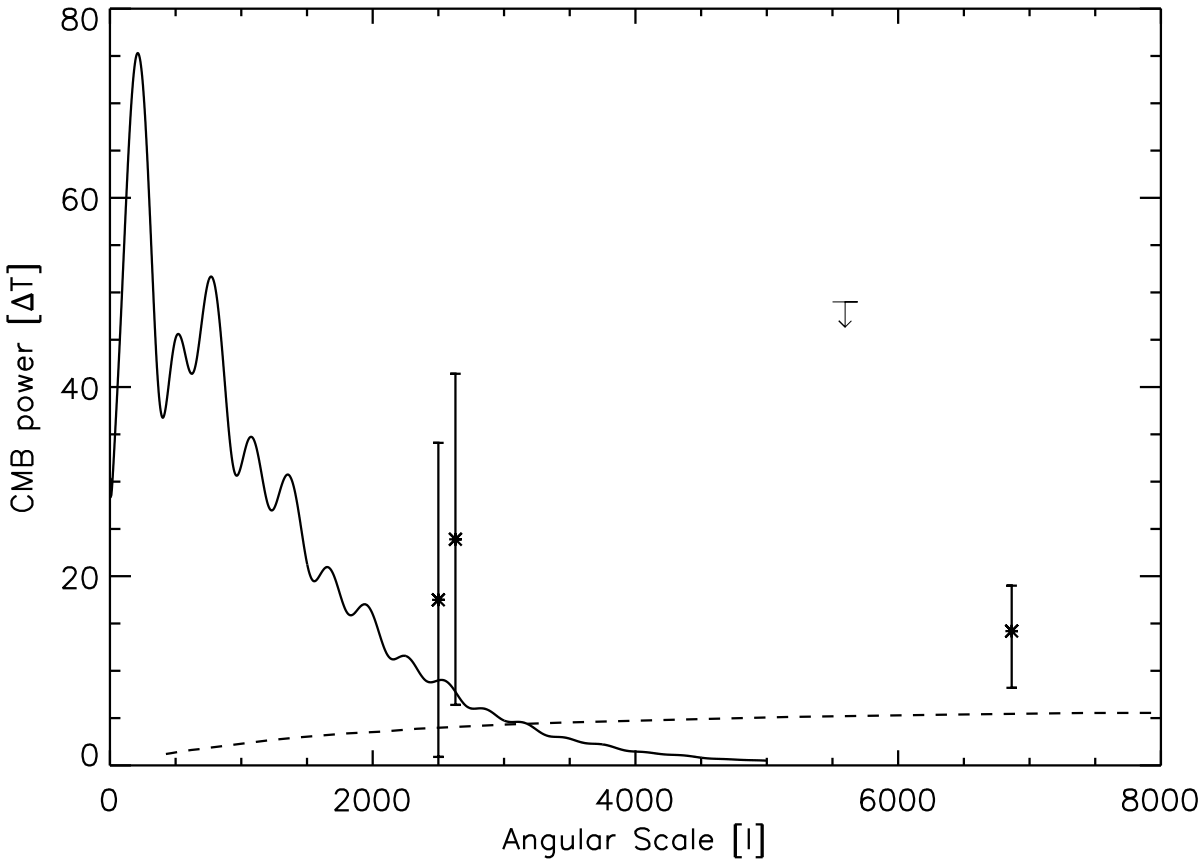

Figure 6.9: A CMB angular power spectrum model is shown as the solid line, using a $\Omega_M = 0.3$, $\Omega_\Lambda = 0.7$ flat Universe model. Predictions for the high ℓ power due to the SZE from Springel et al. (2001) is shown as the dashed line. The data points included are from left to right; ACBAR, CBI, Bolocam, and BIMA.

Experiment	$\Delta T_{CMB}(\mu K_{CMB})$	ℓ_{eff}
ACBAR[1]	17.5 ± 16.6	2500
CBI	23.9 ± 17.5	2630
BIMA	$14.2^{+4.8}_{-6.0}$	6864

Table 6.5: CMB angular power spectrum values for various recent experiments

et al. 2003), and the BIMA survey (Dawson et al. 2002). Each survey's measurement of the CMB angular power spectrum and the corresponding ℓ values are given in table 6.5. Using the mapping speed we calculated for Bolocam we can determine the integration time needed to reach $\Delta T_{CMB} = 14.2 \rightarrow 23.9\ \mu K_{CMB}$. Using equation 6.10 the one sigma level we need to achieve in our blank field map is $1\sigma = 21 \rightarrow 35.6$ μK_{CMB}. Given the mapping speed we calculated the number of hours required to achieve this noise level assuming the same coverage as the center of the Lynx map (242 $arcmin^2$), to be 249 $\rightarrow$ 86 hours.

6.7 Comparison to Expectations

Before Bolocam 2.1 mm system was completed and tested we calculated a predicted sensitivity of 660 $\mu K_{CMB}\sqrt{s}$ and a predicted mapping speed of 0.14 $arcmin^2/\mu K^2_{CMB}/hr$. The final mapping speed of $2.2 \times 10^{-3} arcmin^2/\mu K^2_{CMB}/hr$ is about 2 orders of magnitude lower. There are two places where the factor of 63 between the predicted and achieve mapping speeds was introduced. The first is in the difference between the predicted and achieved sensitivity. In the predicted sensitivity calculation we assumed that the atmospheric noise could be subtracted down to the white noise limit, which was predicted to be 660 μK_{CMB}. In section 3.6.3 we measured the white noise level achieved during the observing run to be $1.03 \times 10^{-16} W/\sqrt{Hz}$. We use the bolometer sensitivity and gain to convert to $1.4 mK_{CMB}\sqrt{s}$. This is a factor of 2 higher than our predicted white noise, due to the excess loading increasing the photon noise of the bolometers. Unfortunately, as we saw in chapter 5, the sky noise cannot be subtracted from the data down to the white noise limit. The actual sensitivity achieved at our signal frequencies can be determined from the PSDs of the data after PCA atmo-

spheric removal (see Figure 5.12). Although the sensitivity depends on the weather conditions, we can take an average value of $5mV/\sqrt{Hz}$, which can be converted using the calibration to $3.14mK_{CMB}\sqrt{s}$, almost a factor of 5 higher than the predicted value. The mapping speed is inversely proportional to the sensitivity squared, so with a factor of 5 difference in the achieved and predicted sensitivity we can account for a factor of 25 lower mapping speed. The predicted mapping speed assumed a full 144 detectors at 2.1 mm, whereas during the observing run we used 30 active detectors. Mapping speed is directly proportional to number of detectors, which accounts for another factor of almost 5 in the mapping speed, giving a total factor of 125, more than enough to account for the achieved mapping speed. It must be remembered that the blank maps were aggressively filtered to achieve the quoted mapping speed, removing most large-scale structure. Any survey for large scale structure would suffer from much lower mapping speeds.

Chapter 7

Conclusions

7.1 Bolocam Results

With Bolocam we have conducted a one square degree galaxy cluster survey. The survey consisted of two regions of blank sky, Lynx and SDS1. We made 1/2 $\times$ 1 degree maps of both regions, which were then filtered to extract cluster sources. We found two 4 σ decrements in the maps. We also analyzed the Lynx map to place an upper limit on the CMB angular power spectrum high ℓ SZE contribution. We found an upper limit of $\Delta T = 49\ \mu K_{CMB}$.

Atmospheric noise was the major limitation we faced, and further investigation is being conducted into how to fully remove this noise source from our time ordered data. Experiments have also been made during our 1.1 mm observing runs with chopping the secondary, although it remains to be seen if this is feasible at 2.1 mm given the larger beam size and limited chop throw of the CSO.

7.2 Future Prospects

Bolocam will return to the CSO this fall observing at 2.1 mm to continue our cluster survey. The excess load discussed in chapter 3 has been greatly reduced, and the observing run will show whether this improves the sky noise limit also.

Two new experiments are being developed to conduct large scale SZE cluster surveys, the APEX telescope in the Atacama desert in Chile (APEX SZ survey 2003),

and the South Pole Telescope (SPT) receiver, located surprisingly at the South Pole (Ruhl 2002). Both are large format bolometer arrays similar to Bolocam, although they will both use Superconducting Transition Edge bolometers. APEX will have a 300 bolometer array, while the SPT will have a 1000 bolometer array. Both will use have similar optical design to Bolocam, although both are still in design at the writing of this thesis. The major improvement over Bolocam will be the number of bolometers, the atmospheric conditions, and the amount of time available on the telescope for the surveys. Although both the Atacama desert and the South Pole offer better average millimeter wave observing conditions than Mauna Kea, it is interesting to apply Bolocam's achieved mapping speed (adjusted for the increased number of bolometers) to the integration time expected for each project. This will serve as an upper limit to the sensitivity these experiments should achieve as any improvement in sky noise will improve the results.

The APEX project expects 300 bolometers, which is a factor of 10 above that of Bolocam. The mapping speed is directly proportional to number of bolometers, so the APEX mapping speed should be an order of magnitude greater than Bolocam's, or 2.2 $\times 10^{-2}$ $arcmin^2/\mu K^2_{CMB}/hr$. APEX expects to dedicate 25% of the telescope observing time to the cluster survey, giving approximately 3 months, assuming 12 hours of integration time on source per night (similar to Bolocam's) that gives approximately 1000 hours per season. The number of hours dedicated to the cluster survey will likely be reduced by weather, times spent on calibration, and any instrument or telescope failures, but we can start with this for our estimate. APEX plans to survey 250 deg^2 over 2 seasons. If we apply our estimated mapping speed, that will give them a filtered map sensitivity of 143 μK_{CMB}/cluster. Because of the large area covered this survey will be ideal for detecting rare high flux clusters.

The SPT receiver expects an array of 1000 bolometers, a factor of 33 higher than Bolocam, giving an estimated mapping speed of 0.17 $arcmin^2/\mu K_{CMB}/hr$. If we assume that the SPT will have approximately the same amount of integration time on the cluster survey as ACBAR managed per season, we get approximately 1200 hours. We assume a survey area of 250 deg^2, the same as APEX, and assume a two

season effort. This gives us 2400 hours of integration time and a map sensitivity of 47 μK_{CMB}/cluster.

Bibliography

APEX SZ Survey, http://bolo.berkeley.edu/apexsz/science.html

Archibald, E.N., et al., *Monthly Notices of the Royal Astronomical Society*, **336**, 1, (2002).

Bennett, C.L., et al., *The Astrophysical Journal*, **583**, 1, (2003).

Bennett, C.L., et al., *The Astrophysical Journal*, **436**, (1994).

Benson, A.J., Reichardt, C., Kamionkowski, M., *Monthly Notices of the Royal Astronomical Society*, **331**, 1, (2002).

de Bernardis, P., *Nature*, **404**, (2000).

Bhatia, R.S., et al., *Cryogenics*, **40**, (2000).

Birkinshaw, M., *Physics Reports*, **310**, (1999).

Bock, J.J., et al., *Advanced Technology MMW, Radio, and Terahertz Telescopes*, **3357**, (1998).

Chiang, et al., *Monthly Notices of the Royal Astronomical Society*, **335**, 4, (2002).

Church, S.E., et al., *Proceedings of the ESA Symposium "The Far Infrared and Submillimeter Universe"*, **SP-401**, (1997).

Dawson, K.S., et al., *The Astrophysical Journal*, **581**, (2002).

Evrard, A.E., et al., *The Astrophysical Journal*, **573**, 1, (2002).

Glenn, J., et al., *Applied Optics*, **41**, 1, (2002).

Glenn, J., et al., *Advanced Technology MMW, Radio, and Terahertz Telescopes*, **3357**, (1998).

Glenn, J., *Personal Communication*, (2001).

Glenn, J., et al., *Applied Optics*, **41**, 1, (2002).

Goldin, A., *Personal Communication*, (2001).

Griffin, M., Bock, J., Gear, W., *Applied Optics - OT*, **41**, 31, (2002)

Herranz, D., et al., *The Astrophysical Journal*, **580**, 1, (2002).

Herranz, D., et al., *Monthly Notices of the Royal Astronomical Society*, **334**, 3, (2002).

Hobson, M., McLachlan, C., *Monthly Notices of the Royal Astronomical Society*, **338**, 3, (2003).

Holder, G., et al., *The Astrophysical Journal*, **544**, 2, (2000).

Holzapfel, W.L., *The Astrophysical Journal*, **479**, (1997).

Hubble, E., *Proceedings of the National Academy of Sciences of the United States of America*, **15**, 3, (1929).

Kolmogorov, A.N., Dokl. Akad. Nauk SSSR, **301**, (1941).

Kuo, C.L., et al., *astro-ph/0212289*

Lay, O.P., and Halverson, N.W., *The Astrophysical Journal*, **543**, 787, (2000).

Leighton, R., *Final Technical Report California Inst. of Tech*, (1976).

Lee, C., Ade, P.A.R., Haynes, C.V., *The 30th ESLAB Symposium on Submillimeter and Far-Infraread Space Instrumentation*, **388**, (1996).

Lin, Y., Mohr, J., *The Astrophysical Journal*, **582**, (2003).

Mason, B.S., et al., *The Astrophysical Journal*, **591**, (2003).

Mohr, J.J., Mathiesen, B., and Evrard, A.E., *The Astrophysical Journal*, **517**, (1999).

Peebles, P.J.E., astro-ph/0208037, (2002).

Peebles, P.J.E., *Principles of Physical Cosmology*, Princeton University Press (1993).

Penzias, A.A., Wilson, R.W., *The Astrophysical Journal*, **142**, (1965).

Perlmutter, S., et al., *The Astrophysical Journal*, **517**, 2, (1999)

Philhour, B.J., PhD Thesis, California Institute of Technology, (2001).

Press, W., Schechter, P., *The Astrophysical Journal*, **184**, (1974).

Richards, P.L., *Journal of Applied Physics*, **76**, 1, (1994).

Rosati, P., et al., *The Astrophysical Journal*, **118**, (1999).

Ruhl, J. Presentation at the KITP New Cosmology Conference, (2002).

Rudy, D. J., et al., *Icarus*, **71**, (1987).

Sanz, J.L., et al., *The Astrophysical Journal*, **552**, (2001).

Springel, et al., *The Astrophysical Journal*, **549**, (2001).

Stanford, S. A., et al., *The Astronomical Journal*, **114**, 6, (1997).

Zel'dovich, Y., Sunyaev, R., *Soviet Astronomy Letters*, **6**, (1980).